Dissipation and Nonlinear Effects in Nanomechanical Resonators at Low Temperatures

Kunal Lulla, MPhys

Thesis submitted to the University of Nottingham
for the degree of Doctor of Philosophy

· March 2011 ·

Abstract

Nanomechanical resonators have extremely low masses ($\sim 10^{-15}$ kg) and frequencies from a few megahertz all the way up to the gigahertz range. These properties along with a small damping rate make them very useful for ultrasensitive detection applications, now pushing into the realm of zeptonewtons (10^{-21} N) and zeptograms (10^{-21} g). On a more fundamental level, nanomechanical resonators are expected to display quantum mechanical effects when cooled down to millikelvin temperatures.

The understanding of dissipation in nanomechanical resonators is important for device applications and to study quantum mechanical effects in such systems. However, despite a range of experiments on semiconducting and metallic devices, dissipation in nanomechanical resonators at low temperatures is not yet well understood. Although mechanical resonators have traditionally been operated in the linear regime, exploiting their nonlinearities can prove advantageous for industrial applications as well as opening up new experimental windows into the fundamental study of the nonlinear dynamics of mesoscopic systems.

In this thesis, we present results from low temperature dissipation studies on pure gold and on gold-coated high-stress silicon nitride nanomechanical resonators. A theory, which predicts the existence of tunnelling two-level systems (TLS) in bulk disordered solids at low temperatures, is used as a framework to describe the data. The nonlinear interactions between different flexural modes of a single silicon nitride device, are explored experimentally and theoretically.

The resonators were fabricated as doubly-clamped beams using a combination of optical lithography, electron-beam lithography, dry and wet etching techniques. The motion of the resonators was actuated and detected using the magnetomotive scheme. At low temperatures, all the beams had

resonant frequencies between 3 and 60 MHz and quality factors in the range $10^5 - 10^6$. The strong variation observed in dissipation and resonant frequency at the lowest temperatures (below 1 K) indicates the presence of tunnelling TLS in nanomechanical resonators.

Dedicated to Mum and Dad

Acknowledgements

First of all, I would like to thank my supervisors Prof. J. R. Owers-Bradley, Dr. A. D. Armour and Dr. C. J. Mellor for their guidance and assistance over the past three and a half years. Be it low temperature experimental techniques, fabrication or the more theoretical aspects of this project, I have indeed learnt a great deal working with them. I would also like to thank my colleagues Dr. A. Venkatesan with whom I worked side-by-side for three years, and Mark for providing a helping hand with the experiments/fabrication whenever I needed it, and for writing the Labview program for the first set of experiments.

This thesis would not have been possible without the expert support of the talented technical staff in the School of Physics and Astronomy: Chris Pallender for the supplies of liquid helium, David Holt and Peter Smith in the workshop, Bob Chettle and his team and specially Steve Booth for his help in re-wiring the dilution fridge in B228.

On a more personal note, I would like to thank my friends in Nottingham and Leicester, people without whom I do not think I would have lasted so long in the UK.

First and foremost, my ex-housemates, Kuldeep (Shabhash!) and Ryan with whom I shared a house for more than two years. I will never forget our times at 23 Tattershall drive, the Christmas meals, the DVD marathons, the firework parties, Dino's! Of course, I cannot forget Samantha ('Dear Sam') for all those times when she made profiteroles for us, but more importantly, for being a kind friend. To my fellow team mates in the Dave Jephcote XI and Post-grad cricket team, thanks for putting up with me despite my temperament on the field. I would also like to thank James (Jamanjeet! alright...) for all the football related discussions we had, and Iain for his constant lectures on how awesome MRI and X-box 360 are. The last few

months would have not been the same without Filip and Todor, I want to thank them for all the Champions league football evenings, with chips and peppermint tea, and for allowing me to go round their house whenever I wanted. Last but definitely not the least, a big thank you to Jara, Kalpana and Laveena for their invaluable friendship and for always being there for me.

This thesis is not just the culmination of the last three years but of the past eight years, since the day when I first came to the UK for my undergraduate studies. I spent four years in Leicester, I made many friends and I would like to thank all of them, specially the guys from College hall, and of course Ali and Stephanie for everything they have done for me.

None of this would have been possible without the love and support of my family. I would like to thank Ravi uncle and Bhano aunty for helping me settle in the UK, and for providing me with a home away from home. Thanks to my grandma, uncles, aunties and cousins in India for all their love and encouragement. A big thank you to my brothers Amit and Jimmy, cousins Nilesh and Avi, Veena aunty, Divya and Mahek bhabhi and the kids for their belief in me and for bringing a smile onto my face at times when I needed it the most. A very special thank you to Reema bhabhi, who is not only my sister-in-law, but also my best friend. Finally, I would like to thank the two most important people in my life, my parents, for their unconditional love and support, hard work and sacrifice to allow me to fullfil my dreams of coming to the UK for my studies, I dedicate this thesis to them.

Contents

Chapter 1

Introduction

An electromechanical device is a mechanical element which is coupled to an electronic circuit, where the energy from the motion of the mechanical part is converted into an electrical energy. In the last ten to twenty years, fast progress in the fabrication techniques has led to the development of electromechanical devices with dimensions in the micrometre scale. Such devices are known as microelectromechanical systems (MEMS) and are now widely used in industrial applications: electric current regulators, radio-frequency (rf) components, navigational sensors are only some examples from a whole range of applications [1–4].

In more recent years, further minaturisation of electromechanical devices has led to the natural successors of MEMS, the nanoelectromechanical systems (NEMS), with even smaller dimensions. At the heart of a NEMS lies a nanomechanical resonator, usually in the form of a cantilever or a doubly-clamped beam with cross-sections below 1 μm. Nanomechanical resonators have extremely low masses ($\sim 10^{-15}$ kg) and frequencies from a few MHz all the way up to the GHz range. These properties make nanomechanical resonators extremely useful for ultrasensitive detection applications, with very high force [5] and mass [6] sensitivities.

On a more fundamental level, what makes these systems interesting is that they are mechanical objects with $\sim 10^{10}$ degrees of freedom; it would be of much interest to see how quantum mechanical effects manifest themselves in such systems as compared to a few atoms which have fewer degrees of freedom. A nanomechanical resonator is expected to behave quantum mechanically when its vibrational energy is greater than the thermal energy

of the surroundings, such that:

$$\hbar\omega \geq k_B T \tag{1.1}$$

where $\hbar$ is Planck's constant divided by 2π, $\omega = 2\pi f$ is the angular frequency of the resonator, k_B is the Boltzmann constant and T is the temperature of the thermal bath surrounding the resonator. Using this simple approximation, a nanomechanical beam with a resonant frequency of 1 GHz, for example, is expected to display quantum mechanical effects at 50 mK, a temperature well within the reach of current dilution refrigerators. Much of the ongoing experimental research on NEMS is performed at millikelvin temperatures, trying to cool the nanoresonator down to its ground state and measuring its position with quantum limited sensitivity by coupling it to other mesoscopic circuit elements such as qubits or microwave cavities [7–9].

1.1 Dissipation

The performance of nanomechanical resonators for the applications mentioned and for studying quantum effects is often limited by thermal noise and other sources of dissipation (energy loss) in the device. The dissipation is quantified by a number known as the Q-factor (Q = 1 / dissipation), the higher it is, the smaller the dissipation. Thermal noise can be minimized by performing the measurements at cryogenic temperatures. However, a full picture of the dissipation mechanisms needs to be established in order to maximize the potential of NEMS for nanosensor applications. Some of the more common sources of energy loss in nanomechanical resonators are clamping losses, gas friction and defects within the structure (dissipation mechanisms are covered in extensive detail in Chapter 2). Also, a good understanding of the dissipation mechanisms in nanomechanical resonators is vital for fabricating devices with extremely high Q-factors. Furthermore, if one is to probe the quantum nature of a nanomechanical system, it is important to understand the scaling of the dissipation with dimension and temperature (especially at the lowest temperatures where experiments of a quantum nature are performed).

Figure 1.1 shows a plot of Q-factor for resonators of varying sizes, clearly

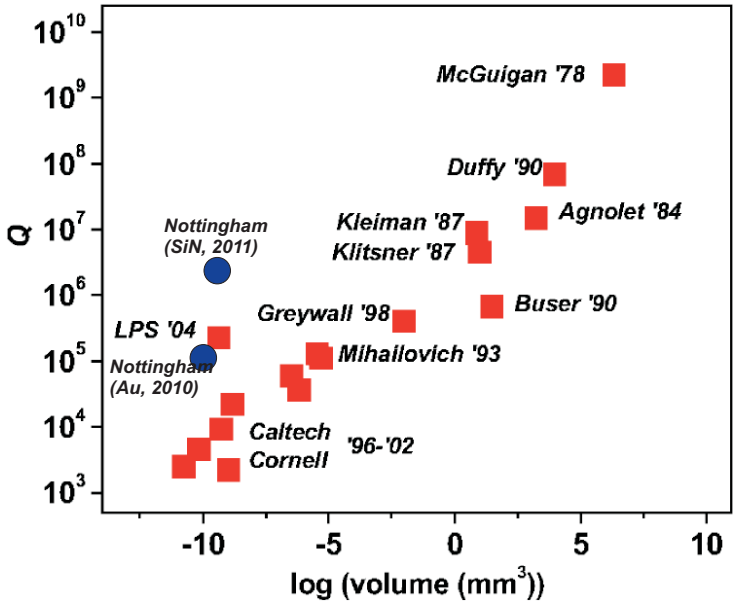

Figure 1.1: Maximum reported Q-factors in mechanical resonators of different materials and geometries and in different bath conditions [2]. The two blue circles correspond to the nanomechanical resonators investigated in this thesis.

showing a decrease in the Q-factor with dimension [2], contrary to what was popularly believed. The results from the two materials investigated in this thesis have also been included (blue circles in Figure 1.1) for comparison. It should be noted that this figure is far from being conclusive, as the data have been collected from experiments performed at different temperatures, with various materials and using different measurement techniques.

1.2 Nonlinear effects

Mechanical resonators can effectively be treated as harmonic oscillators as long as the forces acting on them are linear. However, nonlinearities are commonly encountered in nanomechanical devices, which usually manifest themselves, in the equation of motion of the resonator, as a force which is proportional to the cube of the displacement. This is commonly known as the Duffing nonlinearity. Nonlinearities in NEMS devices can arise, for example, from the effects of the measurement set-up, the clamping of the device or geometrical effects such as the lengthening of the beam [10, 11].

The onset of the nonlinear regime decreases with device dimensions,

therefore the linear dynamic range in nanomechanical resonators is severely limited [12]. It is important to understand the nonlinear behaviour in NEMS devices in order to avoid it when it is unwanted but to exploit it efficiently when required, especially for future nanotechnology applications. In terms of industrial applications, large integrated MEMS and NEMS devices usually contain an array of resonators which interact with each other through nonlinear forces. Understanding this coupling is of vital importance for device applications. Furthermore, the nonlinear coupling between two nanoresonators [13], or even between two vibrational modes of the same resonator [14, 15], can be exploited when studying the quantum effects in such structures. A system of coupled resonators has been proposed as a quantum nondemolition detection scheme, in which one resonator is in a quantum state [16].

1.3 Outline of this thesis

This thesis presents a study of dissipation and nonlinear effects in doubly-clamped nanomechanical beams of different sizes and materials, at temperatures below 2 K. The dissipation in doubly-clamped gold and silicon nitride beams was studied as a function of temperature and magnetic field. The nonlinear interactions between the different modes of a single silicon nitride beam were also investigated.

Chapter 2 provides the theoretical background describing the calculation of the resonant frequencies of doubly-clamped beams in several different limits using methods of continuum mechanics. A detailed discussion of the dissipation mechanisms which are known to be important for nanomechanical resonators is also presented, with focus on a theory known as the standard tunnelling model (STM) which is used as a framework to describe the low temperature dissipation data. The theory described in this chapter is used to analyze the results in Chapters 4 and 5. A brief literature review on previous low temperature dissipation experiments on both bulk and mesoscale structures is also provided.

Chapter 3 describes the fabrication and characteristics of the gold and silicon nitride beams used for the experiments described in Chapters 4, 5 and 6. The magnetomotive transduction scheme is explained in detail as it was used to actuate and detect the motion of the beams. The experimental set-

up for the respective studies is described as well as the different measurement techniques employed. The fitting procedures, used to extract the resonant frequency and Q-factor from the raw experimental data, are explained at the end of Chapter 3.

Chapter 4 describes the low temperature dissipation studies on two doubly-clamped gold beams of different lengths and cross-sections. These were the first set of measurements studying the dissipation in metallic resonators. We compare the estimated resonant frequencies to the measured ones and discuss the origins of the discrepancy between them. A magnetic field dependence study was used to infer the intrinsic Q-factor of the resonator at any given temperature. The dissipation and resonant frequencies of the beams were monitored as a function of temperature. The STM is used to qualitatively describe the data, and a detailed discussion of other recent dissipation studies in metallic nanomechanical structures is also provided with comparisons to our results. The work presented in this chapter has been published in [17, 18].

In Chapter 5, we present the results from the low temperature dissipation studies on gold-coated high-stress silicon nitride nanomechanical beams. The measurements were carried out in a similar manner to those for the gold beams, but with different equipment and in a different cryostat. A discussion on the effect of the gold layer on top of the resonator is given. We compare our results to those obtained recently by other research groups on similar structures.

Chapter 6 describes the theory and experimental aspects of the nonlinear studies on a single silicon nitride beam. We probed the nonlinear dynamics of three different vibrational modes of the same beam and studied the nonlinear coupling between them. We found a fairly good quantitative agreement between experiment and the theoretical model.

In Chapter 7, we summarize all our results and propose some improvements for future experiments studying both the dissipation and nonlinear dynamics of nanomechanical resonators.

Chapter 2

Theory and literature review

This chapter presents the theoretical foundations used to analyze the mechanical behaviour of nanomechanical resonators at low temperatures in the linear response (harmonic) regime. Nanomechanical resonators can be modelled as harmonic oscillators and so the first section provides a brief overview on the properties of harmonic oscillators. The governing equations for the flexural vibrations of doubly-clamped beams are obtained using the methods of continuum mechanics. The changes that have to be introduced to the equations when the beams are under a considerable amount of tension are also outlined. The main sources of damping in nanomechanical resonators are presented focusing on the ones that are most relevant at low temperatures. The standard tunnelling model (STM) which models the behaviour of low energy excitations (LEE) in bulk, structurally disordered solids in terms of tunnelling two-level systems (TLS) is described in detail. In the absence of a suitable theory that can explain the low temperature internal friction in mesoscopic structures, the STM provides a useful way to qualitatively describe our results.

2.1 Mechanical resonant systems

A harmonic oscillator, also known as a linear oscillator, is a system in which the restoring force is linearly proportional to the displacement and which has an oscillation frequency independent of the amplitude of motion. Mechanical resonators are often modelled as harmonic oscillators as it captures the principal resonance characteristics while allowing for a simple phenomeno-

logical description in terms of the resonant frequency and damping. This picture is only valid in the linear regime of operation, where the amplitude of the vibrating element is small. For large amplitudes, the relationship between force and displacement is no longer linear and the resonant frequency can then change depending on the system's displacement. Details of the theory of nonlinear oscillations are discussed in Chapter 6.

2.1.1 Simple harmonic oscillator

One of the simplest examples of a resonator is a mass m attached to a spring with a spring constant k [1]. When the mass is displaced from its equilibrium position, the spring exerts a restoring force $F = -ku$ where u is the displacement of the mass. The mass periodically oscillates with an angular frequency $\omega_0 = \sqrt{\frac{k}{m}}$ about the equilibrium position. A one dimensional (1D) simple harmonic oscillator can serve as a mathematical model for such a system, with an equation of motion given by

$$m\ddot{u}(t) + ku(t) = 0. \tag{2.1}$$

Since there is no damping mechanism in the system, the oscillation continues on forever. In a more realistic situation however, the motion of a resonator is driven (by an external sinusoidal force for example) and damped, where the damping term depends on the velocity of the resonator.

2.1.2 Driven damped harmonic oscillator

A more realistic oscillating system such as a nanomechanical resonator can be modelled as a driven damped harmonic oscillator [1] with an equation of motion given by

$$\ddot{u}(t) + \gamma\dot{u}(t) + \omega_0^2 u(t) = \frac{F_d e^{i\omega_d t}}{m}, \tag{2.2}$$

where γ is the damping coefficient, F_d is the amplitude of the driving force and ω_d its angular frequency. To find the homogeneous solution to the above expression, we first consider the undriven case which is [1]

$$\ddot{u}(t) + \gamma\dot{u}(t) + \omega_0^2 u(t) = 0. \tag{2.3}$$

A particular solution to equation 2.3 is $u(t) = \mathrm{Re}[u_0 e^{i\omega t}]$, where u_0 is the amplitude and ω the oscillation frequency. Substituting this solution into equation 2.3 gives $-\omega^2 + i\gamma\omega + \omega_0^2 = 0$ with solutions

$$\omega_\pm = i\frac{\gamma}{2} \pm \sqrt{\omega_0^2 - \frac{\gamma^2}{4}} = i\frac{\gamma}{2} \pm \omega_0\sqrt{1 - \frac{\gamma^2}{4\omega_0^2}}. \tag{2.4}$$

In the limit of small damping, the term inside the square root can be simplified by defining a new parameter, $Q = \frac{\omega_0}{\gamma}$, the quality factor which quantifies the damping in the system [1]. The displacement in terms of the Q-factor is

$$u(t) = \mathrm{Re}[u_0 e^{-\omega_0 t/2Q}(e^{\pm i\omega_0^{'} t})] = u_0 e^{-\omega_0 t/2Q}\cos(\omega_0^{'} t), \tag{2.5}$$

where the natural frequency of the system is

$$\omega_0^{'} = \omega_0\sqrt{1 - \frac{1}{4Q^2}}. \tag{2.6}$$

For the underdamped case ($Q \gg 1$), the system's motion can be approximated to that of a simple harmonic oscillator, $\omega_0^{'} \approx \omega_0$. On the other hand, for a strongly damped system ($Q \approx 1$), the natural frequency is lower than ω_0 and the displacement decreases rapidly within a few oscillations.

For the situation where the resonator is being driven by an external force, $F_d \neq 0$, the solution to equation 2.2 is a sum of the homogeneous solution (transient response, equation 2.5) and a steady state solution with motion only at the drive frequency. Since the amplitude of the transient response depends on the Q-factor, for times long in comparison to the damping time, this solution can be ignored. The particular solution is of the form $\mathrm{Re}[Re^{i\omega_d t}]$ where R is the amplitude response function of the oscillation [1, 19]:

$$R = \frac{F_d/m}{\omega_0^2 - \omega_d^2 + \frac{i\omega_0\omega_d}{Q}}, \tag{2.7}$$

a complex function which can witten as $R = R_x + iR_y$ where

$$R_x = \frac{F_d/m[\omega_0^2 - \omega_d^2]}{(\omega_0^2 - \omega_d^2)^2 + \frac{\omega_0^2\omega_d^2}{Q^2}} \tag{2.8}$$

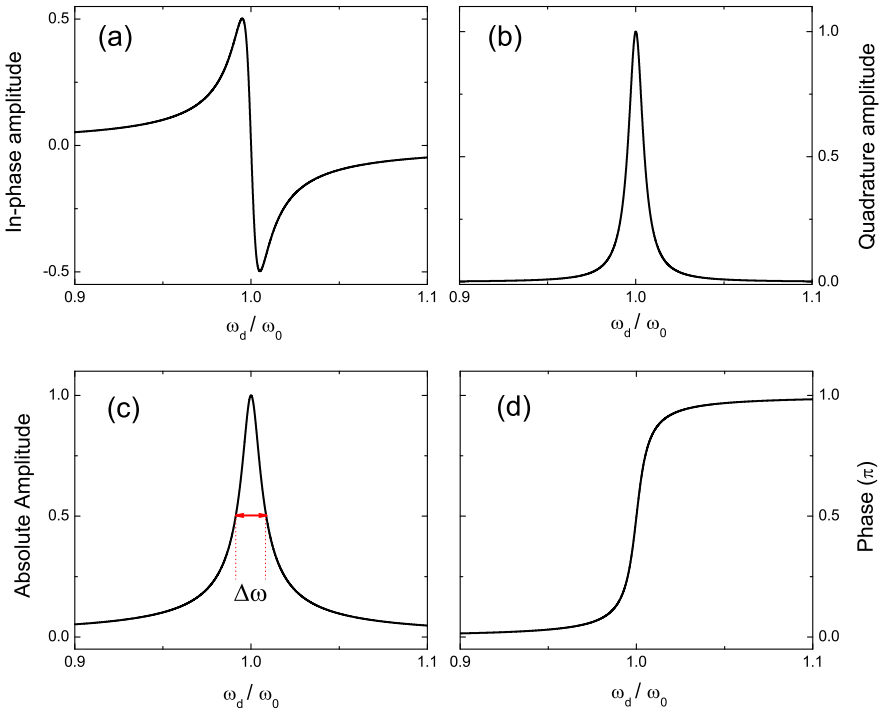

Figure 2.1: (a) In-phase, (b) quadrature and (c) absolute amplitude response of a driven damped harmonic oscillator as a function of driving frequency ω_d. (d) Phase response as a function of driving frequency ω_d.

and

$$R_y = -\frac{F_d/m[\frac{\omega_0\omega_d}{Q}]}{(\omega_0^2-\omega_d^2)^2+\frac{\omega_0^2\omega_d^2}{Q^2}}. \tag{2.9}$$

The real part (R_x) is known as the 'In-phase' amplitude and the imaginary part (R_y) is the 'quadrature' amplitude. The corresponding lineshapes are shown in Figures 2.1(a) and (b).

The resonant response function can also be expressed as $R = u_0 e^{-i\phi}$, where u_0 is the absolute amplitude $\left(u_0 = \sqrt{R_x^2 + R_y^2}\right)$ and ϕ the phase. They can be written as [1, 19]

$$u_0(\omega_d) = \frac{F_d/m}{\sqrt{(\omega_0^2-\omega_d^2)^2+\frac{\omega_0^2\omega_d^2}{Q^2}}}, \tag{2.10}$$

and

$$\phi(\omega_d) = \arctan \frac{\omega_0 \omega_d}{Q(\omega_0^2 - \omega_d^2)} \text{ for } \omega_d \leq \omega_0 \quad (2.11)$$

$$= \pi + \arctan \frac{\omega_0 \omega_d}{Q(\omega_0^2 - \omega_d^2)} \text{ for } \omega_d > \omega_0 \ . \quad (2.12)$$

On resonance, the oscillation amplitude is equal to $\frac{QF_d}{m\omega_0^2}$ [19]; the Q-factor amplifies the signal proportional to the resonator's displacement at the natural frequency. The amplitude response has the form of a Lorentzian with a peak at ω_0 as shown in Figure 2.1(c); the Q-factor is given by $Q = \frac{\omega_0}{\triangle\omega}$ where $\triangle\omega$ is the full width at half maximum (FWHM) of the Lorentzian curve. The phase of the signal goes through a 180° phase shift (Figure 2.1(d)), with the response being 90° out of phase with the drive at resonance.

2.2 Natural frequency

In this section we review the standard theory of beam mechanics [1, 20–22]. Consider the doubly-clamped beam represented schematically in Figure 2.2 with length L, width W and thickness h, with the coordinate system as shown. For a structure with a cross-section much smaller than its length, it is possible to derive a simple equation for the natural frequencies of oscillation considering only linear forces and ignoring any other complicated mechanical effects. In the absence of an external drive and a damping term, and considering only the linear response problem, the wave equation for the flexural motion of such a beam is given by [1]

$$EI\frac{\partial^4 z}{\partial x^4} - T_0\frac{\partial^2 z}{\partial x^2} + \rho A\frac{\partial^2 z}{\partial t^2} = 0, \quad (2.13)$$

where E is the Young's modulus, $I = \frac{Wh^3}{12}$ is the moment of inertia of the beam, T_0 is the intrinsic tension in the beam, ρ is the density and A the cross-sectional area [22]. Expression 2.13 is the Euler-Bernoulli equation [1] including a tension term. The two clamped ends impose the boundary conditions:

$$z(0,t) = z(L,t) = \frac{\partial z}{\partial x}(0,t) = \frac{\partial z}{\partial x}(L,t) = 0. \quad (2.14)$$

Equation 2.13 can be solved for several situations: the string limit where the tension dominates over the bending rigidity ($T_0/EI \gg 1$), the opposite

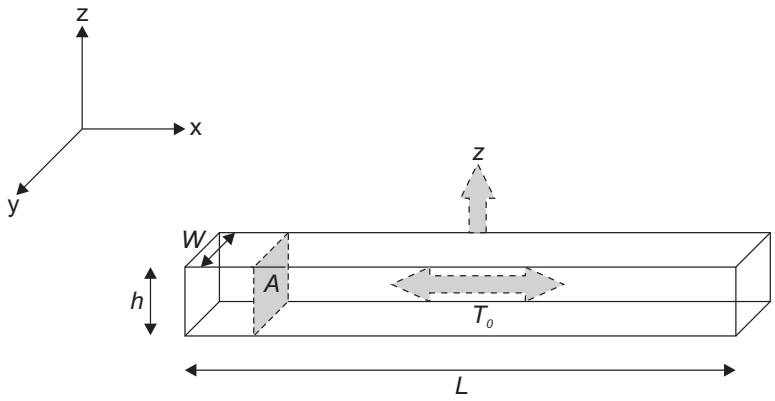

Figure 2.2: A schematic of a doubly clamped beam with dimensions $L \times W \times h$ and cross-sectional area A. The beam displaces in the z direction and is subject to a tension T_0 along the x-axis.

case known as the bending limit ($EI/T_0 \gg 1$), and one where both tension and bending rigidity are important. A general solution to the wave equation has the form

$$z_n(x,t) = \sum_n u_{0n} g_n(x) e^{i(\omega_{0n} t + \phi_n)} = \sum_n u_n(t) g_n(x), \tag{2.15}$$

where n=1, 2, 3, 4... is the mode number and $g_n(x)$ is the spatial function of the n^{th} mode. By substituting equation 2.15 into 2.13, the spatial dependence must satisfy the expression

$$EI\frac{\partial^4 g}{\partial x^4} - T_0\frac{\partial^2 g}{\partial x^2} - \rho A\omega_{0n}^2 g(x) = 0. \tag{2.16}$$

2.2.1 String limit

In the string limit, the tension in the beam determines its resonant frequency. The bending rigidity (first term in equation 2.16) is very small and can therefore be neglected. With a general solution of the form $g(x) = \sin(\frac{kx}{L})$, the displacement profile is simply [20]

$$g_n(x) = u_{0n} \sin\left(\sqrt{\frac{\rho A}{T_0}}\omega_{0n} x\right) \qquad \text{where } \omega_{0n} = \frac{k}{L}\sqrt{\frac{T_0}{\rho A}}, \tag{2.17}$$

where $k = n\pi$. As expected we simply obtain the 'guitar string' vibrational modes; the resonant frequency of the n^{th} harmonic is just $n\times$ the resonant

frequency of the fundamental mode.

2.2.2 Bending limit

In the bending limit we can ignore the tension in the beam (second term in equation 2.16), leading to a fourth order differential equation. The solutions, in terms of real functions, are: $g(x) = \sin(\frac{kx}{L})$, $\cos(\frac{kx}{L})$, $\sinh(\frac{kx}{L})$, $\cosh(\frac{kx}{L})$. Substitution of any of these into equation 2.16 leads to

$$k_n = \beta_n L \qquad \text{where } \beta_n = \left(\frac{\rho A}{EI}\right)^{\frac{1}{4}} \sqrt{\omega_{0n}}. \tag{2.18}$$

The general solution has the form

$$g_n(x) = c_1 \sin(\beta_n x) + c_2 \cos(\beta_n x) + c_3 \sinh \beta_n x + c_4 \cosh(\beta_n x), \tag{2.19}$$

where c_1, c_2, c_3, c_4 are constant coefficients. The boundary conditions imply that there are a discrete set of values of $\beta_n L$ satisfying the equation

$$\cos \beta_n L \cosh \beta_n L - 1 = 0, \tag{2.20}$$

which can be solved numerically to obtain $\beta_n L$ =4.73, 7.85, 10.99, 14.14... for the first four modes of oscillation [1]. This allows us to express the angular frequency of the fundamental mode as:

$$\omega_{01} = \left(\frac{4.73}{L}\right)^2 \sqrt{\left(\frac{EI}{\rho A}\right)}. \tag{2.21}$$

The spatial dependence for the four lowest frequency modes of a doubly clamped beam are shown in Figure 2.3.

2.2.3 Joining the two limits

In the case where the effects on the dynamics of the beam from both bending rigidity and tension are comparable, the solution to equation 2.16 is slightly more complicated as k becomes a tension dependent parameter. This scenario has been analyzed in detail in reference [22], the main aspects of which are outlined here.

Substituting solutions of the form $\sinh(\frac{kx}{L})$ and $\cosh(\frac{kx}{L})$ into equation

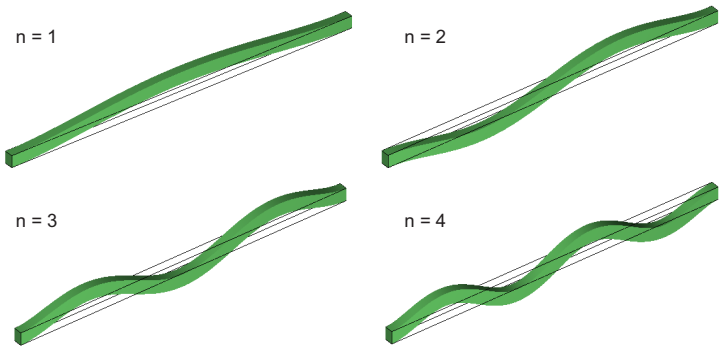

Figure 2.3: The four lowest frequency modes for a doubly clamped beam, solved using finite element simulations (COMSOL Multiphysics 3.3). The frequencies are determined by the factor $\beta_n L$.

2.16 leads to

$$k_1 = \sqrt{U + \sqrt{U^2 + \Omega^2}}, \tag{2.22}$$

whereas $\sin(\frac{kx}{L})$ and $\cos(\frac{kx}{L})$ give

$$k_2 = \sqrt{-U + \sqrt{U^2 + \Omega^2}}, \tag{2.23}$$

where $U = \frac{T_0 L^2}{2EI}$ and $\Omega = \omega_0 L^2 \sqrt{\frac{\rho A}{EI}}$ are the dimensionless tension and frequency parameters [22]. The general solution for the mode function $g(X)$ has the form

$$g(X) = c_1 \sinh(k_1 X) + c_2 \cosh(k_1 X) + c_3 \sin(k_2 X) + c_4 \cos(k_2 X), \tag{2.24}$$

where $X = \frac{x}{L}$ is a dimensionless parameter. Applying the boundary conditions 2.14 leads to the characteristic equation

$$\Omega + U \sin(k_2) \sinh(k_1) - \Omega \cos(k_2) \cosh(k_1) = 0, \tag{2.25}$$

which can be solved numerically for a given tension, T_0, to obtain the eigenfrequencies of a monolithic beam.

An analytical expression is also derived in reference [22] which provides a very good approximation to the mode frequencies obtained numerically:

$$f_{0n} = \frac{\pi}{8}(2n+1)^2 \frac{1}{L^2} \sqrt{\frac{EI}{\rho A}} \sqrt{1 + \frac{0.97 T_0 L^2}{(n+1)^2 \pi^2 EI}}. \tag{2.26}$$

Equation 2.26 provides an upper bound for the frequency of the fundamental mode (n=1). A derivation of an approximate equation for the resonant frequency of the fundamental mode as a function of tension has also been derived elsewhere [23], using a different type of approximation, but we will simply refer to the results here. The analytical expression for the frequency of the fundamental mode of a doubly-clamped beam as given in reference [23] is

$$f_{01} = \frac{2\pi}{L^2}\sqrt{\frac{EI}{3\rho A}\left(1 + \frac{L^2 T_0}{4\pi^2 EI}\right)}, \tag{2.27}$$

very similar to equation 2.26 for $n = 1$. The equations outlined in this section provide a reliable way of obtaining good estimates for the resonant frequencies of doubly-clamped beams given the correct material coefficients and device dimensions. Furthermore, it can be clearly seen that the presence of any tension T_0 in the beam will increase its resonant frequency.

2.3 Dissipation

The dissipation (Q^{-1}) determines the damping rate of a resonator, and is defined as $Q^{-1} = \frac{\gamma}{\omega_0}$. An alternative definition is

$$\frac{1}{Q} = \frac{1}{2\pi}\frac{\Delta E}{E}, \tag{2.28}$$

where ΔE is the energy lost during one cycle and E is the total energy stored in the system. Losses in nanomechanical resonators can be divided into two categories: intrinsic and extrinsic. Intrinsic losses are due to fundamental processes which occur within the structure, interactions involving electrons and phonons for example, and they are difficult to control. Extrinsic damping arises from the coupling of the resonator to its surroundings such as the measurement set-up, which can be accounted for and minimized. The overall energy loss in a resonator can be expressed in terms of a sum of several different mechanisms.

$$\frac{1}{Q} = \frac{1}{Q_i} + \frac{1}{Q_j} + \frac{1}{Q_k} + ..., \tag{2.29}$$

where the indices i, j, k represent different damping mechanisms. In this section we describe some of the main dissipation mechanisms which are

known to exist for nanomechanical resonators, focusing on the ones which are particularly important for our measurements. The STM is covered in greater detail as it provides a good phenomenological description for the behaviour of nanomechanical resonators at the lowest temperatures.

2.3.1 Extrinsic mechanisms

As the name suggests, extrinsic dissipation mechanisms arise from the coupling of the resonator to its surroundings such as, for example, the measurement set-up. The use of large magnetic or electric fields to actuate and detect the motion of resonators can increase the damping in the device by a considerable amount. Energy can also be lost through the supports into the substrates holding the beam, a mechanism which is known as clamping loss. However, unlike the intrinsic processes, extrinsic damping can be controlled and reduced.

Fluid friction

If a resonator is surrounded by a fluid (gas or liquid) then collisions with the fluid molecules can severely limit its quality factor. Depending on the pressure in the sample chamber, the losses due to friction can be divided into two categories. At very low pressures, the interaction is in the 'molecular' regime where the mean free path of the fluid molecules is much larger than the device dimensions. Thus the quality factor is limited due to individual collisions with the molecules. The energy loss in this case is given by

$$Q_{gas}^{-1} = \frac{pA}{m_{eff}\omega_0 v}, \tag{2.30}$$

where p is the pressure in the chamber, A and m_{eff} are the surface area and effective mass of the resonator, ω_0 its resonant frequency and v the thermal velocity of the gas molecules [24]. At higher pressures, the losses can be considered due to the viscosity of the fluid and $Q_{gas}^{-1} \sim \sqrt{p}$; the dissipation increases with pressure in the chamber as expected [25]. Frictional losses can be avoided by using a good vacuum.

Clamping

A vibrating resonator can lose energy to its supports through the propagation of acoustic waves into the substrate, and this can be an important source of dissipation in doubly-clamped beams. However for acoustic waves with a wavelength comparable to the beam length L, most of the waves are reflected back. A recent study by Wilson-Rae showed that

$$Q_{cl}^{-1} \propto \frac{h^4}{L^5} \tag{2.31}$$

for the fundamental mode of vibration of a monolithic structure [26]. Clamping losses depend strongly on the aspect ratio $\frac{h}{L}$ and are therefore expected to become increasingly relevant as the aspect ratio is increased, or in other words, at higher frequencies. Furthermore, clamping losses are expected to be temperature independent which means they can impose an ultimate limit on the Q-factor of a resonator at low temperatures. Careful fabrication methods can help minimize this type of damping. It is important to note that the theory described in reference [26] does not, however, consider the effects of tension on clamping loss.

Dissipation due to measurement set-up

Attempts to measure the mechanical motion typically tend to cause some disturbance of the motion, and often lead to additional damping. The technique we use is known as the magnetomotive transduction scheme [27], which involves passing currents through the device in the presence of a large magnetic field; the Lorentz force generated drives the resonator into motion.

The magnetomotive technique is widely used in the research of NEMS because of its simplicity, however, the use of this method results in a measured Q-factor which is loaded by the external circuit. Details of this technique and the loading effect are described in detail in Chapter 3, here we just quote the resulting effect on the Q-factor:

$$Q_L^{-1} = Q_0^{-1} + \alpha B^2,$$

where Q_L^{-1} and Q_0^{-1} are the loaded and intrinsic dissipations, B is the magnetic field and α is a constant that depends on the external impedance of the circuit and other resonator parameters [27].

2.3.2 Intrinsic mechanisms

Intrinsic dissipation mechanisms occur due to the interactions that take place inside the solid which may involve electrons, phonons, defects or any impurities present in the lattice. Intrinsic losses set an absolute limit to the performance of a mechanical oscillator. Most of the damping processes can be effectively treated in the framework of a simple generalization of the elasticity theory by C. Zener which accounts for the anelastic behaviour of solids [1]. One of the most important sources of dissipation in mechanical systems is the thermoelastic effect, the theory for which was first developed by C. Zener [28] and further developed for thin vibrating beams by R. Lifshitz and M. L. Roukes [29].

Thermoelastic effect

In the thermoelastic effect, mechanical vibrations of the structure induce local temperature gradients across the resonator, hence heat flows from hot to cold regions. Once out of its equilibrium position, the resonator tries to relax back to equilibrium by coupling to the thermal modes of the surrounding environment which make it a temperature dependent process. The temperature dependence of thermoelastic damping for thin vibrating beams is

$$Q^{-1} = \frac{E\alpha^2 T}{C_p} P, \tag{2.32}$$

where E is the Young's modulus, $\alpha = \frac{1}{L}\frac{\partial L}{\partial T}$ is the thermal expansion coefficient, T is the temperature, C_p the heat capacity at constant pressure and P is a constant which depends on the beam material's thermal diffusivity [29]. For the experiments described in this thesis, thermoelastic processes play no significant role as the measurements were carried out at temperatures below 2 K.

Surface effects

Figure 1.1 in Chapter 1 shows how the measured quality factor in many devices decreases in a linear fashion as the surface-to-volume ratio is increased [2]. This figure is far from being conclusive as the data have been collected from experiments performed under different conditions and with different types of devices, however, it still suggests that surface losses could be an

important source of dissipation. These surface losses can come from many different factors such as oxide or water layers and dangling bonds which may behave as TLS at low temperatures. Although various surface treatments like annealing [30] or surface passivation with thiol monolayers [31] can be employed to reduce these losses, they cannot be completely eliminated.

Two-level systems: Standard Tunneling Model

Studies of the thermal and acoustic properties of disordered solids at low temperatures have always been full of interesting yet unexpected results. Pioneering experiments carried out by Zeller and Pohl in 1971 [32] revealed striking differences at low temperatures ($T < 1$ K) between the thermal properties of dielectric amorphous solids and their crystalline counterparts. In a Debye dielectric crystal it is well known that the heat capacity and thermal conductivity are both proportional to T^3 at $T < 1$ K. In the case of amorphous solids, the specific heat is almost linear ($C \sim T^{1.2}$) and the thermal conductivity varies almost quadratically ($\kappa \sim T^{1.8}$). Furthermore the thermal conductivity of amorphous solids is considerably reduced compared to that of their crystalline counterparts, behaviour which was also observed in doped alkali halides where the motion of the dopants gives rise to additional low energy excitations [33].

The investigations mentioned above along with acoustic experiments confirmed the presence of low energy excitations and their interactions with phonons leading to the observed 'glass-like' low temperature features in disordered solids. Several theories were proposed in order to explain the behaviour of disordered solids at low temperatures, the most successful one being the Standard Tunneling Model (STM), introduced simultaneously by Phillips [34] and Anderson et al [35].

The STM predicts that the presence of defects in solids, such as dangling bonds, contaminants or dislocations, leads to the existence of anharmonic excitations which can cause damping. A double well potential model can be applied to these defects where an atom or group of atoms can sit in any one of two possible energy minima separated by an energy barrier height V as depicted schematically in Figure 2.4. At low temperatures only the two lowest energy eigenstates are considered hence they are known as two-level systems (TLS). They differ in energy by Δ which characterizes the asymmetry between the two wells and the tunnelling energy Δ_0 which is

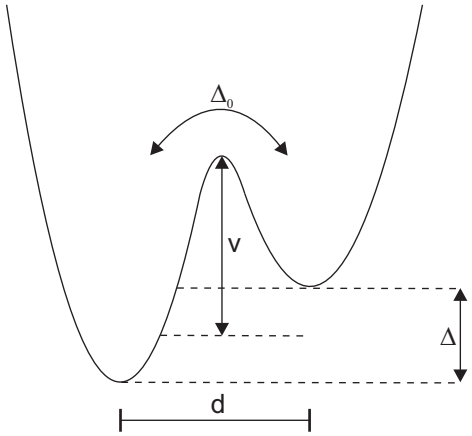

Figure 2.4: The double well potential model for defects in a solid, with barrier height V, width d, asymmetry Δ and tunnelling energy Δ_0. At low temperatures only the ground states of both wells play a role in the dynamics hence it is defined as a two-level system.

given by

$$\Delta_0 = \hbar\Omega e^{-\lambda} = \hbar\Omega e^{-d\sqrt{2mV/\hbar^2}}, \tag{2.33}$$

where $\hbar\Omega$ is the average of the two lowest energy states, d is the distance between them and m is the mass of the tunnelling particle. The TLS hamiltonian is

$$H_0 = \frac{1}{2}\begin{pmatrix} \Delta & \Delta_0 \\ \Delta_0 & -\Delta \end{pmatrix}, \tag{2.34}$$

and the total energy splitting is given by $E = \sqrt{\Delta^2 + \Delta_0^2}$ [36].

The STM assumes that there is a broad distribution of TLS with a wide range of energies and relaxation times $\tau(E,T)$ within the disordered solid. The relaxation time τ of the TLS depends on the energy E (and the underlying details Δ, Δ_0), but more importantly on the mechanism by which the TLS relax to equilibrium. This means that there is a range of values of Δ and Δ_0 which can be calculated using the probability distribution function $P(\Delta, \Delta_0)$. For Δ, the distribution function must be symmetric as both positive and negative values of Δ are equally likely. Furthermore, because of the exponential dependence of Δ_0 on λ, a small change in λ leads to a large range of Δ_0 over which λ can be assumed to be constant. The distribution function is assumed to have the general form

$$P(\Delta, \Delta_0) = \frac{P_0}{\Delta_0}, \tag{2.35}$$

where $P_0 \sim 10^{44}\mathrm{J}^{-1}\mathrm{m}^{-3}$ has been estimated from experiments on bulk amorphous solids [33, 37]. At temperatures above 1 K the asymmetry is not much larger than the thermal energy available and therefore the model breaks down as motion between the wells can occur via thermal activation, rather than tunnelling.

The TLS couple to their environment via strain and electric fields and therefore, can absorb energy from the mechanical motion which modifies the strain field. The TLS then release the energy through interactions with phonons and conduction electrons (in the case of metallic structures). This can occur via two processes: resonant and relaxation absorption. Once a given vibrational mode of the resonator with angular frequency ω is excited by an external acoustic wave, the behaviour depends on the ratio $\frac{\hbar\omega}{k_B T}$, where $\hbar\omega$ is the energy of the acoustic wave. If $\frac{\hbar\omega}{k_B T} \geq 1$, then the phonons can be resonantly absorbed by those defects with the correct energy splittings and the relevant TLS will undergo a transition from the ground state into the excited state. However, the overall effect of this depends on the population difference between the two states as acoustic excitation will stimulate emission as well as absorption of phonons. In the regime where $\hbar\omega \ll k_B T$, the TLS are likely to be in the ground state, resonant absorption is minimal and the contribution to the damping is negligible. However, there remains a measurable temperature dependence for the shift in frequency of the resonator arising from resonant interactions with TLS.

In order to directly excite a TLS, one needs an external drive at extremely high frequencies or be able to measure at the sub-millikelvin regime; for example, a frequency of 1 GHz corresponds to a temperature of $\sim$ 50 mK, a temperature easily achievable in a dilution refrigerator. Nonetheless, most experiments are performed in the regime where $\hbar\omega \ll k_B T$ as fabrication and detection of high frequency ($\sim$ GHz) resonators is difficult. If no direct excitation of the level occurs, there can still be dissipation in the vibrating element via anelastic effects which come about due to the phase delay between the stress and imposed strain. The acoustic wave couples to the TLS and changes its thermal equilibrium by altering Δ or Δ_0. The TLS then tries to relax to a new equilibrium position by, for example, absorbing and emitting thermal phonons, this results in dissipation and a shift in the resonant frequency of the resonator.

The strength of relaxation damping depends crucially on the ratio be-

tween the mechanical period and the relaxation time τ of the TLS. Maximum damping occurs when

$$\omega\tau \sim 1, \tag{2.36}$$

so that the mechanical period of the resonator matches the relaxation time of the TLS. The broad distribution of tunnel splittings, Δ_0, means that there is a broad range of relaxation rates. However, one can show that for the relaxation mechanisms relevant for TLS in amorphous solids there is always a well-defined minimum, $\tau_{min}(E)$, at each energy $E \simeq k_B T$ [33, 36]. At any given temperature T, it is this minimum relaxation rate $\tau_{min}(E)$, which is important. At the lowest temperatures where $\omega\tau_{min} \gg 1$, the dissipation drop will have a characteristic temperature dependence ($\sim T^n$) which depends on the details of the relaxation mechanism that determines τ. On the other hand, when $\omega\tau_{min} \ll 1$, the damping will be independent of temperature and relaxation mechanism, thus it will have a constant non-zero value. Figure 2.5 illustrates the behaviour of the frequency and dissipation as a function of temperature. The crossover temperature, T^*, is defined as that at which $\omega\tau_{min} \sim 1$.

As mentioned previously, TLS can relax through coupling with phonons (and electrons in the case of metals). For acoustic experiments in the regime $\hbar\omega \ll k_B T$, the resonant contribution to the damping is negligible in comparison with the relaxation contribution. Below T^*, the dissipation is proportional to $\sim T^n$ where $n = 3(1)$ depending on whether the relaxation is through phonons (electrons). Above T^*, the damping is given by

$$Q^{-1} = \frac{\pi}{2} C, \tag{2.37}$$

where $C = \frac{P_0 \eta^2}{\rho v^2}$ is a constant which depends on the density of states of the TLS in the structure but provides no information about the relaxation mechanism. The parameter η is the change in the TLS asymmetry per unit strain and v is the speed of sound.

The frequency shift at temperatures below T^* is dominated by the resonant mechanism (the relaxation mechanism in this regime is negligible compared to the resonant process) and it increases logarithmically with slope C. Beyond T^* relaxation processes start to dominate the frequency shift and a logarithmic decrease with temperature is observed, the gradient of which is determined by the relaxation mechanism. The main predictions of the STM

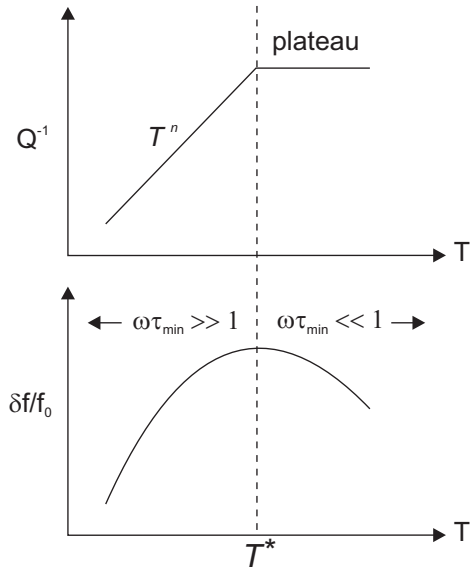

Figure 2.5: Generic predictions of the STM for the behaviour of Q^{-1} and frequency shift as a function of temperature in an amorphous solid ($\hbar\omega \ll k_B T$ over the whole range considered here). The relaxation mechanism completely dominates the dissipation with a plateau observed above T^* and a characteristic power law dependence below it. The frequency shift of the solid has contributions from both the resonant and relaxation mechanisms.

are summarized in Table 2.1 [37].

The difference in the properties of metallic and insulating amorphous structures becomes evident in acoustic measurements which probe the dynamics of TLS. Any property which probes the relaxation times of TLS will show a difference between the relaxation due to phonons and that due to electrons. Studies on attenuation in metallic glasses have shown that TLS have extremely short relaxation times when interacting with electrons [37].

The variation of the dissipation and frequency in a metallic structure is qualitatively similar to that of an dielectric one. However, there are two important differences: In dielectric materials, the logarithmic increase in frequency is from the contribution of the resonant process only whereas in metals the relaxation process contributes too. This is because in metallic structures, the crossover from the regime $\omega\tau_{min} > 1$ to $\omega\tau_{min} < 1$ occurs at much lower temperatures (sub mK) due to the fast relaxation of the TLS via electrons. In insulating solids, T^* highlights the temperature at which the contributions from the resonant and relaxation processes to the frequency of

Table 2.1: Predictions of the STM for the acoustic properties of dielectric and metallic amorphous solids. The parameters a and b provide information about the coupling between the TLS to phonons and electrons respectively, T_0 is an arbitrary reference temperature [37].

Interaction		Effect	$\omega\tau_{min} \gg 1$ $T \leq T^*$	$\omega\tau_{min} \ll 1$ $T \geq T^*$
Resonant		Q^{-1}	negligible for $\hbar\omega \ll k_B T$	
Resonant		$\delta f/f_0$	$C\ln(T/T_0)$	
Relaxation	to phonons	Q^{-1}	aCT^3/ω	$(\pi/2)C$
Relaxation	to electrons	Q^{-1}	bCT/ω	$(\pi/2)C$
Relaxation	to phonons	$\delta f/f_0$	negligible	$-(3/2)C\ln(T/T_0)$
Relaxation	to electrons	$\delta f/f_0$	negligible	$-(1/2)C\ln(T/T_0)$

the device match each other and it depends on the frequency as $T^* \propto \omega^{1/3}$. In metallic solids, $\omega\tau_{min} \sim 1$ is fulfilled at much lower temperatures and the maximum seen only marks the crossover from electron to phonon dominated relaxation and should be independent of the frequency [33].

The STM is not always in good agreement with the experimental data. Modifications have been tried in the past in order to account for the differences between theory and experiment which most commonly involved varying the distribution function of TLS [33]. Furthermore, the STM does not consider interactions amongst TLS, which is a factor to be considered at temperatures below 10 mK [38]. In the last section of this chapter we will review some of the experiments on bulk amorphous dielectrics and metals as well as more recent measurements on nanomechanical resonators. We will compare the results from these experiments to the predictions made by the STM.

Regarding the dissipation in nanomechanical resonators at low temperatures, the STM provides a useful framework to qualitatively analyze the results, but it is not able to give good quantitative predictions due to several factors. Firstly, the STM was developed to describe the low temperature behaviour of bulk amorphous solids and it does not take into account dimensionality. Secondly, we do not know a priori what the distribution function P is or how broad it is in such small devices. Furthermore, as the structures get smaller surface effects start to become more important, therefore it is essential to know whether the TLS are in the bulk or at the surface.

2.4 Previous studies of dissipation

Investigations of the sound attenuation and energy loss at low temperatures in mechanical oscillators have been carried out for many years, in this section we provide a brief review of some of the most important results obtained in this field of research. This section is divided into two parts: in the first part we will discuss some of the results from previous dissipation measurements on bulk amorphous solids and in the second part we will concentrate on the more contemporary experiments on micromechanical and nanomechanical resonators.

2.4.1 Low temperature studies on bulk structures

A detailed review on some of the earliest experiments on bulk amorphous solids is available in references [33, 37, 39]. For the purposes of this section, we only describe some of the results with a brief comparison between experiment and theory.

Dielectrics

The STM has been used extensively, with varying degrees of success, as a theoretical model for the internal friction in bulk amorphous solids at low temperatures. Some of the early experiments on the polymer PMMA (using the vibrating reed technique) [33] and on vitreous silica [39] agreed quite well with the STM. The internal friction in these materials had the expected T^3 dependence (due to phonon relaxation) below 1 K and a plateau at higher temperatures. Figure 2.6 shows the internal friction in vitreous silica, obtained by several research groups using different experimental techniques. A plateau is clearly seen for all samples at temperatures below about 10 K which is independent of the measuring frequency, with the low-temperature roll-off occurring at temperatures proportional to $\omega^{1/3}$, in agreement with the STM [39].

However, more recent measurements of the internal friction in vitreous silica using the mechanical double paddle resonator technique, showed disagreements with the STM at the lowest temperatures [40]. As can be noticed in Figure 2.7, the internal friction of the vitreous silica is in good agreement with the STM at the higher temperatures, indicated by the presence of a plateau, but at the lowest temperatures, the data deviate from the expected

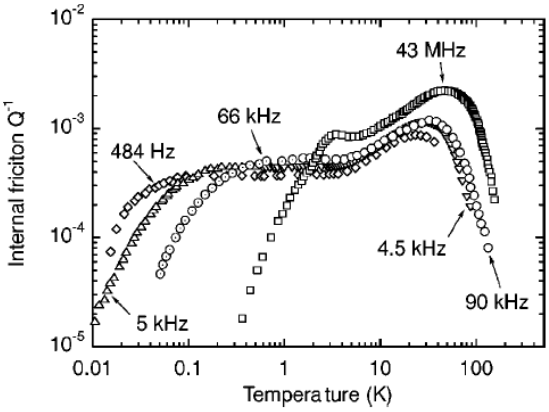

Figure 2.6: Internal friction of vitreous silica, measured by several research groups, at different frequencies. The devices exhibit the behaviour predicted by the STM, with a plateau below about 10 K and a cubic temperature dependence at the lowest temperatures. The roll-off temperature is proportional to $\omega^{1/3}$ as predicted by the model [39].

T^3 behaviour (denoted by the smooth black lines). Furthermore, the sound velocity increases with a different slope at the lower temperatures, depending on the frequency, features which cannot be explained by the STM. The Parpia group at Cornell (USA) also measured the internal friction and sound velocity in double paddle amorphous silica oscillators down to 1 mK [38]. A crossover from the T^3 dependence predicted by the STM to a T dependence was observed which they claim demonstrates the existence of interactions amongst TLS, which are not accounted for in the basic version of the STM.

Although, the STM is not always in good agreement with the experiments, it is a well known fact that the constant C for many disordered materials, obtained from the plateau, lies within a narrow range as illustrated in Figure 2.8. The range bounded by the dashed lines is known as the 'glassy range' ($Q^{-1} \approx 10^{-3} - 10^{-4}$). The internal friction for many amorphous solids lies within this range, at least down to 10 mK.

Metals and alloys

Experiments on amorphous metals never agreed as well with the predictions of the STM as those on dielectrics. Vibrating reed and wire experiments by Esquinazi et al [41], found only qualitative agreement between the STM and the internal friction of amorphous PdSiCu, with the temperature dependence being linear which disagreed with theoretical model for the phonon-TLS in-

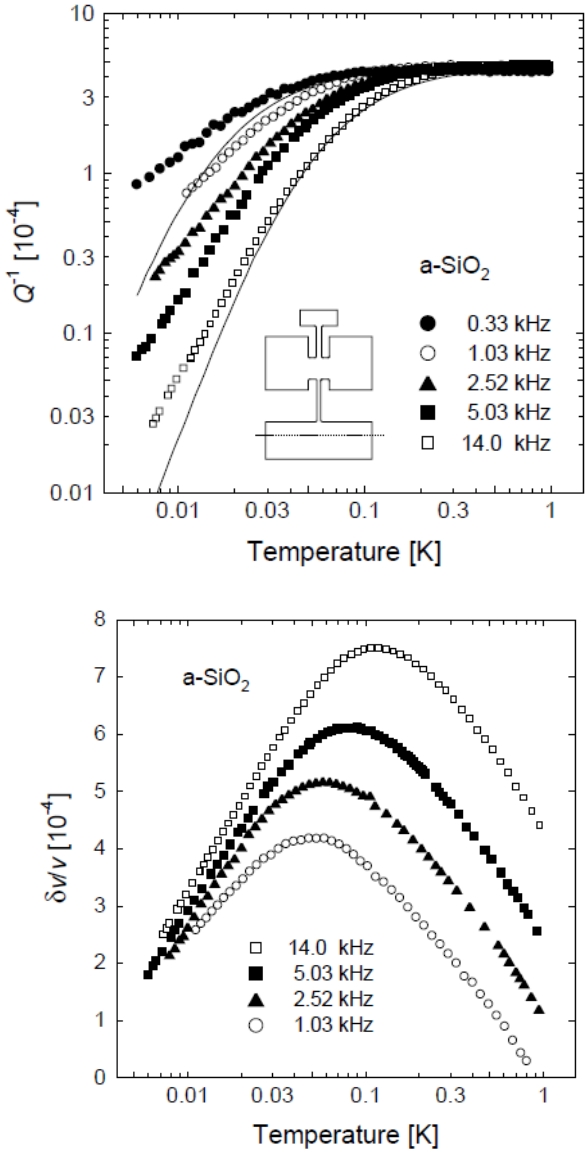

Figure 2.7: (Top) Temperature dependence of the dissipation of vitreous silica at five frequencies, (Bottom) temperature dependence of the sound velocity at four frequencies [40].

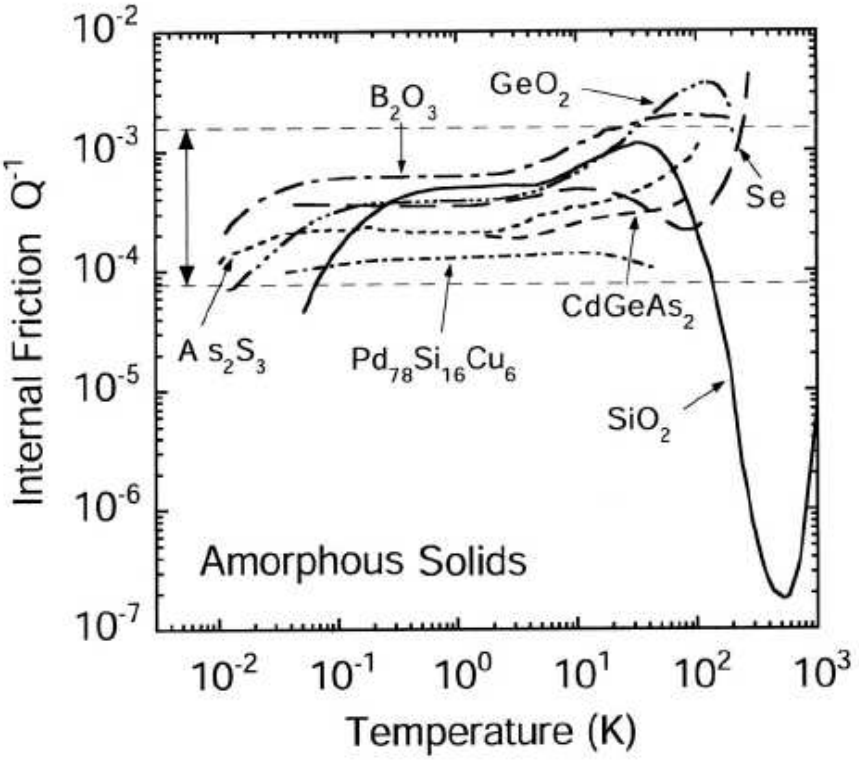

Figure 2.8: The internal friction of several amorphous solids between 0.1 and 10 K, where the internal friction is nearly independent of temperature and frequency. The dashed lines denote the glassy range [39].

teraction. Data for polycrystalline silver revealed a plateau in Q^{-1} from 600 - 60 mK and a $T^{1/3}$ drop at lower temperatures once a constant background was subtracted from the data. This behaviour does not agree with STM predictions and the $T^{1/3}$ dependence is considerably lower than expected. Vibrating wire measurements by König et al [42] on polycrystalline platinum (Pt) and aluminium (Al) revealed the absence of electron assisted relaxation in these systems. Whilst for Pt, Q^{-1} had a typical temperature dependence and magnitude of amorphous dielectrics, the sound velocity in the structure showed a plateau below 10 mK, a feature not explained by the theory. König et al also carried out investigations on Al in both normal and superconducting states; no difference was observed in the behaviour between both states which led the authors to claim that electron-assisted relaxation plays no significant role in Al. However, more recent vibrating

reed experiments by Haust et al [43] disagree with this as they observe a significant difference in the magnitude of Q^{-1} between the normal Al state and the superconducting one.

In another set of experiments by Liu et al [44], the low temperature internal friction of thin metal films was measured on substrates of ultra-pure boron-free silicon double paddle oscillators vibrating in their asymmetric mode. They first measured the dissipation of the bare paddles, and then measured the loss in the film coated oscillators, to finally use the equation

$$Q_{film}^{-1} = \frac{G_{sub}t_{sub}}{3G_{film}t_{film}}(Q_{pad}^{-1} - Q_{sub}^{-1}) \tag{2.38}$$

to calculate the loss in the film. Here G is the shear moduli of the material, Q_{sub}^{-1} is the dissipation in the bare paddle and Q_{pad}^{-1} is the dissipation in the coated resonators. Liu et al, claimed that the material type, film thickness and fabrication processes had minimal influence on the internal friction. They found the damping in most metal films to be only weakly dependent on temperature below 10 K, with a magnitude very close to the dissipation in bulk amorphous insulators, denoted by the 'glassy range' in Figure 2.9.

2.4.2 Low temperature studies on mesoscale structures

There have been only a few studies on the internal friction in nanomechanical resonators at low temperatures. The Mohanty group in Boston (US) have studied dissipation in nanomechanical resonators in materials such as silicon, gallium arsenide and diamond, however, their devices also had a 80 - 100 nm thick metallic layer on top for actuation/detection purposes. For all the materials studied, it was found that both the dissipation and shift in frequency can be described phenomenologically by the STM [45–47]. They found a $\sim T^{1/3}$ temperature dependence of the internal friction below 1 K, but observed no clear plateau. The shift in frequency follows the expected shape as predicted by the STM but the values of C extracted from the frequency plots are an order of magnitude lower than for bulk amorphous solids.

Studies on nanoscale metallic resonators have been scarce. The work described in Chapter 4 was the first systematic study of low temperature dissipation in metallic nanomechanical resonators. However, very recently other groups have begun to study metallic systems as well. A review on

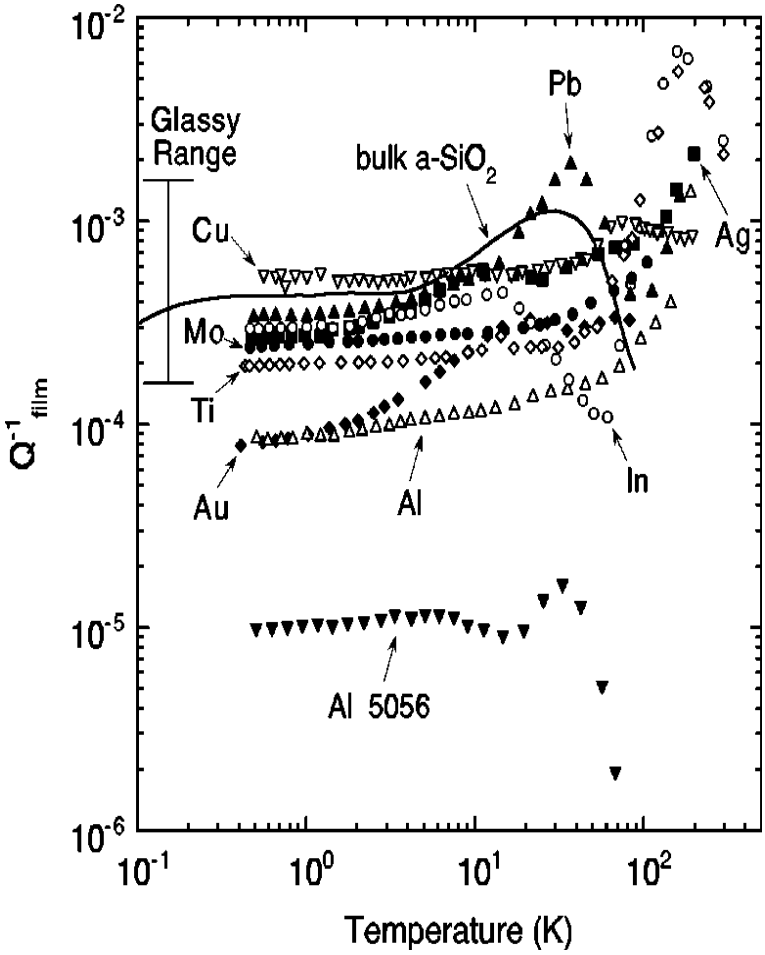

Figure 2.9: Internal friction of several metal films determined using equation 2.38. The vertical bar indicates the range of internal friction in the temperature-independent region, measured on a wide range of bulk amorphous solids [44].

some of the most recent work on aluminium resonators is given at the end of Chapter 4, with comparisons to our results for the low temperature dissipation in gold beams.

2.5 Summary

In this chapter we have derived the principal equations which describe the flexural motion of nanomechanical resonators in the linear response (harmonic) regime. The natural frequencies of the resonators can be derived using methods of continuum mechanics with slight changes to include the effects of tension. The main damping mechanisms that are known to affect nanomechanical resonators have been described, with a detailed explanation of the STM, which we will use later to qualitatively describe our low temperature data. A brief review of previous dissipation studies is also given with comparisons to the STM.

Chapter 3

Experimental Techniques

This chapter discusses the fabrication and properties of devices used for the dissipation and nonlinear studies at low temperatures, which include gold beams on gallium arsenide and gold-coated, high-stress silicon nitride beams on a silicon substrate. The principal steps of the device fabrication are given in this chapter whereas further processing details and technical specifications are given in Appendix A. Details of the experimental arrangements for the low temperature measurements are also presented. The magnetomotive transduction scheme is explained in detail outlining the two main measurement techniques used: continuous wave (CW) and pulsed. The last section describes the fitting procedures for both the CW and ring-down signals from which the resonant frequency and the Q-factor of the resonators were accurately extracted.

3.1 Device fabrication

3.1.1 Gold beams on gallium arsenide

Nanomechanical resonators consisting of doubly-clamped gold beams were used for dissipation studies at temperatures below 2 K. They were fabricated using a combination of standard electron beam (e-beam) lithography and wet etch techniques; an outline of the fabrication process is given in Figure 3.1. A <100> insulating gallium arsenide (GaAs) wafer was scribed into smaller 9.8×9.8 mm chips which were subsequently cleaned with solvents ethyl lactate, acetone, methanol and isopropanol (IPA) in ultrasound for five minutes each. To finish off the cleaning process, the chips were placed

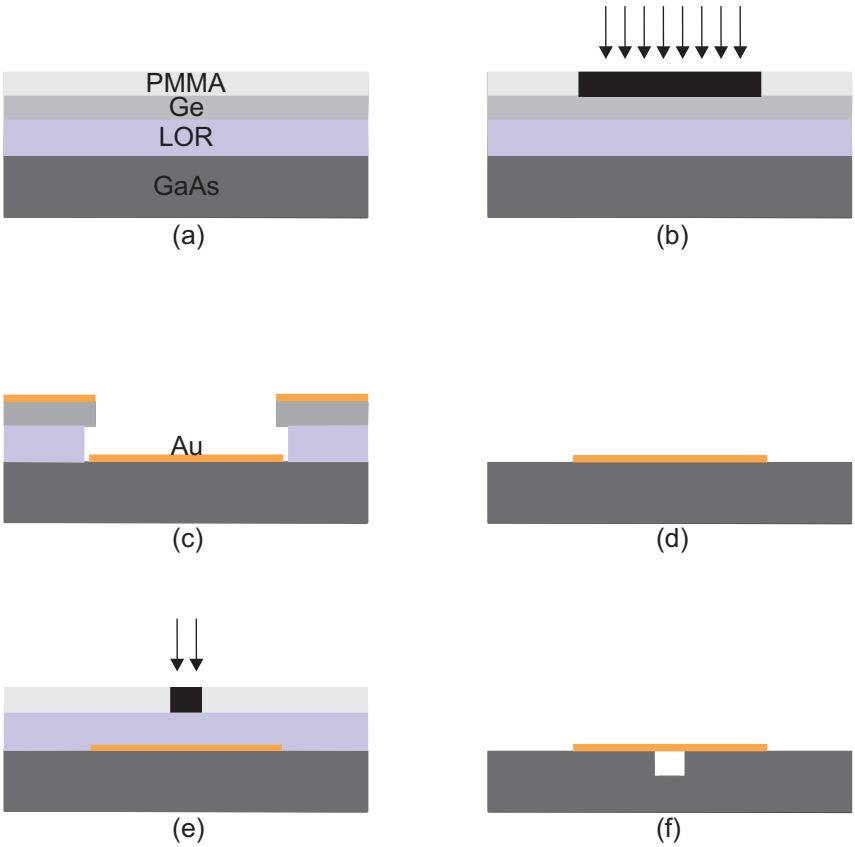

Figure 3.1: Fabrication process for a doubly-clamped gold beam on top of a GaAs substrate. (a) The GaAs chip is coated with a trilayer consisting of PMMA/Ge/LOR, (b) the stencil is patterned using e-beam lithography, (c) the PMMA is developed and the Ge/LOR layer is etched via plasma etching, the gold is then evaporated, (d) the Ge/LOR stencil is removed in photo-resist stripper, (e) the chip is coated with another bilayer consisting of PMMA/LOR and a suitable etch window is patterned using e-beam lithography and (f) finally, the underlying GaAs is wet etched to release the beam.

in a plasma asher for five minutes at 150°C.

A trilayer resist consisting of lift-off resist (LOR) [48], germanium (Ge) and poly-methyl methacrylate (PMMA) [48] was coated onto the GaAs chips. A Ge stencil with an undercut LOR was obtained using e-beam lithography and plasma etch processes as outlined in reference [49]. The patterns defined nano-wires of two different lengths, 12 μm and 20 μm with widths in the range 250-300 nm, connected to wider electrical contact pads. The stencil was metallized with an adhesion layer of 3 nm thick titanium (Ti) followed by the deposition of 60-80 nm thick gold in a thermal evaporator.

The Ge/LOR stencil was removed in photo-resist stripper (1165 Microposit Remover) [50] and a doubly-clamped beam was then released by wet etching the underlying GaAs. A window patterned in a second PMMA/LOR bilayer resist using e-beam lithography was used to selectively etch only the region of interest. A standard wet etch recipe H_2SO_4:H_2O_2:H_20 in the ratio 1:8:100 by volume was used. By wet etching, rather than plasma etching the GaAs, possible sputtering and ion-implantation damage was avoided. The etched substrate was rinsed in de-ionized (DI) water followed by methanol, and then blown dry with nitrogen gas; any remaining resist was removed in an oxygen plasma asher. The results presented in this thesis correspond to two beams of length $L \sim 7.5$ μm and 10.5 μm, thickness $h \sim 80$ nm and 65 nm and width $W \sim 300$ nm and 250 nm. A typical doubly-clamped gold beam used for the dissipation studies is shown in Figure 3.2.

3.1.2 Gold-coated high-stress silicon nitride beams

Gold-coated high-stress silicon nitride resonators were used for further dissipation studies at low temperatures as well as experiments investigating the nonlinear coupling between the different modes of a single beam. The devices were fabricated from wafers composed of a 190 μm thick silicon wafer [51] with 170 nm of LPCVD[1] silicon nitride on both sides [52]; the nitride layer has a built-in tensile stress of $\sim$ 1070 MPa, measured by the Cornell Nanoscale Facility (CNF). The resonators were made using a combination of optical lithography, e-beam lithography and plasma etching. A schematic diagram including the main steps of the fabrication process is shown in Figure 3.3.

[1]Low pressure chemical vapour deposited

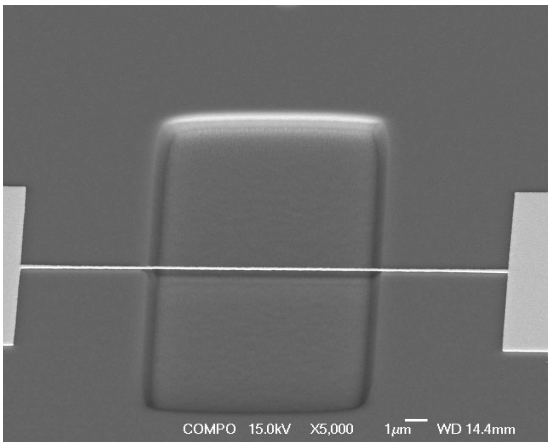

Figure 3.2: Scanning electron microscope image of a gold nanomechanical resonator. The nanowire is 20 μm long and the suspended region which forms the resonator is 10.5 μm in length.

The wafers were first scribed into 9.8 $\times$ 9.8 mm pieces and cleaned in the same manner as described in the previous section. A trilayer resist consisting of LOR, Ge and photo-resist AZ6612 [48] was coated on the wafer. The samples were then soaked in toluene for 5 minutes to avoid over-developing the photo-resist after UV exposure.

The electrical contact pads were defined using optical lithography, the Ge in the exposed areas was fully dry-etched whilst around only 50-100 nm of the LOR was removed. The sample was then coated with two layers of PMMA and the nano-wires were patterned via e-beam lithography including several alignment processes to ensure the contacts and the wires were connected to each other. The remaining Ge/LOR in the exposed areas was etched away. The resulting stencil was metallized with 3 nm of Ti and 90-130 nm of gold in a thermal evaporator, followed by lift-off in photo-resist stripper. Using a PMMA/Ge/LOR trilayer a suitable etch window was patterned in the areas of interest using e-beam lithography, and finally the doubly-clamped beams were released through an anisotropic etch of Si_3N_4 in a CHF_3 plasma followed by an isotropic etch of Si with SF_6. The gold layer acted as a mask however some of it was sputtered away while releasing the beams. This meant the gold on the beams was thinner than on the contacts. A more detailed account on the fabrication of silicon nitride resonators is given in Appendix A.

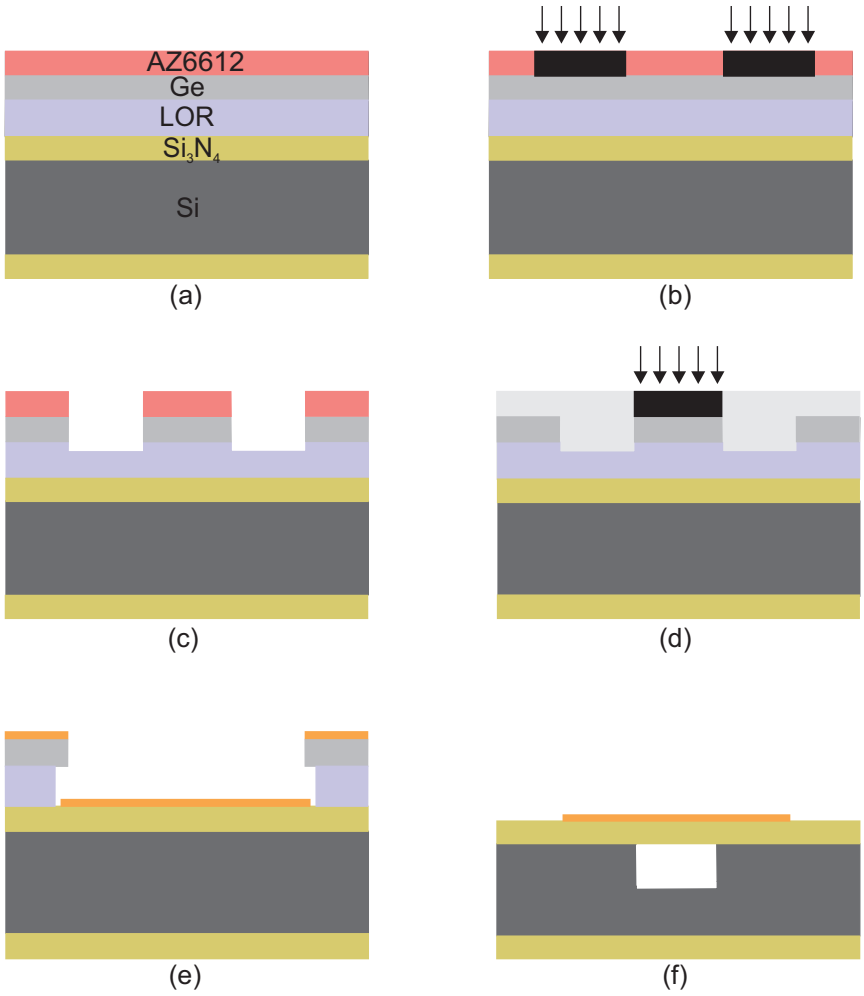

Figure 3.3: Fabrication process for gold-coated high-stress silicon nitride beams. (a) The Si_3N_4/Si wafer is coated with a trilayer resist consisting of AZ6612/Ge/LOR, (b) the contacts are patterned using optical lithography, (c) the photo-resist is developed and the Ge etched fully whilst the LOR is partially etched. (d) The wafer is then coated with two layers of PMMA and the wires are patterned using e-beam lithography, (e) the PMMA is developed, the remaining Ge/LOR etched away and gold is evaporated, (f) finally, after patterning a suitable etch window on a PMMA/Ge/LOR trilayer resist, the beams are released through dry etch processes.

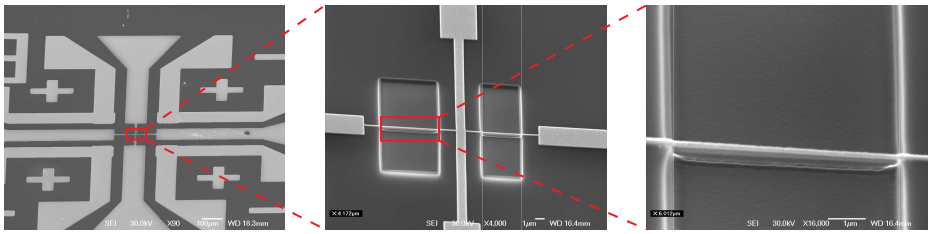

Figure 3.4: Scanning electron microscope image of the contact pads (a), gold coated silicon nitride beams in bridge formation (b) and a 6.4 μm long resonator with 80 nm of gold on top (c).

Figure 3.4 shows images of a typical silicon nitride resonator used for the experiments described in Chapters 5 and 6. The contacts are in the shape of coplanar waveguides[2] (Figure 3.4(a)) to ensure good impedance matching between cables and the sample thereby minimizing unwanted reflections. The resonators were prepared in a bridge formation (Figure 3.4(b)) to minimize any frequency varying background noise [53] (the balanced bridge technique is discussed in more detail in section 3.3.2).

Two batches of devices were made for the measurements, each having four beams (two bridges). The first batch consisted of doubly-clamped beams with lengths 4.4 μm, 6.4 μm, 15.8 μm and 25.5 μm; the width was the same for all, about (190 $\pm$ 10) nm, with the thickness of the nitride layer being 170 nm. The thickness of the gold layer on top of the beams was around (80 $\pm$ 10) nm. The second batch included 4 beams of the same lengths as the first but with a width of $\sim$(170 $\pm$ 10) nm and (40 $\pm$ 10) nm thick gold. As mentioned earlier, part of the gold is etched away when releasing the beams; by exposing part of the contact pad on a test sample, the amount of gold etched away from that region compared to an unexposed area was measured using a surface profiler. The test sample was subjected to the same etching processes used to release the beams.

[2]A coplanar waveguide consists of a central conducting strip with a ground plane on each side, on top of a dielectric surface. They are commonly used to send high frequency signals (with a low parasitic background) to micro/nano-electronic devices.

3.2 Transduction scheme

For the experiments described in this thesis, the magnetomotive transduction scheme was used to drive and detect the motion of the nanomechanical resonators. This technique was first developed by A. N. Cleland and M. L. Roukes [54]. Although there are other methods to detect the motion of such devices, for example capacitive coupling to other mesoscopic electronic elements [55, 56], piezoresistive actuation and optical detection [57], the magnetomotive technique is the simplest to implement in nanomechanical devices and has been used to detect mechanical frequencies up into the GHz range [58].

The magnetomotive technique involves placing a conducting beam of length L at the centre of a uniform magnetic field B with its longitudinal axis perpendicular to the magnetic field. To drive the beam into motion, a radio-frequency (rf) alternating current $I_d(t) = I_0 e^{i\omega t}$ is passed along the length of the resonator, transverse to the magnetic field; I_0 and ω are the amplitude and frequency of the oscillating current. A Lorentz force, $F_d = LBI_d(t)$, is generated at the same frequency as the rf current and perpendicular to both the current and magnetic field, which excites the motion of the beam [1, 27]. The scheme is illustrated in Figure 3.5.

The motion of the beam can be described by the equation

$$\ddot{u} + \gamma\dot{u} + \omega_0^2 u = \frac{LB}{m} I_d(t), \tag{3.1}$$

where $u(t)$ is the displacement of the beam in the direction of flexure, m its mass, ω_0 its resonant frequency and $\gamma = \frac{\omega_0}{Q_0}$ is the damping coefficient. The resulting displacement of the resonator generates an electromotive force (EMF) across it, which according to Faraday's Law, opposes the flow of current thereby increasing the impedance of the beam on resonance. This EMF is given by

$$V_{emf}(t) = \frac{d\Phi}{dt} = \xi_n LB \frac{du(t)}{dt} \tag{3.2}$$

where $\Phi = LBu\xi_n$ is the flux and ξ_n is a geometric constant that accounts for the non-uniform displacement of the vibrational mode (n is the mode number); for the fundamental mode of a doubly-clamped beam ξ_1 =0.83 [1].

Allowing the displacement to have the form $u(t) = u_0 e^{i\omega t}$, where u_0 is the amplitude, and substituting this into the equation of motion 3.1, the

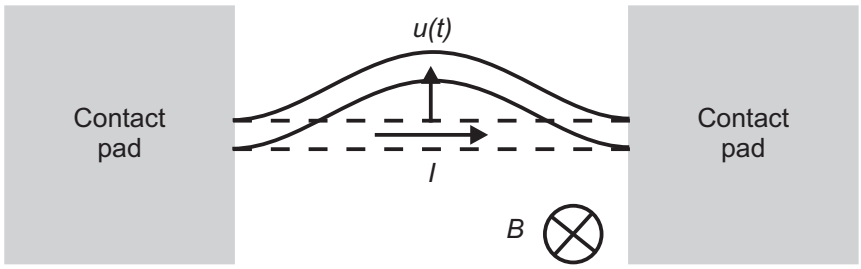

Figure 3.5: Schematic diagram of the magnetomotive drive and detection technique. An rf alternating current is passed through the beam, perpendicular to the magnetic field, generating a Lorentz force which actuates the motion of the beam. A vibrating current-carrying beam in a magnetic field produces an EMF voltage which is proportional its displacement.

beam's displacement can be expressed in terms of the driving current:

$$u(t) = \frac{LBI_d(t)}{m(\omega_0^2 - \omega^2) + \frac{im\omega\omega_0}{Q_0}}. \tag{3.3}$$

Combining equations 3.2 and 3.3 yields

$$V_{emf}(t) = i\omega \frac{\xi L^2 B^2 I_d(t)}{m(\omega_0^2 - \omega^2) + \frac{im\omega\omega_0}{Q_0}}. \tag{3.4}$$

Equivalent electrical circuit A mechanical resonator undergoing magnetomotive transduction is electrically equivalent to a parallel combination of an inductor L_m, a capacitor C_m, and a resistor R_m [27], as depicted in Figure 3.6. For the case where the external impedance Z_{ext} is infinite, the voltage across the circuit is given by

$$V_{emf}(t) = i\omega \frac{\frac{I_d(t)}{C_m}}{(\omega_{LC}^2 - \omega^2) + \frac{i\omega}{R_m C_m}} \tag{3.5}$$

where $\omega_{LC} = 1/\sqrt{L_m C_m}$ is the resonant frequency of the LCR circuit. Clearly, equations 3.4 and 3.5 are analogous to each other and the model circuit parameters can be identified in terms of the mechanical properties of the resonator

$$C_m = \frac{m}{\xi L^2 B^2}, \qquad L_m = \frac{\xi L^2 B^2}{m\omega_0^2}, \qquad R_m = \frac{\xi L^2 B^2}{m\omega_0^2} Q_0. \tag{3.6}$$

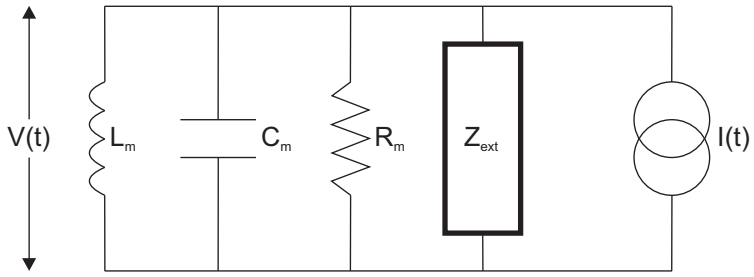

Figure 3.6: LCR representation of a mechanical resonator with a external impedance Z_{ext}, which includes the electrical resistance of the sample itself and the rest of the circuit used for the measurements.

The above implies the equality of the resonant frequencies $\omega_{LC} = \omega_0$.

In the case where the external impedance Z_{ext} has a finite value, the voltage across the whole circuit is

$$V_L(t) = i\omega \frac{\frac{I_d(t)}{C_m}}{\left(\omega_0^2 + \frac{\omega\omega_0 Z_c X_{ext}}{|Z_{ext}|^2}\right) - \omega^2 + i\omega\omega_0\left(\frac{1}{Q_0} + \frac{Z_c R_{ext}}{|Z_{ext}|^2}\right)} \tag{3.7}$$

where R_{ext}=Re$[Z_{ext}]$, X_{ext}=Im$[Z_{ext}]$ and $Z_c = \sqrt{L_m/C_m}$ [27]. From the above expression it is clear that the external impedance has an influence on the measured voltage signal; in this case, the measured resonant frequency f_0 and Q-factor are not intrinsic to the resonator but depend on the full measurement circuit. The loaded values are given by

$$f_L = f_0\sqrt{1 + \frac{Z_c X_{ext}}{|Z_{ext}|^2}} \tag{3.8}$$

$$Q_L^{-1} = Q_0^{-1} + \alpha B^2, \tag{3.9}$$

where $\alpha = \frac{\xi L^2}{m\omega_0}\frac{R_{ext}}{|Z_{ext}|^2}$. At any given temperature it is possible to extract Q_0 and α by carrying out measurements as a function of magnetic field strength.

Figure 3.6 illustrates a magnetomotive reflection measurement with a constant current source. The results presented in this thesis (Chapters 4, 5 and 6) were obtained using magnetomotive transmission and balanced-bridge measurements[3]. The circuits for these measurements are described

[3]The reflection technique measures a signal proportional to the mechanical impedance of the beam, which will be highest on resonance. On the other hand, through the transmission technique we measure a signal proportional to the conductance of the beam.

in detail in section 3.4, including simulations which show the behaviour predicted from relations 3.8 and 3.9.

It has to be noted that although the magnetomotive technique works very well for NEMS, it has some disadvantages. Firstly, it requires the use of magnetic fields generated by large superconducting coils, which need to be cooled down to cryogenic temperatures. This is very time consuming as well as expensive because helium transfers are required every two days. Furthermore, it is only possible to detect the odd flexural modes as the EMF voltages are cancelled for the even modes.

3.3 Measurement set-up and techniques

This section describes the equipment and measurement techniques employed for the ultra-low temperature experiments. The set-up and equipment used for the experiments on doubly-clamped gold beams and that for silicon nitride resonators was different and so this section is divided into two parts.

3.3.1 Gold nanomechanical resonator experiments

The cryostat used for this investigation was an Oxford Instruments KelvinoxTLM top loading ^{3}He/^{4}He dilution refrigerator (see Figure 3.7) with a base temperature of (10 ± 1) mK, equipped with a 15.5 T magnet and two rf lines. This cryostat has the benefit of allowing the user to exchange samples whilst the cryostat is operating at ultra-low temperatures; other systems have to be warmed up before the samples can be changed. The measurements were carried out in transmission mode therefore only one device could be measured at a time. The sample was mounted on a 12-pin header and placed inside a brass vacuum can (sealed with an indium O-ring) with electrical feed-throughs to the sample and resistance thermometers (2 kΩ RuO_2 resistors). The feed-throughs were filled with Stycast 2850FT in order to avoid any helium mixture leaking into the vacuum can. The can, along with the support and cables, was immersed in the ^{3}He/^{4}He liquid in the mixing chamber allowing the sample to cool through the wires and substrate. The magnetic field was applied parallel to the plane of the wafer in order to study the fundamental out-of-plane flexural mode of the beam. Two different measurement techniques relying on the magnetomotive scheme (continuous wave and ring-down), were applied to study the motion of the beams.

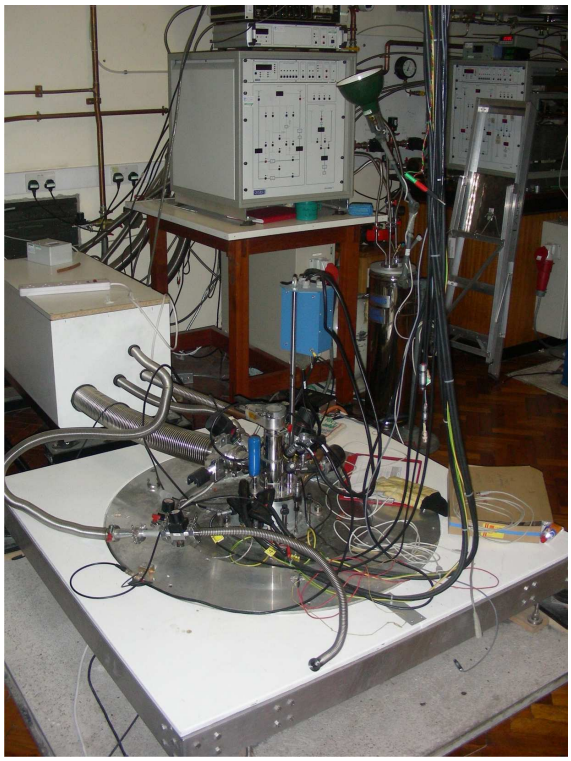

Figure 3.7: The Oxford Instruments KelvinoxTLM ^{3}He/^{4}He dilution refrigerator and KelvinoxIGH gas handling system to the rear of the KelvinoxTLM.

Continuous wave (CW) This technique involved studying the resonator response in the frequency domain, passing an rf alternating current through the beam in the presence of a magnetic field. The response to the resulting Lorentz force was detected by measuring a voltage proportional to the induced EMF as the frequency of the current was tuned through the mechanical resonance. The resonant frequency f_0 and Q-factor were then extracted by fitting the spectrum to a complex Lorentzian function, after a linear background was subtracted (see the last section for more details). Excitation powers of -100 dBm or less were used and care was taken to ensure that the resonator remained in the linear response regime throughout. Typical raw data obtained from this technique is shown in Figure 3.8(a).

Ring-down Measurements were also made using the ring-down approach [59] in which the resonator was excited by 200 μs radio-frequency pulses, spaced 1 s apart, with a frequency close to the mechanical resonance; the re-

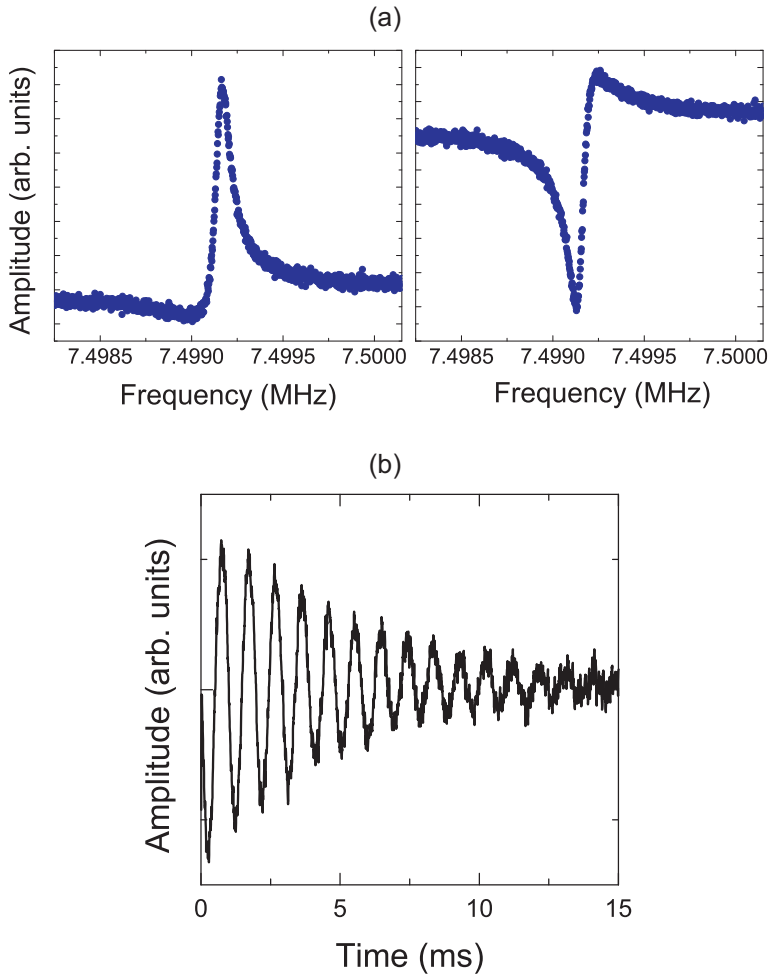

Figure 3.8: (a) The two quadratures corresponding to a typical resonant response of a beam measured using the CW technique. (b) A typical ring-down of a 10.5 μm long gold beam.

sponse of the beam was measured in the time domain. These measurements were only used to extract the Q-factor of the beam as obtaining accurate estimates of the resonator frequency from this method was more problematic because of transient effects. During excitation the resonator moves at the drive frequency. During ring-down, the oscillations come closest to the natural mechanical frequency at later times when the signal is itself rather small. A typical ring-down signal is shown in Figure 3.8(b). The analysis of the CW and ring-down data are discussed in the last section of this chapter.

Heterodyne detection scheme

For both the techniques described above, the response of the beams was captured using a heterodyne detection scheme with an intermediate frequency of 30 MHz as shown in Figure 3.9. Two rf signals, the beam frequency (f_R + 30) MHz from the Agilent E4400B signal generator and the 30 MHz intermediate frequency from the PTS500 signal generator, were fed into the mixer in the transmitter. Low-pass filters inside the transmitter removed the high frequency component (f_R + 60) MHz. The resulting signal at frequency f_R was applied to the sample after passing through a series of variable attenuators which allowed the driving signal to be altered. The response from the resonator was amplified using a +30 dB room temperature rf pre-amplifier [60] and mixed with a signal at frequency (f_R + 30) MHz in the receiver. The output at the intermediate frequency was fed into a second mixer in the receiver to produce a dc signal proportional to the EMF response of the nanomechanical resonator. The data was collected at the 16-bit auxiliary ADC ports of a EG&G 7260 lock-in amplifier. Various filters were used to remove any unwanted high frequency background noise. The CW experiments were controlled by a Labview program written by my colleague M. J. Patton. The TTL pulse generator was controlled by a Matlab routine written by Dr. K. Panesar and was in use only for the ring-down measurements.

3.3.2 Silicon nitride nanomechanical resonator experiments

The equipment and experimental set-up used for the silicon nitride studies were different to that for the gold studies. The cryostat in which the samples were measured was an Oxford Instruments Kelvinox 300 ^{3}He/^{4}He

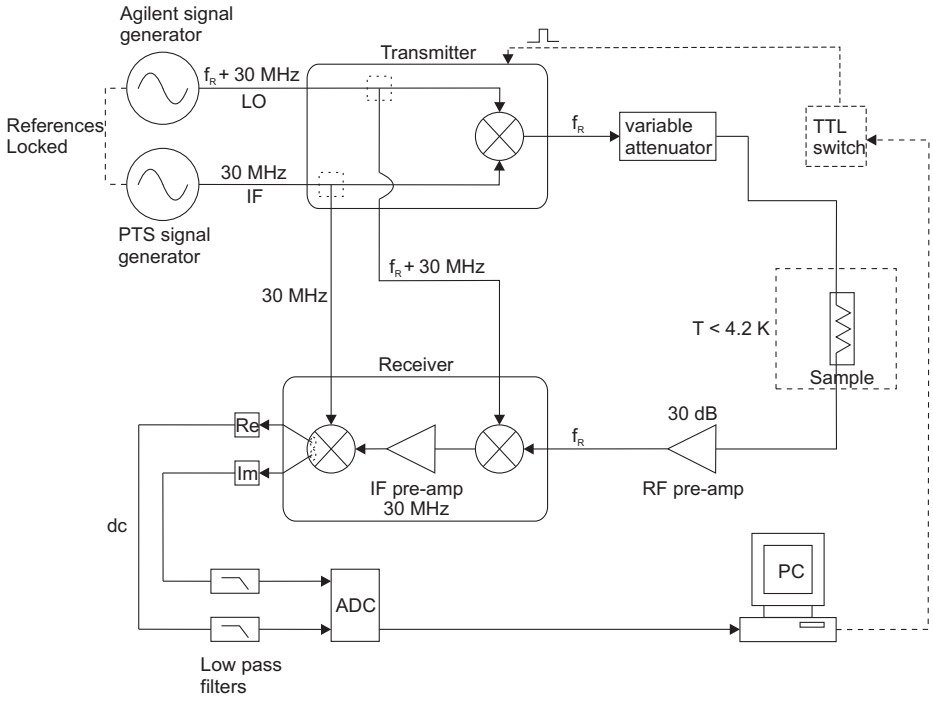

Figure 3.9: Schematic of the heterodyne detection set-up used to perform the magnetomotive measurements. A 30 MHz intermediate frequency (IF) signal is mixed with another rf waveform to generate a signal of the desired frequency in the transmitter. The same IF is used to convert the rf response from the sample to a proportional dc output in the receiver.

dilution refrigerator (Figure 3.10) with a minimum temperature of about 40 mK and equipped with a 12 T superconducting magnet. This particular cryostat offered the possibility to measure more than one sample at a time as there were more rf coaxial lines available than in the top loading fridge. The samples were mounted on a 12-pin header which was plugged into a printed circuit board (PCB). Connections from the sample to the pins were made using a 17 μm diameter aluminium wire and a commercial wedge bonder. The circuit board was designed to provide four 50 Ω coplanar waveguide transmission lines, each of them soldered to an SMA connector for external connections. The sample stage was situated $\sim$31 cm below the mixing chamber flange, at the same level as the centre of the magnetic field. The sample stage was supported by a cylindrical structure ('cold finger') made out of copper and which provided good thermal contact with the mixing chamber (Figure 3.11).

The magnetomotive scheme in conjunction with a balanced-bridge electronic technique [53, 61] was used to study the silicon nitride resonators. In the balanced bridge technique, two devices share the same central branch (see Figure 3.4(b)). The potential of the centre pad is initially held at virtual ground by using a 180° power splitter to drive the two devices out of phase from each other and making the impedance of the two branches of the circuitry similar. High frequency resonators have very small signals and therefore are difficult to resolve in the presence of background noise. This problem is partially resolved by using the balanced-bridge technique (section 3.4 provides a more detailed description).

A schematic diagram of the measurement set-up is shown in Figure 3.12; the different types of coaxial cables employed are colour coded. The sample consisted of two balanced-bridges, separating the two high frequency ($f_0 >$ 30 MHz) and the two low frequency ($f_0 <$ 30 MHz) beams. The output of an Agilent 8712ET network analyzer was sent through a -50 dB fixed attenuator before being split up into two signals using a 180° power splitter and then through another set of variable attenuators before entering the cryostat. The beams were excited using the CW technique by passing an rf current through them and sweeping through the mechanical frequency. The response of the beams was amplified by two +30 dB room temperature rf pre-amplifiers and captured on the network analyzer. The first amplifier [60] was placed just outside the cryostat and the second one [62] at the input of

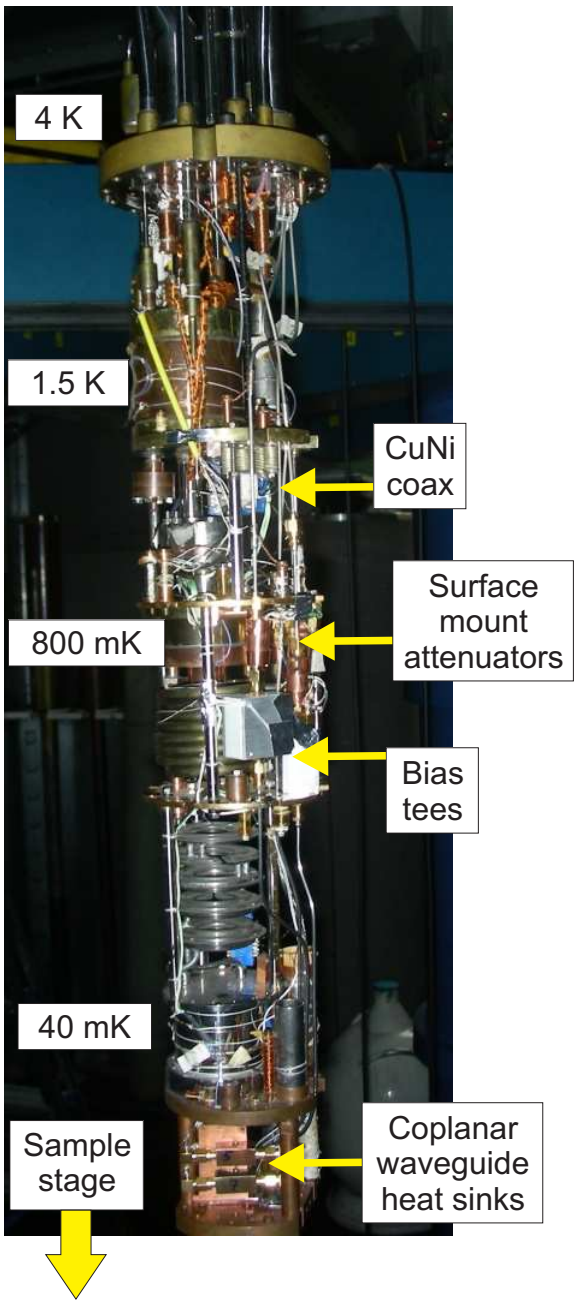

Figure 3.10: Photograph of Oxford instruments Kelvinox 300 dilution refrigerator showing all cables and components from the 4 K flange to the mixing chamber.

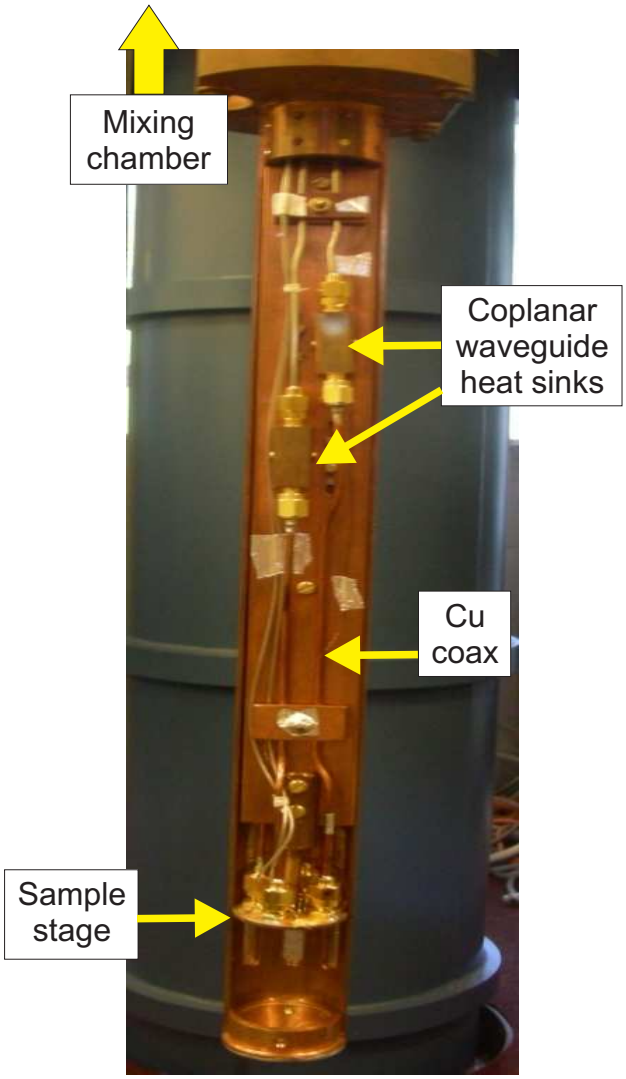

Figure 3.11: Photograph of the Cu cold finger holding the sample stage, thermally anchored to the mixing chamber.

the network analyzer.

Inside the cryostat, between room temperature and the mixing chamber stage, the signals for the high frequency resonators were transmitted through semi-rigid, cupro-nickel (CuNi) coaxial cables as they provide a fairly good thermal insulation between the mixing chamber and the rest of the dilution unit and are less resistive than the flexible stainless steel cables. These lines were connected to surface mount attenuators just below the 1 K pot stage followed by bias tees which, however, were not used in these experiments. The attenuators were soldered onto coplanar waveguides made out of a gold conducting layer on top of a sapphire substrate; this also acted as a heat sink for the central conductor of the coaxial cable. The lines were once again heat sunk at the mixing chamber flange, and between the mixing chamber and the sample stage the signals were transmitted through semi-rigid copper coaxial cables.

The input signals for the low frequency resonators were transmitted through lossy, flexible, stainless steel (SS) coaxial cables from room temperature to the sample stage. The signals were passed via -10 dB attenuators just below the 1 K pot stage and through coplanar waveguide heat sinks at the mixing chamber stage. The response of the beams was transmitted through semi-rigid cables in the same manner as the high frequency signals. In this case, the attenuators were fixed on PCB instead of sapphire.

Photographs, dimensions and room temperature transfer characteristics of a typical 1 dB surface mount attenuator and a coplanar waveguide heat sink are shown in Figures 3.13 and 3.14 respectively. The 1 dB attenuators work well up to about 3 GHz; at higher frequencies the attenuation increases drastically. The gold coplanar waveguide heat sinks only attenuate 0.5 dB up to 1 GHz which is acceptable, especially for home-made components. The purpose of the heat sinks was to thermalize the inner conductor of the coaxial lines while providing 50 Ω transmission; they had a dc resistance between 3-4 Ω.

The room temperature forward transmission (S21) characteristics of all coaxial lines (labelled in Figure 3.12) from the top of the fridge down to the sample space are shown in Figure 3.15. Accounting for the -10 dB (-1 dB) attenuation for the input (output) transmission lines and the -0.5 dB from the heat sinks, the cables themselves attenuate another 0.5 dB which agrees fairly well with Figure 3.15(a). The semi-rigid rf lines behave as

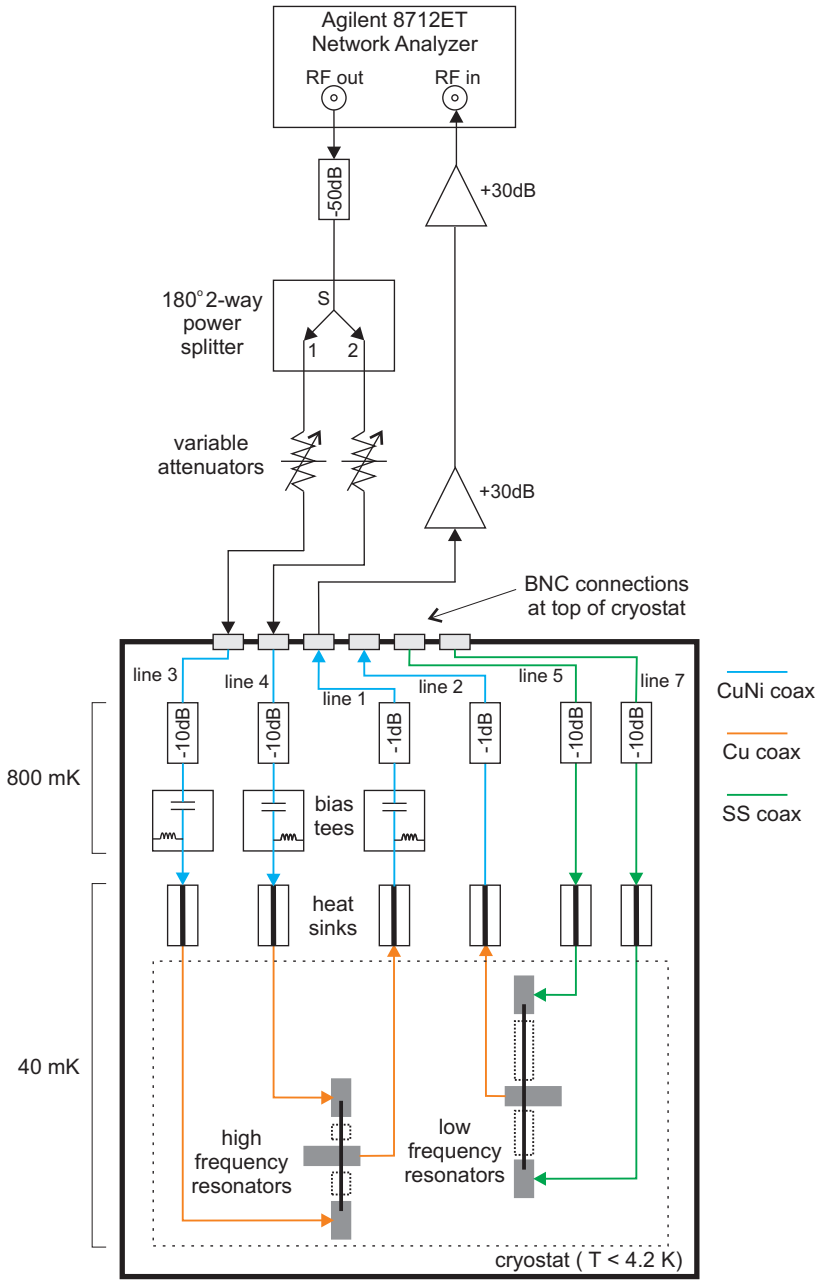

Figure 3.12: Schematic of the measurement set-up and wiring inside the dilution refrigerator for the measurements on gold-coated silicon nitride resonators.

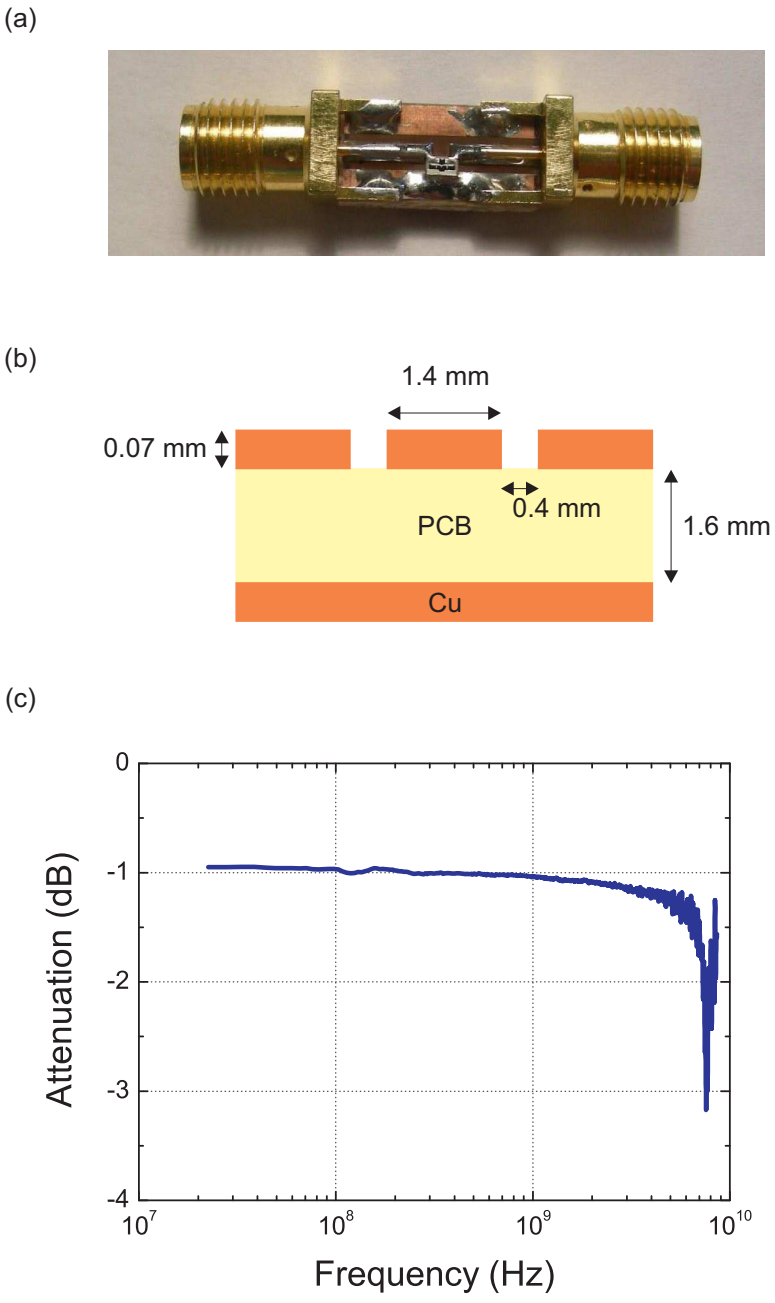

Figure 3.13: (a) Photograph of a 1 dB attenuator fixed onto a coplanar waveguide with PCB as the substrate. (b) Dimensions of the coplanar waveguide. (c) S21 measurements of the 1 dB attenuator.

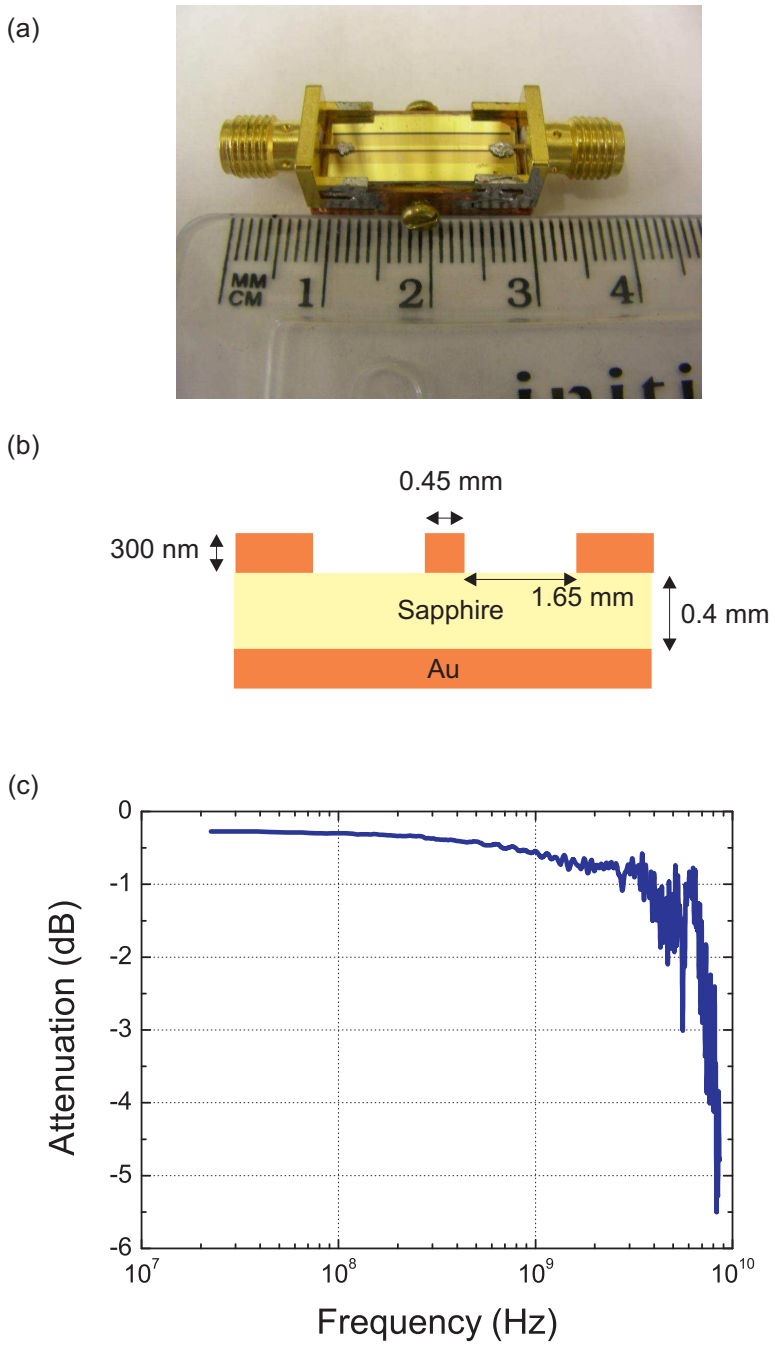

Figure 3.14: (a) Photograph of a coplanar waveguide heat sink. The conducting layer is Au, the substrate is sapphire. (b) Dimensions of of the heat sink. (c) S21 measurements of the Au coplanar waveguide.

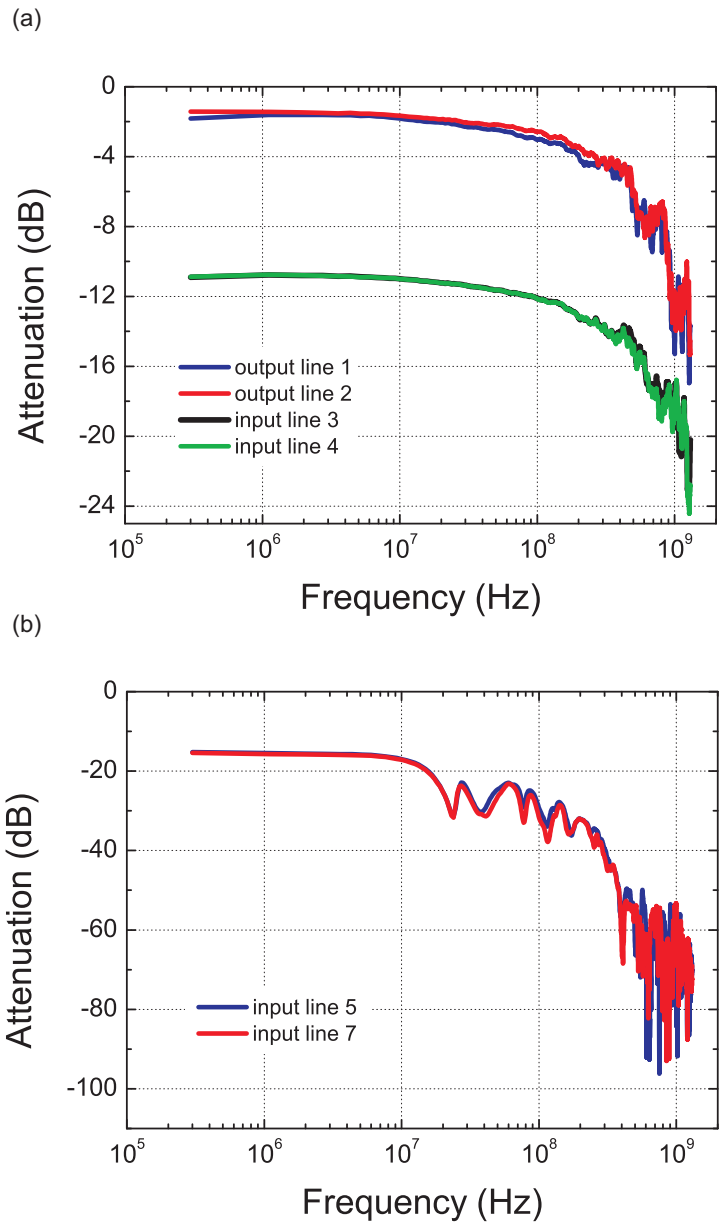

Figure 3.15: (a) S21 measurements of the semi-rigid coaxial lines from the top of the fridge to the sample space. (b) S21 measurements of flexible SS coaxial lines. All measurements done at room temperature.

expected up to 100 MHz. The flexible coaxial lines on the other hand are more lossy and unpredictable; below 20 MHz the attenuation is as much as -15 dB but above that frequency the attenuation fluctuates, increasing to more than -60 dB above 500 MHz (Figure 3.15(b)). This could be due to the fact that the flexible cables were wrapped around Cu pillars at several stages in the fridge in order to thermalize them and because their length was much longer than required. The bending of the cables may have caused such transmission behaviour at high frequencies. All resonant frequencies reported in this thesis are below 100 MHz, a region in which the cables worked quite well. Transmission through cables and other rf components changes slightly with temperature; unfortunately I do not have data for the transfer characteristics for any of the rf lines at low temperatures.

The temperature of the sample stage was monitored using a 2 kΩ RuO_2 chip resistor. The resistor was glued to the sample stage using GE varnish, and its resistance was determined using a 4-wire measurement and an AVS resistance bridge. Twisted pairs connected the bridge to the resistor. The RuO_2 resistance at the sample stage was calibrated against the one at the mixing chamber stage by letting the fridge stabilize for a couple of hours at several temperatures between 4 K and 40 mK. The resistances of both chip resistors were then measured and assuming that both stages were at the same temperature, a calibration chart for the sample stage resistor was produced.

3.4 Measurement circuits

In this section we describe the models for the measurement circuits employed for the experiments described in Chapters 4, 5 and 6. The gold and the silicon nitride (with thin gold electrode) nanomechanical resonators were measured in transmission mode, looking at a dip in the conductance of the beam. The silicon nitride beams with a thicker gold layer were measured using the balanced-bridge technique. In both cases, a constant voltage source was used. The simulated data were fitted to the same Lorentzian function used to fit all the experimental data in order to confirm that the measured signals (in volts), indeed provide us with information about the Q-factor of the nanomechanical resonator.

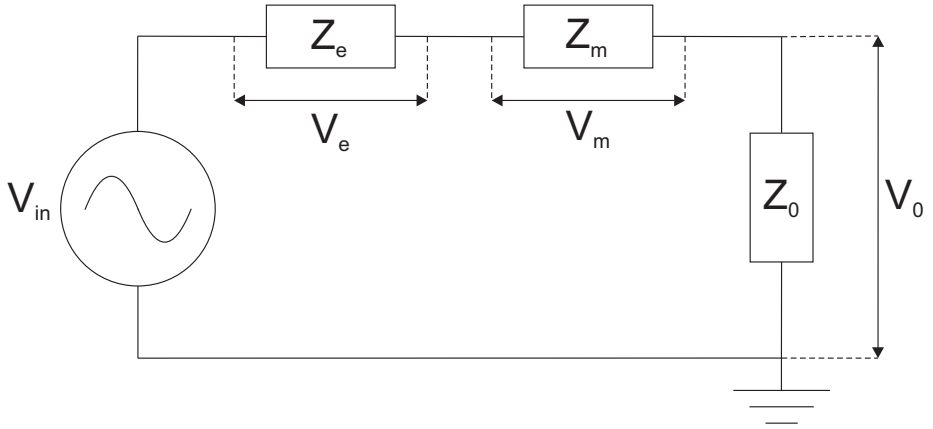

Figure 3.16: Circuit model for magnetomotive transmission measurements, with external circuit impedances Z_e and Z_0, sample impedance Z_m, with the drive voltage V_{in} and the measured voltage V_0.

3.4.1 Transmission

Figure 3.16 illustrates the electrical circuit for a magnetomotive transmission measurement, with a voltage source instead of a current source. The drive and measured voltage signals are denoted by V_{in} and V_0, respectively. The impedances of the input and output coaxial lines are Z_e and Z_0, and the device impedance is Z_m. We assume that all voltages and currents are oscillating at the same frequency in the long time limit, thereby neglecting any transients.

In a magnetomotive set-up, the electrical equivalent of a resonator is a parallel combination of an inductor L_m, a capacitor C_m and a resistor R_m. Hence, the resonator impedance has the form:

$$Z_m = \frac{\frac{i\omega}{C_m}}{\omega_0^2 - \omega^2 + \frac{i\omega}{C_m R_m}}, \tag{3.10}$$

where ω is the drive frequency and ω_0 is the resonant frequency. Equation 3.10 has the typical Lorentzian shape. As all the impedances are in series, the same current flows through each element:

$$I = \frac{V_e}{Z_e} = \frac{V_m}{Z_m} = \frac{V_0}{Z_0}. \tag{3.11}$$

The voltages add, $V = V_e + V_m + V_0$, which gives the relation between the

measured and drive signal as

$$\frac{V_0}{V_{in}} = \frac{Z_0}{Z_e + Z_m + Z_0}. \tag{3.12}$$

Analytically solving equation 3.12 to obtain the relations[4]

$$f_L^2 = f_0^2 + \beta B^2 \tag{3.13}$$

and

$$Q_L^{-1} = Q_0^{-1} + \alpha B^2 \tag{3.14}$$

is not trivial. Instead, simulations were carried out, as a function of magnetic field, using parameters similar to those for the 7.5 MHz thin gold silicon nitride nanomechanical resonator, to prove that the above expressions still hold for transmission measurements. Table 3.1 shows the parameters used for the simulations.

Table 3.1: Parameters used for the magnetomotive transmission simulations.

Length (μm)	25.5
thickness (nm)	170 (Si_3N_4) + 40 (Au)
width (nm)	170
total mass (kg)	5.34×10^{-15}
f_0 (MHz)	7.499200
Q_0	10^6
Z_0 (Ω)	50
Z_e (Ω)	50 - i10

Curves representing the function $\frac{V_0}{V_{in}}$ were generated for twenty different magnetic fields in the range 0.02 - 3 T, an example of which is illustrated in Figure 3.17. The real and imaginary parts are plotted against each other to form a circle, a behaviour characteristic of Lorentzian functions. The real and imaginary parts of the simulated curves were fitted in the same manner as the experimental data (see section 3.5, Chapter 3) in order to extract the Q-factors and resonant frequencies f_L.

Figures 3.18(a) and (b) show a plot of Q_L^{-1} and f_L^2 as a function of B^2, with the simulated data following the trend of equations 3.13 and 3.14. The

[4]Equations introduced in section 3.2, they describe the loading effect of the magnetic field and the external circuitry on the resonant frequency and Q-factor of the nanomechanical beam.

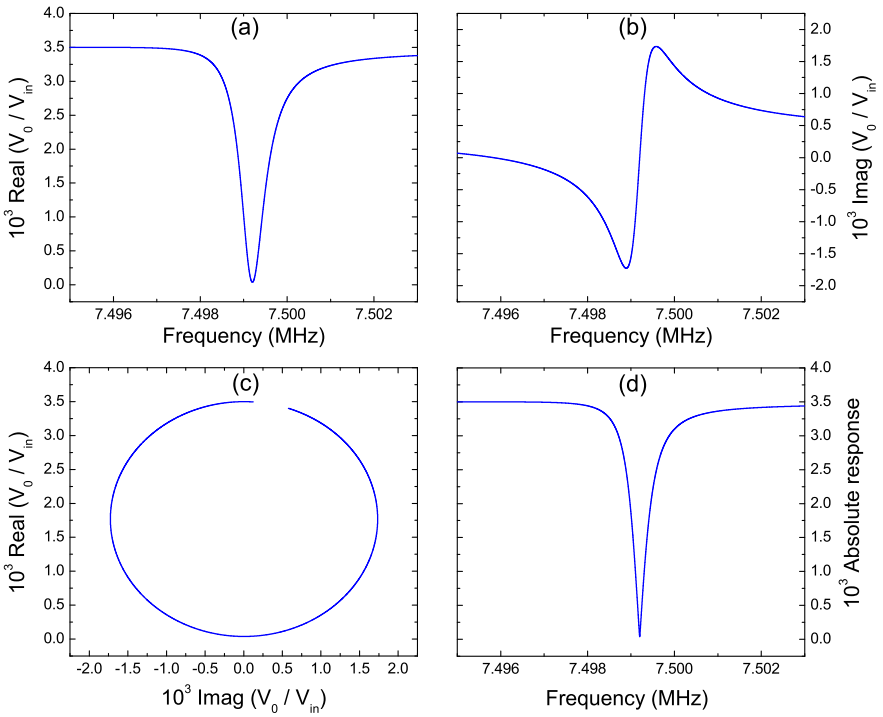

Figure 3.17: Simulations showing the (a) real, (b) imaginary parts of the function $\frac{V_0}{V_{in}}$, which trace out a circle (c) when plotted against each other. The absolute response is shown in (d).

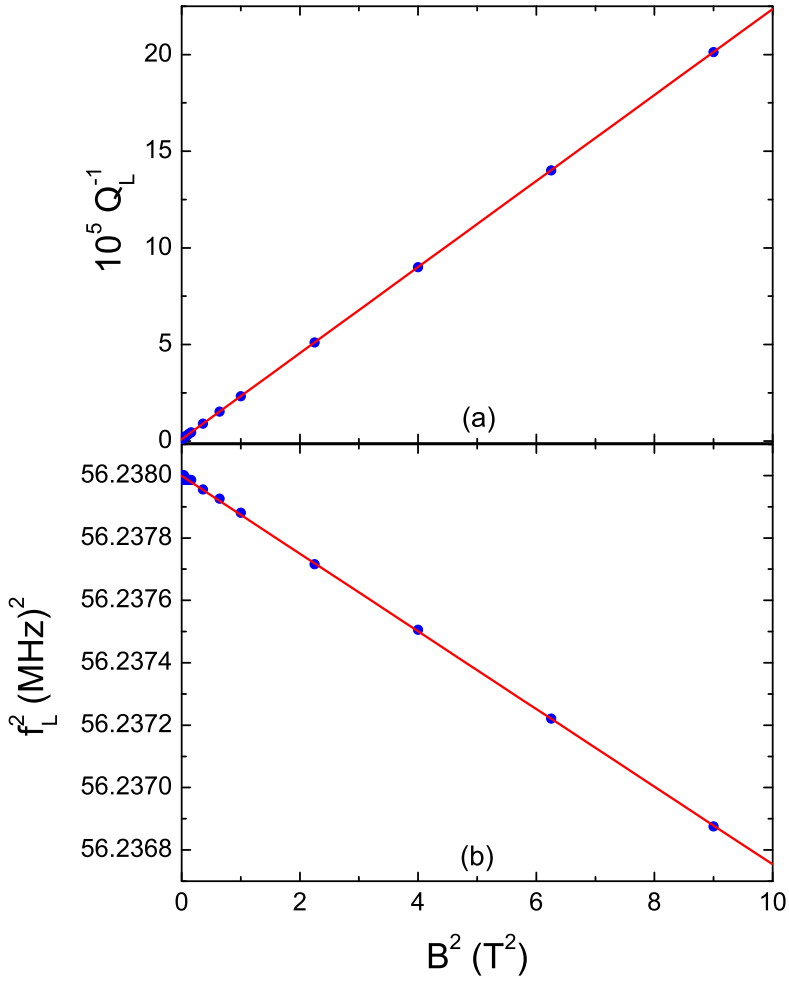

Figure 3.18: (a) Loaded dissipation and (b) resonant frequency as a function of B^2. The smooth lines are linear fits to the data from which the intrinsic dissipation and resonant frequency were obtained.

smooth lines are linear fits to the data from which we obtained Q_0 and f_0. The fitted values are $Q_0 = 10^6$ and $f_0 = 7.4992$ MHz, in agreement with the values initially set (see Table 3.1), as expected. Furthermore, the fitted gradients α and β are also in agreement with the model. These simulations essentially prove that the voltage signals measured will provide us with the real Q-factor and resonant frequency of the device, in the limit of $B = 0$.

3.4.2 Balanced-bridge technique

The use of a balanced bridge technique for the electronic detection of displacement of a nanomechanical resonator was first implemented by the Roukes Group (CALTECH, USA) [53]. Measuring the motion of nanomechanical resonators becomes more challenging as the frequency is increased. This is because the mechanical resistance ($R_m = \frac{\xi L^2 B^2 Q_0}{\omega_0 m}$) of such devices diminishes very quickly as their resonant frequency is increased, as does the Q-factor which means that $R_m \ll R_e$, where R_e is the total resistance of the external measurement circuit. Hence it becomes very difficult to measure the tiny resonance signal embedded within a large parasitic background signal. This problem is solved by using a bridge, as shown in Figure 3.19, where Z_{m1} and Z_{m2} are the impedances of two separate nanomechanical resonators and PS is a 2-way, 180 degree power splitter.

The following relations apply to the circuit in Figure 3.19:

$$I = I_1 + I_2 \tag{3.15}$$

$$V_{in} = I_1(Z_e + Z_{m1}) + V_0 \tag{3.16}$$

$$V_{in} = -I_2(Z_e + Z_{m2}) - V_0 \tag{3.17}$$

$$V_0 = IZ_0. \tag{3.18}$$

Rearranging equations 3.16, 3.17 and 3.18 and substituting them into 3.15 leads to the following expression

$$V_0 \left(\frac{1}{Z_0} + \frac{1}{Z_e + Z_{m1}} + \frac{1}{Z_e + Z_{m2}} \right) = V_{in} \left(\frac{1}{Z_e + Z_{m1}} - \frac{1}{Z_e + Z_{m2}} \right), \tag{3.19}$$

which can be further simplified to obtain the ratio of the measured to the

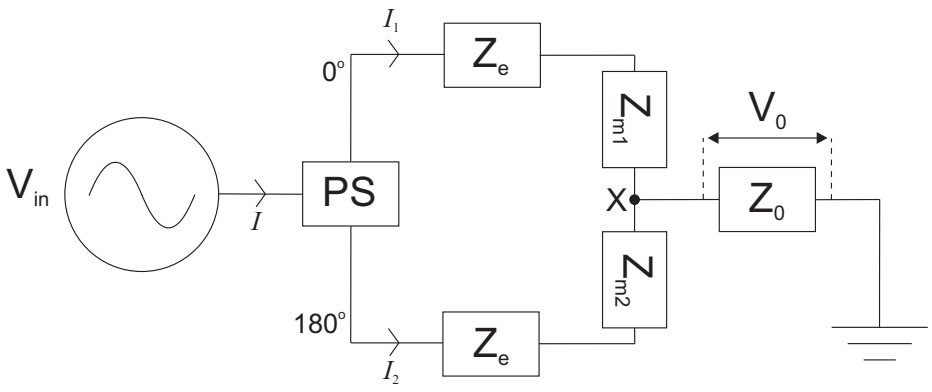

Figure 3.19: Schematic diagram of a circuit for balanced bridge measurements.

drive voltage:

$$\frac{V_0}{V_{in}} = \frac{Z_{m2} - Z_{m1}}{(Z_{m1} + Z_{m2})\left(1 + \frac{Z_e}{Z_0}\right) + Z_e\left(2 + \frac{Z_e}{Z_0}\right) + \frac{Z_{m1}Z_{m2}}{Z_0}}. \tag{3.20}$$

For the situation where $Z_{m1} \approx Z_{m2}$, then equation 3.20 clearly suggests that off resonance, the voltage at point X will be nulled, as expected for a bridge measurement. Furthermore, the signals corresponding to the two resonators will be 180 degrees out of phase, as shown by the simulated curves in Figure 3.20(a) and (b). The absolute response from both resonators will always increase on resonance (Figure 3.20(c)). A good balanced-bridge measurement requires two resonators of similar dimensions (and resonant frequencies), in order for the background signal to be cancelled in the off-resonance regime.

The signals obtained from these bridge measurements have the same magnetic field dependence as those from transmission measurements (linear in B^2) which further confirms that, with both measurement techniques, the measured is a signal is proportional to the EMF generated by the device. By extrapolating to $B = 0$, it is possible to extract the intrinsic properties (f_0, Q_0) of the nanomechanical resonator.

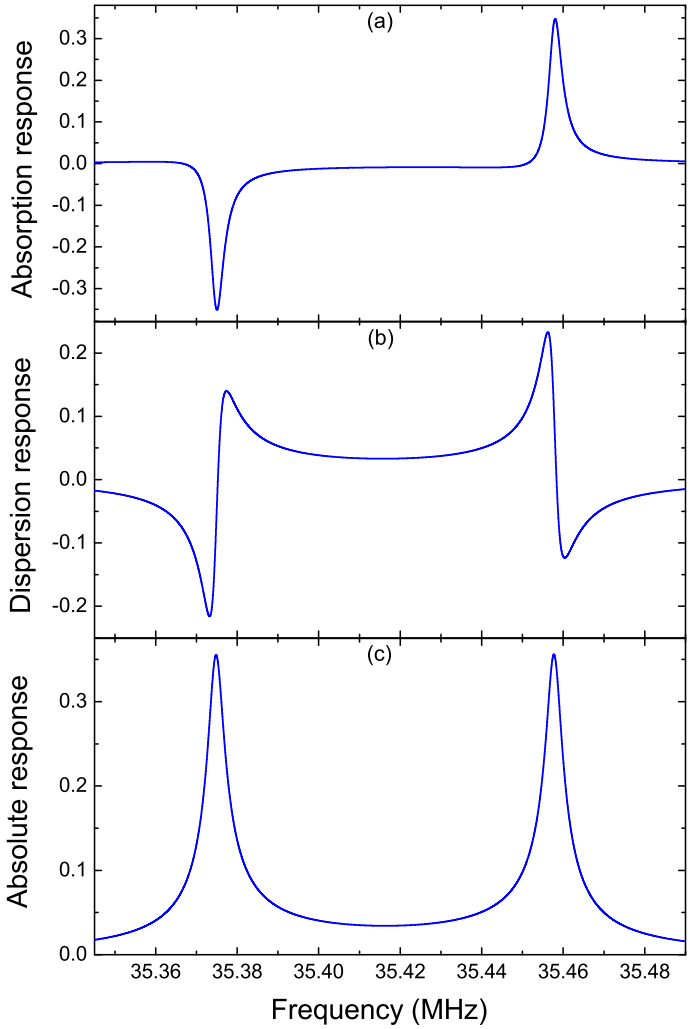

Figure 3.20: (a) Absorption, (b) dispersion and (c) absolute responses of two resonators forming a balanced bridge.

3.5 Resonant response analysis

This section describes a procedure to accurately extract the resonant frequency and Q-factor from the raw data obtained using the CW (spectral domain) and ring-down (time domain) techniques.

3.5.1 Spectral domain

At small amplitudes a resonator's motion can be modelled as a harmonic oscillator with a Lorentzian shaped resonant response. The method to fit the resonance curves obtained from the frequency domain measurements has been adapted from the method described in a thesis by I. Kozinsky [23]. For a Lorentzian superimposed on a background signal, the oscillator response R has the following form:

$$R(\omega) = \frac{\frac{Ae^{i(\theta-\frac{3\pi}{2})}\omega_0^2}{Q}}{(\omega_0^2-\omega^2)+\frac{i\omega_0\omega}{Q}} + B_0 + B_1(\omega-\omega_0), \tag{3.21}$$

which allows for a full 8-parameter fit (A_x, A_y, ω_0, Q, $B0_x$, $B0_y$, $B1_x$, $B1_y$). A is the resonant peak amplitude, ω_0 the resonant frequency of the beam, Q its quality factor, the complex values B_0 and B_1 are the constant and frequency varying components of the background signal, respectively. The subscripts x and y correspond to the two quadrature components of the data. The raw data are fitted to the above equation, the real and imaginary parts being fitted separately.

The initial step is to fit the x and y components of the data to trace out a circle in the xy-plane; this allows an estimate of the peak amplitude A which is given by the diameter of the circle. The phase factor $e^{i(\theta-\frac{3\pi}{2})}$ in the above equation accounts for the background phase, which shifts the circle from its zero background position (which is the origin). For convenience, this phase is incorporated into the complex amplitude A [23]. The next step is to fit the experimental values of $\frac{d\theta}{d\omega}$ which are background free and hence can be fitted to provide more accurate estimates of the resonant frequency and the Q-factor (details on how this is done are given in reference [23]). These values are then used as initial guess parameters to fit equation 3.21 to the raw data. An example of raw data for a 7.5 MHz silicon nitride resonator fitted according to this method is illustrated in Figure 3.21(a).

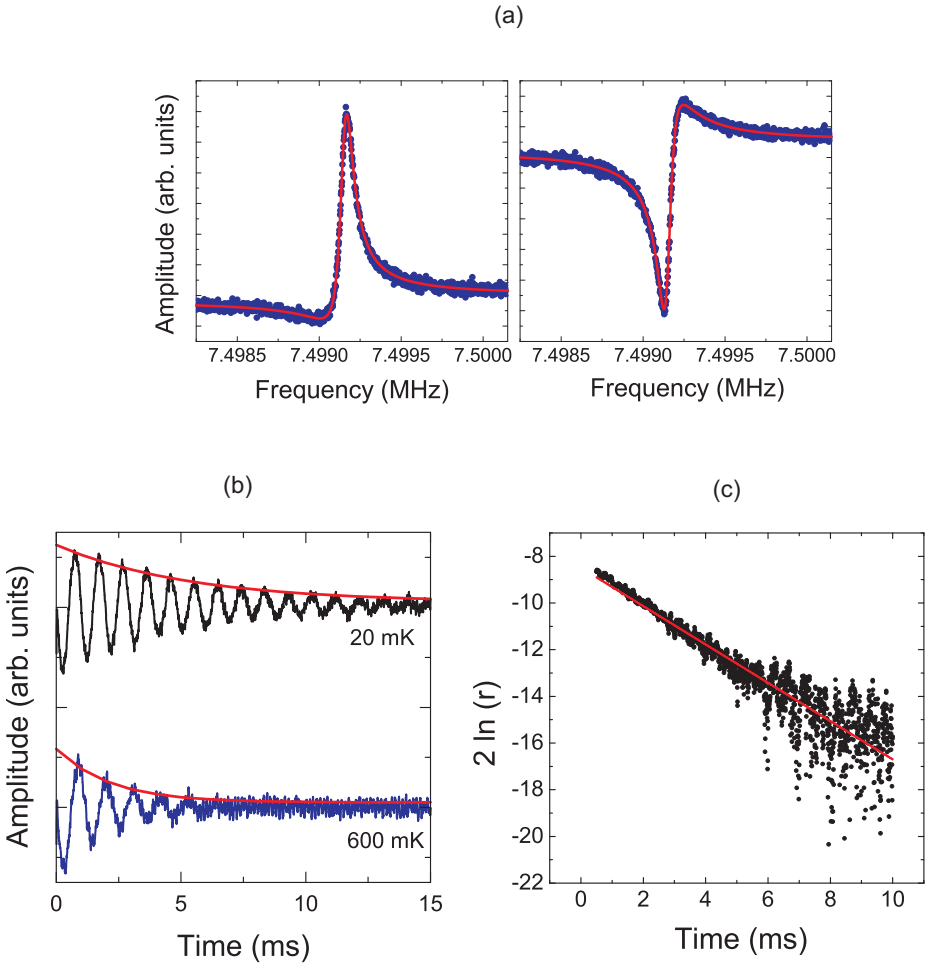

Figure 3.21: (a)Typical real and imaginary parts of the measured magnetomotive response of a 7.5 MHz silicon nitride sample. The smooth line is a Lorentzian fit to the data. (b) Typical data for a 3.87 MHz gold resonator taken at 1 T; the smooth lines are exponential fits to the envelope. (c) Plot of ln (r) as a function of time, the smooth line is a linear fit to the data from which τ can be extracted.

3.5.2 Time domain

Ring-down data can be analyzed by using a fast Fourier transform (FFT) and then fitting the real and imaginary parts as outlined in the previous section. However, an alternative way to extract the resonant frequency and Q factor is to look at the time variation of the amplitude. In the time domain, the x and y components of the amplitude have the form $x = e^{-t/\tau}\sin(2\pi ft)$ and $y = e^{-t/\tau}\cos(2\pi ft)$ with the envelope $r = \sqrt{x^2 + y^2}$. By fitting an exponential function to the envelope of the resulting oscillations or alternatively, from a linear plot of $\ln(r)$ vs t we can extract the time constant τ of the resonator. The phase θ can be extracted from a plot of x vs y and the resonant frequency of the resonator can be deduced from the rate of change of phase. Once f_0 and τ are known, the quality factor is calculated using the expression [1]

$$Q = \frac{\omega_0 \tau}{2}. \tag{3.22}$$

This method gives accurate values for the Q-factor without the effects of frequency varying background noise. Furthermore the values can be obtained from simple linear fits, whereas in the frequency domain a more complicated 8-parameter nonlinear fit has to be used. Typical ring-down data for a gold nanomechanical resonator is shown in Figure 3.21(b) and (c); raw data corresponding to two different temperatures are shown with the smooth lines being fits to the data.

3.6 Summary

In this chapter we discussed the fabrication of doubly-clamped gold beams and gold-coated high-stress silicon nitride nanomechanical resonators used for the low temperature dissipation studies. The gold nanomechanical resonators were fabricated using a combination of e-beam lithography and wet etching techniques; the silicon nitride devices were patterned using a combination of optical and e-beam lithography, and released through dry etch. The magnetomotive transduction scheme was used to study the motion of the nanomechanical beams. The measurement set-ups for the experiments were explained as well as the techniques used to capture the EMF signal corresponding nanomechanical motion.

Chapter 4

Dissipation in gold nanomechanical beams at millikelvin temperatures

This chapter describes the results of a study of dissipation and frequency shift in two polycrystalline gold nanomechanical resonators at temperatures between 10 mK and 2 K. Metal resonators are being used more frequently in low temperature experiments since the fabrication is simplified when an underlying dielectric layer is not required [7, 63–65]. Furthermore, the Q-factor of these resonators has been found to be relatively large, although the temperature dependence of the dissipation has not been studied systematically. As metal resonators are readily fabricated and actuated as monolithic structures, the interpretation of the dissipation measurements is simpler than for dielectric ones where metallization is typically required to facilitate actuation [45, 47, 59, 66].

The fabrication of the devices and the experimental set-up for the measurements have already been described in Chapter 3. This chapter is divided into four sections, the first describes the effect of cooling on the resonant frequencies of the devices. The study of magnetic field dependence is presented in the second section explaining how it is used to determine the intrinsic dissipation in the resonators at any given temperature. Then follows the results showing the temperature dependence of dissipation and resonant frequency. The last section includes a review on the most recent experiments on metallic nanomechanical resonators carried out by other research groups.

4.1 Device frequencies

The resonant frequency of nanomechanical resonators can depend significantly on the tension, T_0, in the structure. Some of the tension can come from the evaporation of the metal film, however most of the tensile stress in a metallic resonator arises from the difference in the thermal contraction between the substrate (GaAs) and the metal (Au) when the device is cooled down to low temperatures. To a good approximation a doubly-clamped beam of length L under tension T_0 has a fundamental frequency given by [22]

$$f_{0n} = \frac{\pi}{8}(2n+1)^2 \frac{1}{L^2}\sqrt{\frac{EI}{\rho A}}\sqrt{1+\frac{0.97T_0L^2}{(n+1)^2\pi^2EI}},$$

an equation already introduced in Chapter 2. Using bulk values for the Young's modulus (E = 78 GPa) and density (ρ = 19300 kgm^{-3}) of gold [23], the expected resonant frequencies without any stress (T_0 =0) are 3.0 and 1.24 MHz for the beams with length 7.5 and 10.5 μm respectively. The tension in the beams can be estimated as $T_0 = EA\left(\frac{\Delta L}{L}\right)$ where $\frac{\Delta L}{L} = \left(\frac{\Delta L}{L}\right)_{Au} - \left(\frac{\Delta L}{L}\right)_{GaAs}$ is the difference in the relative thermal contraction of gold and GaAs. An estimate for the differential thermal contraction of gold is 3.1×10^{-3} [63, 67] and 9.205×10^{-4} for GaAs [68]. These values were used to calculate an estimate for the tensile stress, $\sigma = \frac{T_0}{A}$, in the beams, when cooled from room temperature down to liquid helium temperatures, of about 170 MPa, leading to predicted resonant frequencies of 7.55 and 5.10 MHz for the beams with lengths 7.5 and 10.5 μm respectively.

The measured frequency for the shorter beam was 7.95 MHz but for the longer beam it was 3.87 MHz. The extremely good level of agreement between the observed resonant frequency and the predicted value for the shorter beam is fortuitous given the inherent uncertainties such as the material properties of the system. On the other hand, the 10.5 μm long beam has a lower resonant frequency than expected (by about 35%). This deviation is most probably due to initial compressive strain which was found (based on our experience of fabricating a number of resonators using the same process) to be generated in varying degree during the fabrication process. Figure 4.1 clearly shows the effect of the tension, due to cooling, on the resonant frequency of the 3.87 MHz beam from 20 K to 10 K. The tension in the beam keeps increasing down to about 10 K, which can be inferred

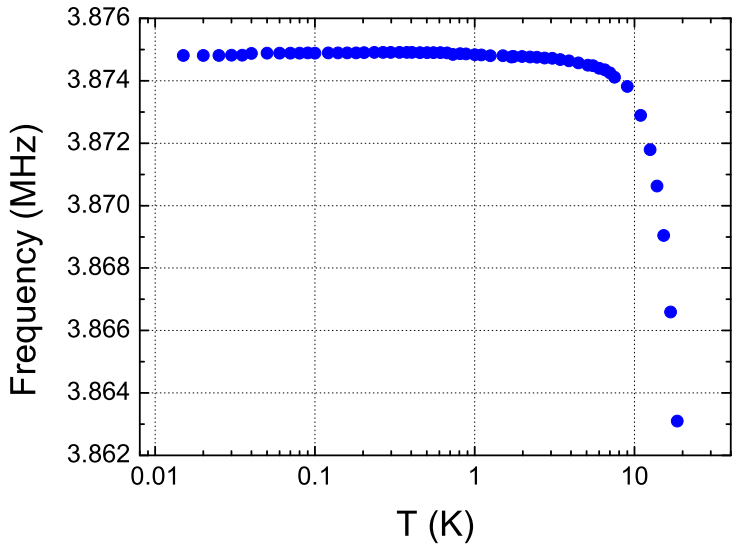

Figure 4.1: Plot of frequency versus temperature for the 3.87 MHz resonator clearly showing the effect of cooling on the resonant frequency of the device. Up to 10 K, the frequency is relatively constant but above 10 K, the frequency starts to drop very quickly as expected.

from the rapid increase in the resonant frequency, however below 10 K, the resonant frequency is roughly constant. A similar behaviour was seen for the 7.95 MHz beam, in measurements carried out during the cool-down, the resonator frequency shifted up from 7.38 MHz to 7.95 MHz as the temperature was reduced from 77 K to 10 K.

4.2 Magnetic field dependence

Use of the magnetomotive transduction scheme results in a measured Q-factor which is loaded by the external circuitry and the electrical resistance of the sample itself. Measurements of the magnetic field dependence of the resonator response were used to extract the resonator's intrinsic Q-factor, Q_0 [27, 59]. The drive and detection circuits for the measurement system each have a 50 Ω characteristic impedance along with some resistance due to the cables and the sample, ∼35 Ω for the 7.95 MHz beam and ∼75 Ω for the 3.87 MHz beam (resistances measured at 4 K). Assuming that the external

impedances presented to the sample are effectively resistive, estimates for the parameter $\alpha = \frac{\xi L^2}{m\omega_0} \frac{R_{ext}}{|Z_{ext}|^2}$ can be calculated, using appropriate values for the mass of the beams and the external impedances. The predicted values of α are 2.39×10^{-6} T^{-2} (3.87 MHz resonator) and 7.86×10^{-6} T^{-2} (7.95 MHz resonator).

The dissipation as a function of magnetic field B was measured for both beams at a range of different temperatures. Figure 4.2(a) and (b) shows plots of the dissipation as a function of B^2 for both samples. It is clear that the magnetic field can cause a substantial change in the dissipation. As expected, the behaviour is found to be linear in B^2 and the gradient (α) allows Q_0^{-1} to be obtained by extrapolation to zero field. The linear fits to the data yield values of α close to the predicted gradients however it can be noticed that α has a very weak temperature dependence, which can be attributed to the fractional changes in cable impedances with field and temperature. Figure 4.3 shows the weak dependence of α on temperature for both gold beams; the solid lines are linear fits using the equation $\alpha = \alpha_0 + \alpha_1 T$. For both devices, α_1 is negligible compared to the temperature independent value. Furthermore, the errors in α are relatively large, hence a simple average of the measured gradients (illustrated by the dashed lines in Figure 4.3) was used to determine Q_0 at arbitrary temperatures. The insets in Figure 4.2 show plots of the resonant frequency shift (with respect to $f_0(B = 1\text{T})$); no corresponding magnetic field dependence was found for the resonant frequency of the devices confirming that the impedances seen by the sample can be treated as essentially real.

4.3 Temperature dependence

Measurements of the Q-factor and frequency of the 7.95 MHz resonator were carried out from about 1 K down to 10 mK using the CW technique at B=3 T as it provided an acceptable signal-to-noise ratio over the whole range of temperatures studied. For the 3.87 MHz device, CW measurements were made at 2 and 3 T, as well as ring-down measurements at 1 T in temperatures ranging from about 2 K down to 10 mK. The ring-down technique allowed measurements in fields as low as 1 T where the magnetomotive damping is minimal. Therefore the correction required to extract Q_0 using equation 3.9 is also smaller than for higher fields.

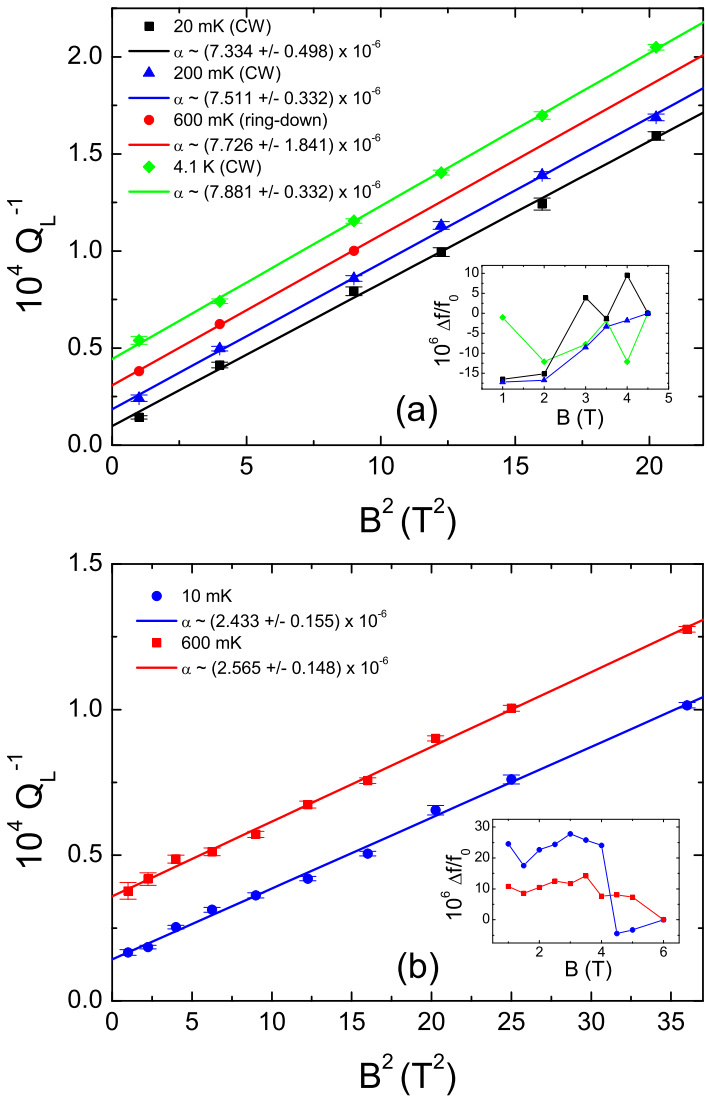

Figure 4.2: Dissipation, Q_L^{-1}, versus B^2 for the (a) 3.87 MHz resonator and the (b) 7.95 MHz resonator. The straight lines are linear fits to the data from which α was extracted. The insets show the change in frequency of the beams as a function of magnetic field.

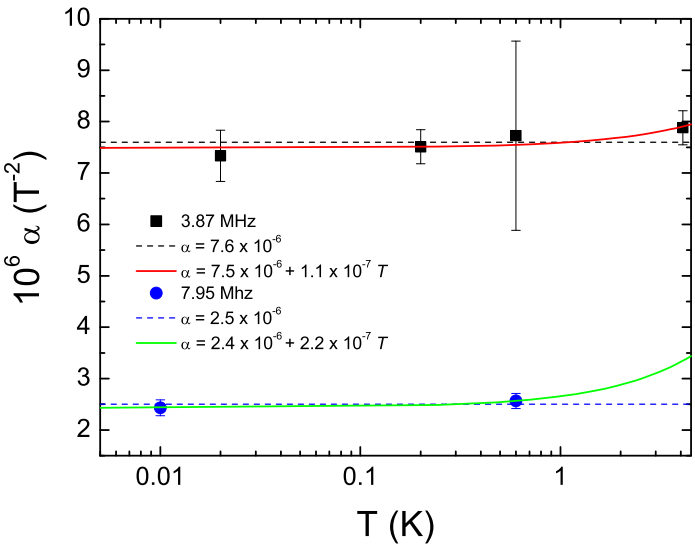

Figure 4.3: Semilog plot of α versus temperature T for both gold beams. The dashed lines represent the average value of the data. The solid lines are linear fits to the data.

4.3.1 Dissipation

Figures 4.4(a) and (b) show the temperature dependence of the intrinsic dissipation, Q_0^{-1}, for both samples. In both plots, the data follow a common pattern and three different regions of behaviour can be identified. Above about 600 mK the dissipation saturates, reaching what appears to be a plateau while saturation is also observed for the data below about 30 mK. In the intermediate region between 30 and 500 mK, fits to the data show that the behaviour of both devices is described by a power law T^n, with $n = 0.50\pm$ 0.05 for the 7.95 MHz device and $n = 0.49 \pm 0.02$ for the 3.87 MHz device. For the latter, the individual data sets (corresponding to different fields) were first fitted separately to obtain the respective power laws, all of them lying in the range 0.47-0.52. Furthermore, the different sets of data, taken at different fields and using different techniques overlay one another as shown in Figure 4.4(b). This strongly suggests that the results are independent of the measurement methods used. Estimates for the dissipation in the plateau regions at the high temperatures (shown as dashed lines in the plots) are obtained by averaging over the five points taken at the highest temperatures for each sample. Very similar results were obtained for both

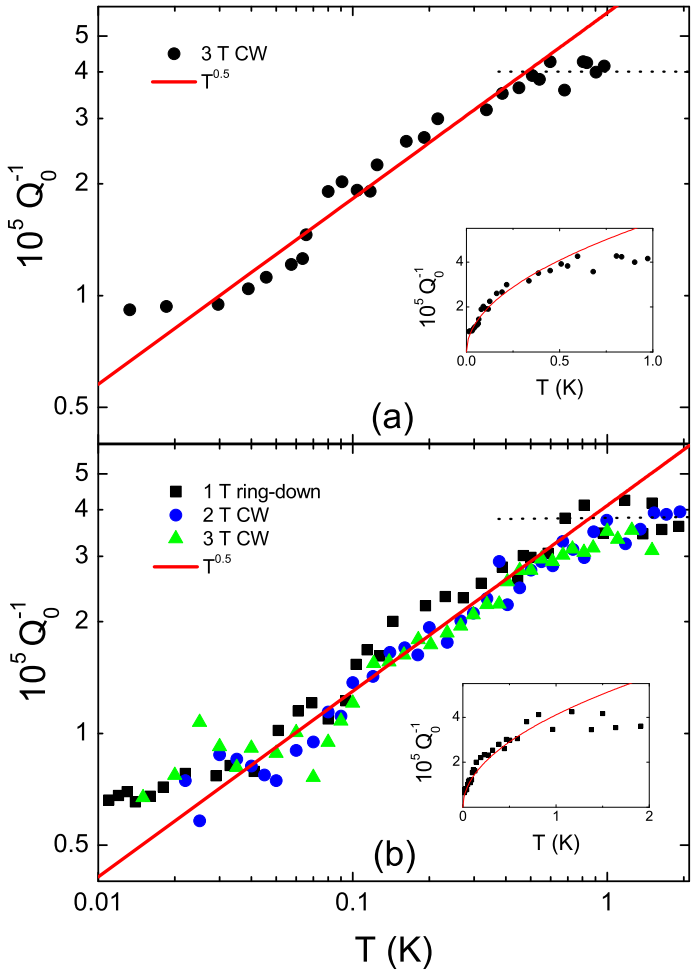

Figure 4.4: Q_0^{-1} as a function of temperature, on a log-log scale (main plot) and a linear scale (inset) is shown for the (a) 7.95 MHz resonator and (b) 3.87 MHz resonator. In each plot, the full line (curve in the insets) is a guide to the eye $\propto T^{0.5}$. The dashed line is the average of the five points at the highest temperatures.

devices: $Q_{p,s}^{-1} = 4.1 \times 10^{-5}$ and $Q_{p,l}^{-1} = 3.8 \times 10^{-5}$ for the 7.95 and 3.87 MHz resonators respectively (the subscript p refers to plateau, s for short beam and l for long beam). Figure 4.5 shows a plot of the loaded quality factor, Q_L^{-1}, as a function of temperature for both beams measured at different magnetic fields. The solid curves represent the expression $bT^{0.5} + \alpha B^2$, b being a constant of proportionality obtained from the fits to the Q_0^{-1} data. The main aspect to notice in this plot is the evident saturation of the dissipation at the highest temperatures.

The saturation in the dissipation at the lowest temperatures could be due to a variety of factors including a crossover to a regime where a temperature-independent mechanism such as clamping losses or Joule heating of the sample dominates. However, simple calculations show that neither of these are expected to have a significant effect on the devices measured. A simple estimate of the clamping loss in the devices was obtained using an equation provided in reference [26], giving values in the range $Q_{clamp}^{-1} \sim 10^{-9} - 10^{-10}$. Although the effects of tension are not included in this calculation, it nevertheless seems unlikely that this mechanism could cause saturation. However, a more detailed theory on clamping losses in nanomechanical resonators, which includes the effect of tension in the devices, is required to determine conclusively whether this mechanism is likely to be relevant here. On the other hand, it is expected that the Joule heating of the resonator should increase the temperature of the sample by only about 1 mK at 10 mK, but other mechanisms which are harder to quantify such as heat conduction along the coaxial cables may play an important role at the lowest temperatures.

4.3.2 Resonant frequency

The relative shift in the frequency of the resonators as a function of temperature is shown in Figure 4.6(a) and (b). For the 3.87 MHz resonator, both the 2 T and 3 T data have been plotted for comparison however the data at 2 T is likely to be more accurate as it provides the best compromise between linewidth and signal-to-noise ratio. For both samples, there is an increase in frequency with temperature over the lower half of the temperature range. The behaviour here is well described by a logarithmic dependence (already introduced in Chapter 2), given by $\frac{\Delta f}{f_0} = C_{s(l)} \ln \frac{T}{T_0}$ with gradients $C_s = (7.37 \pm 0.95) \times 10^{-6}$ for the 7.95 MHz resonator, $C_l = (4.30 \pm 0.45) \times 10^{-6}$

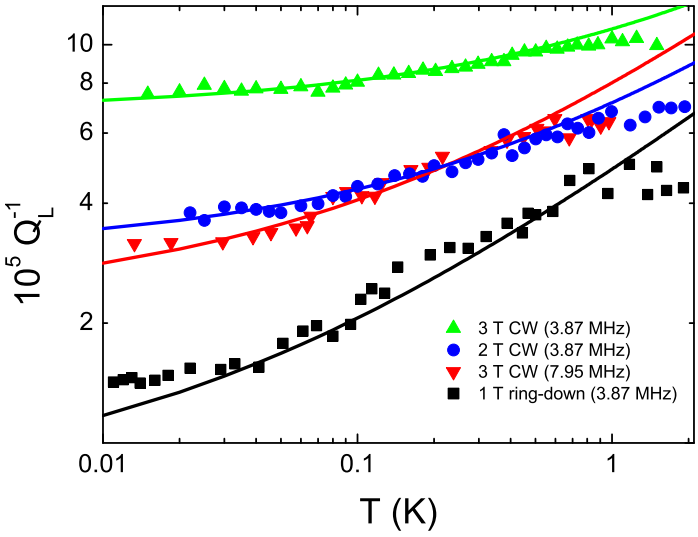

Figure 4.5: Q_L^{-1} as a function of temperature for both resonators plotted on a log-log scale. The solid curves represent the expression $bT^{0.5} + \alpha B^2$. The parameter b was extracted from Figure 4.4.

at 3 T and $C_l = (8.48 \pm 0.30) \times 10^{-6}$ at 2 T for the 3.87 MHz resonator.

The frequency shift for the 3.87 MHz device stops increasing at about 400 mK and shows a systematic decrease above 600 mK. At higher temperatures, no frequency decrease is seen for the 7.95 MHz device, though it has to be noted that the scatter in the data around 1 K, and the lack of data above, makes it difficult to draw firm conclusions about the underlying behaviour at higher temperatures for this device. The data for this particular sample were collected in two runs and a frequency jump of 20.4 kHz that occurred during thermal cycling between the runs was subtracted from the low temperature data. Nonetheless, thermal cycling caused no change in the temperature dependence of $\frac{\Delta f}{f_0}$. Some saturation is also observed in the frequency shift data, indicated by the two points (denoted by unfilled circles) below 30 mK in Figure 4.6(a). This suggests that thermal decoupling between the samples and the refrigerator could be a likely explanation for the saturation observed in both the resonant frequency and dissipation at the lowest temperatures.

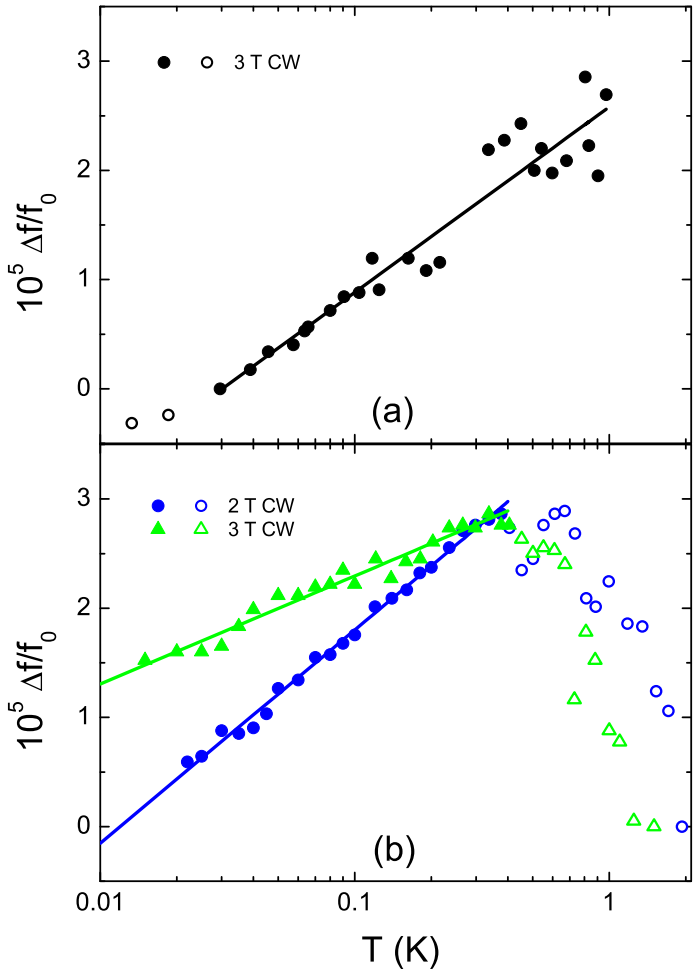

Figure 4.6: $\frac{\Delta f}{f_0}$, as a function of temperature for (a) 7.95 MHz resonator and (b) 3.87 MHz resonator. The smooth lines are logarithmic fits to the subset of data points marked with full circles/triangles.

4.4 Discussion

This section is split into two parts, the first part provides a qualitative description of the data using the standard tunnelling model as a framework. The second part discusses some recent experiments on metallic nanomechanical structures at low temperatures which were reported after the work presented in this chapter was published. Similarities and differences between the studies are discussed.

4.4.1 Qualitative description of data

The strong variation seen in the dissipation at such low temperatures suggests that tunnelling TLS, which are known to exist in polycrystalline metals [69], are the dominant source of dissipation. The STM assumes tunnelling TLS with a broad distribution of energies and relaxation rates. In the regime relevant to the measurements described here, where $\hbar\omega \ll k_B T$, the dominant contribution to the dissipation comes from the relaxation of the TLS rather than resonant interaction. A change in the behaviour is expected at a temperature T^* where the minimum relaxation time for the TLS matches the period of the resonator. Above T^*, there is a plateau where the dissipation $Q_p^{-1} = \frac{\pi}{2}C$, depends on the material properties such as the spectral density of TLS but is independent of temperature and frequency. Below T^* the dissipation is expected to have a characteristic power-law dependence on temperature that depends both on how the TLS relax and the form of the underlying distribution [33, 36].

The dissipation seen in the gold resonators fits the pattern predicted by the STM with both devices showing plateau-like features above about 600 mK and a power law dependence $\sim T^{0.5}$ at lower temperatures down to about 30 mK. However, the temperature dependence observed here is much lower than both those predicted by the standard theories of acoustic damping in bulk solids [33, 36]. Interestingly, a recent model of damping due to TLS in a nanomechanical resonator predicted a $T^{0.5}$ behaviour when the relaxation of the TLS is due to phonons in the structure [70]. However, this model assumes a dielectric rather than a metallic resonator and no plateau region is predicted. Furthermore, the dissipation in the plateau regions is very similar for the two devices although it leads to a value $C \sim 2.5 \times 10^{-5}$ which is about an order of magnitude below the range typical for amorphous

solids [39], though similarly low values are seen in some disordered metals [37] as well as in stressed dielectric resonators [71].

The STM also predicts a frequency that increases logarithmically with temperature for $T < T^*$ due to the resonant interaction between the TLS and the acoustic excitation, with a gradient given by C [33, 36]. For $T > T^*$, a logarithmic decrease in the frequency is expected, with a gradient that depends on the dominant relaxation mechanism. Although a logarithmic increase in frequency at low temperatures is seen, the gradients are only about a third of the value of C inferred from the dissipation in the plateau regions. The logarithmic decrease in the frequency shift that is seen above 600 mK for the 3.87 MHz device agrees qualitatively with the STM however the value of C inferred from the frequency shift data depends on the magnetic field for unknown reasons. For the higher frequency resonator, the scatter and the lack of data above 1 K make it difficult to draw any firm conclusions.

4.4.2 Recent studies on metallic structures

The work described in this thesis is the first systematic study of low temperature dissipation in unsupported metallic nanomechanical resonators. However, very recently other groups have begun to study metallic resonators as well. In a recent publication [72], Hoehne et al, reported low temperature measurements on aluminium nanomechanical beams with frequencies in the range 40 - 360 MHz. The authors measured the 'in-plane' response of four doubly-clamped aluminium nanomechanical resonators using the magnetomotive technique and looked at the temperature dependence of the damping and frequency shift. As shown in Figure 4.7, the frequency shift in all four resonators shows the same qualitative temperature dependence with a peak at around 1.5 K with a decrease at higher and lower temperatures. The logarithmic fits to the low temperature data yield values of C in the range $10^{-4} - 10^{-5}$, an order of magnitude higher than for the gold resonators, and closer to value of C for bulk amorphous materials, $C \sim 10^{-3} - 10^{-4}$ which is known to be almost universal.

The damping in the resonators increases linearly with temperature up to about 1 K and above this temperature it continues to increase but with a smaller slope; this is shown in Figure 4.8. The dissipation has a finite value at $T = 0$ for all resonators and the authors claim it is clamping loss

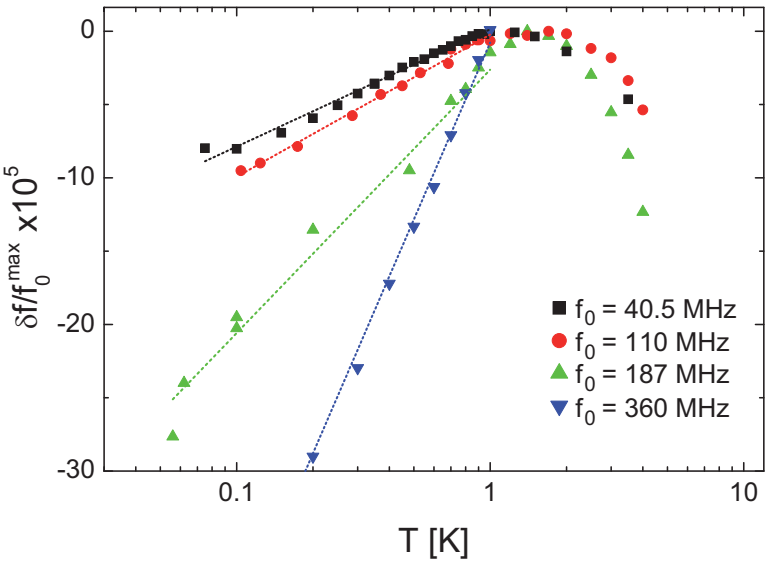

Figure 4.7: Relative shift of the resonant frequency as a function of temperature for different aluminium resonators. For each device the frequency shift is normalized to the maximum resonant frequency f_0^{max}. The dotted lines are logarithmic fits to the data used to determine values of C [72].

because of its frequency dependence. The linear dependence of dissipation on temperature indicates electron-dominated relaxation of TLS according to the STM. However electron relaxation times are extremely short and so this mechanism would only be observed at the lowest temperatures, below 100 mK. The authors argue that at temperatures below 1 K, the beams are essentially 1-D structures as the dominant phonon wavelength in aluminium at these temperatures is comparable to the device dimensions ($\lambda \geq 100$ nm). The linear temperature dependence of the damping is consistent with a 1D phonon-dominated relaxation mechanism. The authors suggest dislocation kinks within the aluminium structure, which are known to exist in crystals, as possible candidates for TLS.

Another recent experiment on an aluminium nanomechanical resonator [73] carried out by a research group from Finland confirmed the linear temperature dependence of dissipation up to 1 K in these structures. The response of the beams was measured capacitively, between 100 K and 10 mK, with the aluminium becoming superconducting at the lowest temperatures. These experiments further support the 1-D phonon modes idea and reject the electron-dominated relaxation theory as superconducting aluminium has no unpaired electrons.

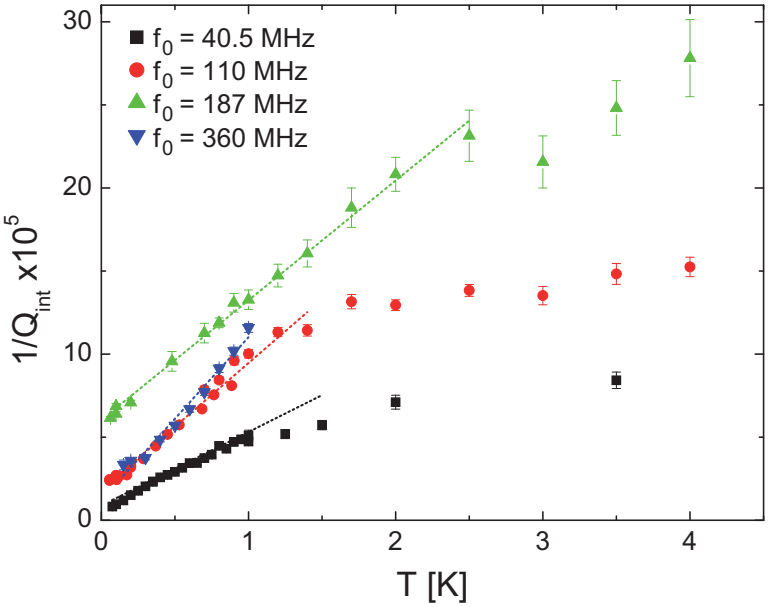

Figure 4.8: Damping, Q_0^{-1}, as a function of temperature for four resonators of different lengths. Damping increases linearly up to 0.7 - 1.5 K followed by a weaker temperature dependence above this temperature. The dotted lines are fits to the data [72].

Measurements on micron-thick aluminium films were carried out by Parpia's group at Cornell University [74]. The authors measured the elastic properties of the films via the double paddle oscillator technique [44]. Measurements at temperatures between 10 mK and 1 K revealed good agreement between the data and the STM for the case of phonon-dominated relaxation mechanism. The plateau in the dissipation is within the glassy range $2 \times 10^{-4} < Q^{-1} < 2 \times 10^{-3}$ with a value of $C \sim 1.3 \times 10^{-4}$, similar to that for aluminium nanomechanical resonators. The crossover temperature T^* for these devices is just 100 mK which is consistent with the STM since T^* varies as $\omega^{1/3}$ and the frequency of these resonators is only 5.5 KHz. They also argue that the origin of TLS in their bulk samples is dislocation kinks.

The disagreement between the low temperature behaviour of gold and aluminium suggest that dimensionality has an important role to play in determining the sources of dissipation in such structures. For a beam to be classified as a 1D structure, the phonon wavelength must be of the same order as the beam dimensions or longer. The gold resonators reported in this thesis have similar dimensions to the aluminium resonators however, they are on average, twice as wide therefore the gold resonators cannot be

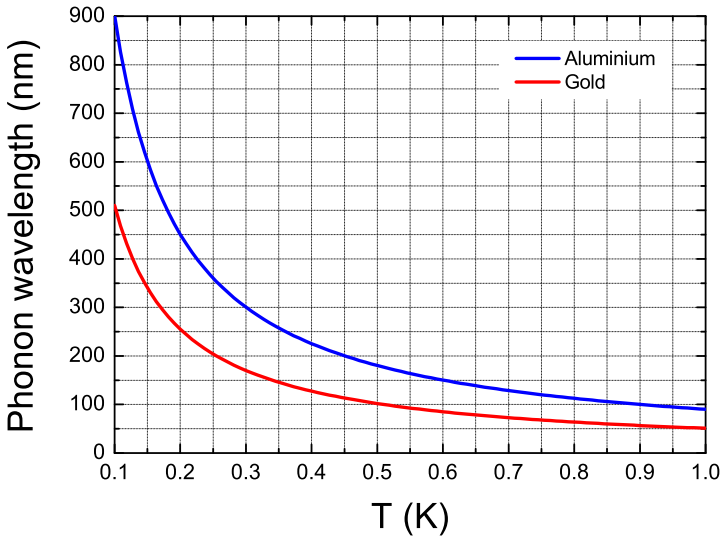

Figure 4.9: Primary phonon wavelength in aluminium and gold at temperatures below 1 K.

assumed as 1-D structures. Figure 4.9 shows the variation in the phonon wavelengths in both aluminium and gold for temperatures below 1 K. The wavelengths were calculated using the equation

$$\lambda_T = \frac{hv}{2.821 k_B T}, \tag{4.1}$$

where h is Planck's constant and v the speed of sound in the solid [1]. The speed of sound in the respective metals was estimated using the simple expression $v = \sqrt{\frac{K}{\rho}}$, where K is the bulk modulus of the solid and ρ its density. It can be noticed that from a phonon point of view, the aluminium beams start to look like 1D structures at temperatures around 500 mK; for the gold beams this is the case only at temperatures below 200 mK. However, our measurements do not support the 1D picture as even below 200 mK there is no sign of a linear dependence of Q_0^{-1} on temperature (see Figure 4.4).

Apart from dimensionality, another factor which could add to the discrepancies is the formation of thin oxide layers (1 - 2 nm) on aluminium, which will also have TLS contributing to the dissipative behaviour of the whole device. Oxide layers do not form on top of gold.

4.5 Summary and Conclusions

The dissipation at low temperatures in gold nanomechanical resonators follows a weak power-law dependence $Q_0^{-1} \propto T^{0.5}$ over the range 30 - 500 mK and above 600 mK the dissipation saturates. The relative shift in frequency of the resonators shows a logarithmic increase up to about 400 mK. The observation of features normally associated with tunnelling TLS, such as plateau in the dissipation and a power-law behaviour at low temperatures together with the logarithmic change in frequency, suggest that this is the right paradigm in this case. Nevertheless, our results do not fit quantitatively with current theories. However, differences between our results and theories based on the behaviour of bulk amorphous solids are to be expected, not just because the TLS relaxation rates should be rather different in nanomechanical resonators [70] but also because the very small volume of the samples [75] together with the effects of tension [71] may lead to a distribution of TLS quite different to that usually assumed for bulk disordered solids. Furthermore, recent experiments on aluminium nanomechanical resonators suggest that dimensionality has a key role to play in the dissipation in such devices as in the case of aluminium resonators, TLS relaxation is dominated by 1-D phonon modes at temperatures below 1 K.

Further experiments on gold devices are required in order to get a full picture of the dissipation mechanisms in such devices; a more systematic study, including different fabrication processes, and surface passivation of the beams with thiol molecules [76] might help clarify the nature of TLS in such materials. Gold beams with smaller cross-sections would allow to explore the effect dimensionality on dissipation and check whether the 1D phonon model would also apply for gold devices.

Chapter 5

Dissipation in silicon nitride nanomechanical beams at millikelvin temperatures

In this chapter we describe the results from a study of dissipation and frequency shift in gold-coated, high-stress silicon nitride nanomechanical resonators. The measurements were carried out in the temperature range 40 mK to 1.5 K and the magnetomotive transduction scheme was used to drive and detect the motion of the beams. High-stress silicon nitride has been used to fabricate nanomechanical resonators for a number of NEMS experiments reported recently [9, 77, 78] as the Q-factor of such resonators has been found to be extremely large [57, 79]. The temperature dependence of the dissipation at low temperatures in other dielectric nanomechanical resonators have been reported in the recent years [45–47]. However, the low temperature dissipation in silicon nitride resonators has not been studied systematically. The presence of a metallic layer on top of the dielectric resonator makes the interpretation of the results more challenging as it is well known that the metallic layer contributes significantly to the dissipation in the system [44].

The fabrication of the devices along with the experimental arrangement for these measurements have already been explained in Chapter 3. We carried out measurements on two batches of samples, the first with a 80 nm gold layer and second with a 40 nm one. The first batch had 4 beams of lengths 4.4, 6.4, 15.8 and 25.5 μm and the motion of these devices was mea-

sured using the balanced bridge technique. Unfortunately, the coaxial line connected to the 15.8 μm long beam was attenuating much more than expected (by about 40 dB), most likely due to a lose connection, thus it was not possible to measure this particular beam. From the second batch, with a thinner gold, we were only able to detect the signal from the 25.5 μm long beam which was therefore measured in transmission mode (see section 3.4 in Chapter 3 for more details on transmission measurements). We were able to measure several higher modes of the 25.5 μm long beams. The results showing the magnetic field and temperature dependence of the dissipation and resonant frequencies are divided into two sections, corresponding to the two batches of samples. The results are qualitatively analyzed in the framework of the STM and compared to other recent low temperature studies on high-stress silicon nitride oscillators.

5.1 Device frequencies

The first batch of resonators had a width of 190 nm and a thickness of 170 nm (excluding the gold layer) and the thin gold device had a width and a thickness of 170 nm. The silicon nitride layer has a built in tensile stress of about 1070 MPa, measured at room temperature [52]. When cooled down to low temperatures, the difference in the thermal contraction between the silicon nitride and silicon causes an additional compressive stress in the silicon nitride layer, which at 1 K, is found to be about -50 MPa, estimated using the equations

$$\epsilon_{SiN} = (\alpha_{T_{SiN}} - \alpha_{T_{Si}})\Delta T \tag{5.1}$$

$$\sigma_{SiN} = \left(\frac{E_{SiN}}{1-\nu}\right)\epsilon_{SiN}, \tag{5.2}$$

where ϵ_{SiN} is the thermal strain of silicon nitride, α_T is the coefficient of thermal expansion, σ_{SiN} is the compressive stress in silicon nitride from the cooling effect and ν is Poisson's ratio [80]. Values of 2.8×10^{-6} and 2.0×10^{-6} for α_{TSi} and α_{TSiN} were used, along with $E_{SiN} = 211$ GPa and $\nu \sim 0.3$ [80]. This leads to an effective tensile stress of 1020 MPa at low temperatures.

We measured the flexural vibrations of the beams in the plane of the substrate, or in other words, the vibrations along the width of the beams. The frequencies were estimated using several methods: using equation 2.26 (see Chapter 2), through graphical solutions (in Matlab) looking for the zero

crossings of the function[1]

$$Y = \Omega + U\sin(k_2)\sinh(k_1) - \Omega\cos(k_2)\cosh(k_1) \tag{5.3}$$

an example of which is shown in Figure 5.1(a), and also from finite element methods (COMSOL multiphysics modelling package) as shown in Figure 5.1(b). The tensile stress in the gold layer from the cooling effect is estimated to be around 200 MPa, five times smaller than in silicon nitride. The cross-section of the gold layer is, at most, half that of the silicon nitride, which leads to the tension in the gold being roughly an order of magnitude lower than in silicon nitride[2]. The Young's modulus of gold (78 GPa) is also much lower. Therefore, for the frequency calculations, we only account for the effect of the gold electrode in the total mass of the resonator, $m = m_{SiN} + m_{Au}$ and neglect the effects on the overall tension or Young's modulus. Table 5.1 shows the frequency estimates, obtained from the different methods, for the resonators (and modes) investigated along with the measured resonant frequencies. The estimates are in fairly good agreement with each other and are within about 10% of the measured frequencies.

Table 5.1: Estimated and measured resonant frequencies (in MHz) of the nanomechanical beams used for the studies described in this chapter. Parameters used: $E_{SiN} = 211$ GPa, $\rho_{SiN} = 2700$ kgm^{-3}, $\rho_{Au} = 19300$ kgm^{-3}, $\sigma_{SiN} = 1020$ MPa. The symbol n represents the mode number.

Length μm	**n**	**Eq. 2.25 (MHz)**	**Matlab (MHz)**	**COMSOL (MHz)**	**Measured (MHz)**
Gold thickness $\sim$ 80 nm					
4.4	1	56.28	56.50	58.44	55.88
6.4	1	32.40	32.34	33.22	31.36
25.5	1	6.52	6.18	6.23	5.45
25.5	3	18.71	19.22	19.43	16.84
Gold thickness $\sim$ 40 nm					
25.5	1	8.28	7.82	7.87	7.50
25.5	3	23.54	24.16	24.38	22.85
25.5	5	41.35	42.48	43.02	39.28

[1] Equation 2.25 in Chapter 2

[2] Recall that $T_0 = \sigma A$ where T_0 is the tension, σ the stress and A is the cross-sectional area (see Chapter 4)

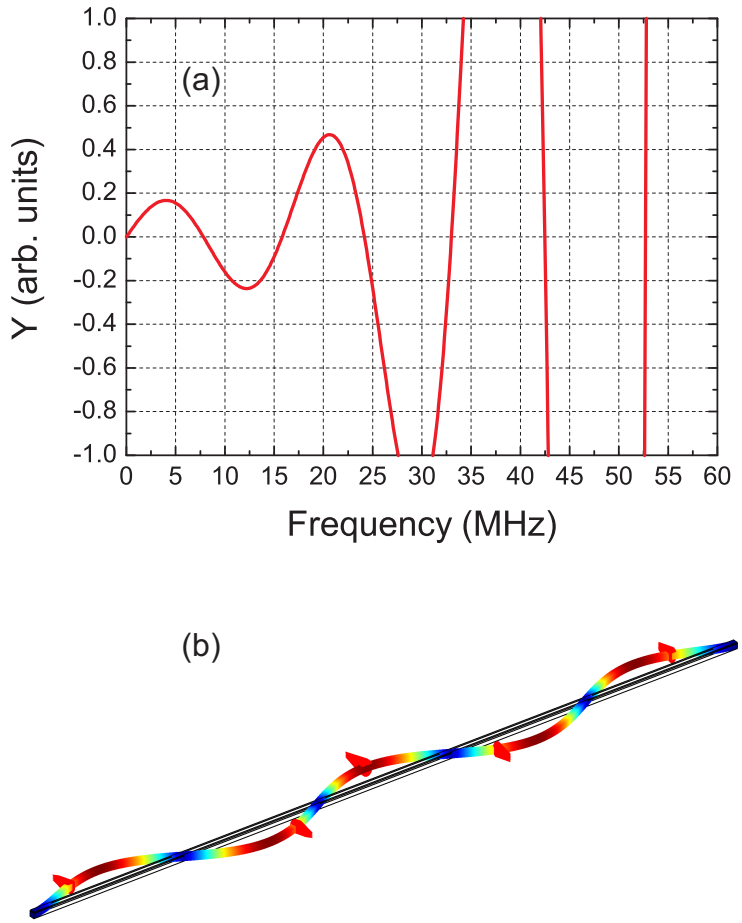

Figure 5.1: (a) Plot of the function $Y = \Omega + U\sin(k_2)\sinh(k_1) - \Omega_n\cos(k_2)\cosh(k_1)$, with the zero crossings giving the mode frequencies for the 25.5 μm long beam with a thin gold layer, (b) COMSOL simulation showing the shape of the 5th mode of the same sample.

5.2 Si_3N_4 beams with a thick gold electrode

In this section we present the results from the low temperature studies on the silicon nitride nanomechanical resonators with the thicker (80 nm) gold electrode. A total of four resonances were measured, three of them corresponding to the fundamental modes of the doubly-clamped beams plus the third flexural mode of the longest beam. All measurements were made using the CW technique (described in Chapter 3) at several temperatures between 40 mK and 1.5 K, using two different magnetic fields at each temperature: 2 and 4 T. A careful magnetic field dependence study was also undertaken at $T = 80$ and 500 mK. Care was taken to ensure that the resonators were not driven into the nonlinear regime.

5.2.1 Magnetic field dependence

Figures 5.2 and 5.3 show the field dependence of the dissipation and resonant frequency for the samples measured. The signal from the 55.88 MHz beam was very hard to detect and a field dependence study for this resonator was only performed at 500 mK. As expected, the dissipation varies linearly with magnetic field squared. The slope of the linear fits (denoted by the red lines) is $\alpha = \frac{\xi L^2}{m\omega_0}\frac{R_{ext}}{|Z_{ext}|^2}$. The fits yield the following values of α (averaged from both temperatures): $(1.39 \pm 0.02) \times 10^{-5}$ T^{-2} (5.45 MHz), $(5.93 \pm 0.45) \times 10^{-7}$ T^{-2} (16.84 MHz), $(8.29 \pm 0.70) \times 10^{-7}$ T^{-2} (31.36 MHz) and $(2.82 \pm 1.44) \times 10^{-7}$ T^{-2} (55.88 MHz). At all other temperatures the nanomechanical resonators were measured at two fields, and it was found that α had no systematic dependence on temperature.

The resonant frequencies of the first and third flexural modes of the 25.5 μm long beam decrease with increasing magnetic field (shown in the insets of Figure 5.2), which indicates that the impedances of the external circuitry are not completely real, but have some reactance too. The slope of the linear fits is $\beta = \frac{\xi L^2 f_0}{2\pi m}\frac{X_{ext}}{|Z_{ext}|^2}$ and the intercept is f_0^2. Knowing β, we can infer the intrinsic resonant frequency of the beam at any temperature. However, by taking the ratio $\frac{\alpha}{\beta}$, we estimated that the reactance (X_{ext}) of the measurement circuit is at most, only $\frac{R_{ext}}{5}$. No systematic frequency shift with field was seen for the two shorter beams (Figure 5.3 insets) .

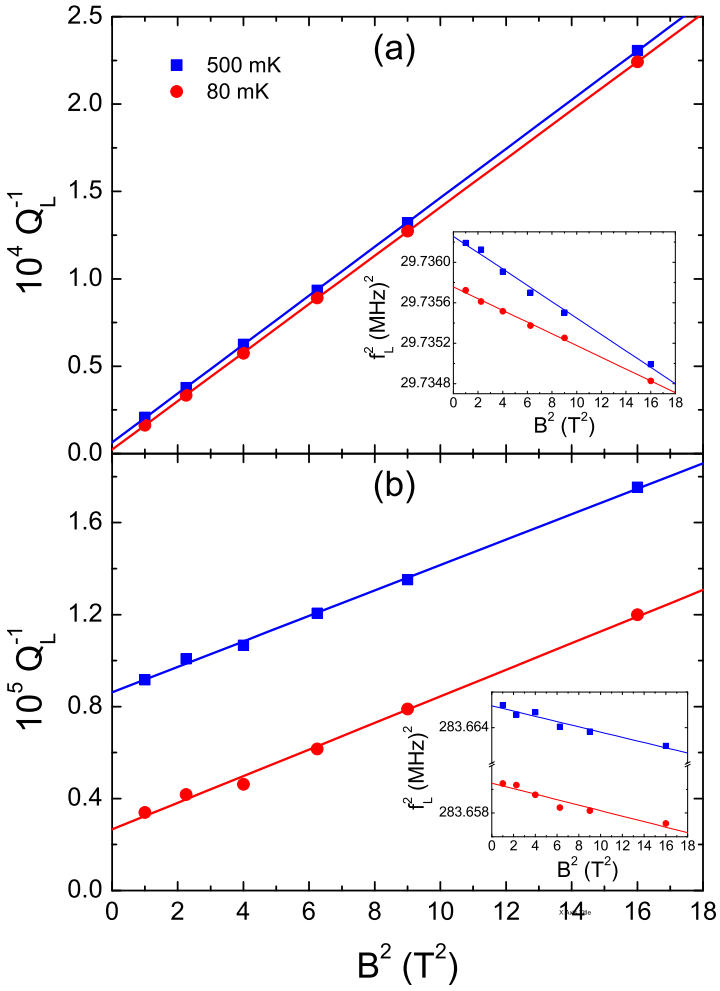

Figure 5.2: Dissipation, Q_L^{-1}, versus B^2 for the (a) first mode (5.45 MHz) and (b) third mode (16.84 MHz) resonance of the 25.5 μm long beam. The straight lines are linear fits to the data from which α was extracted. The insets show the change in resonant frequency of the beams with the magnetic field.

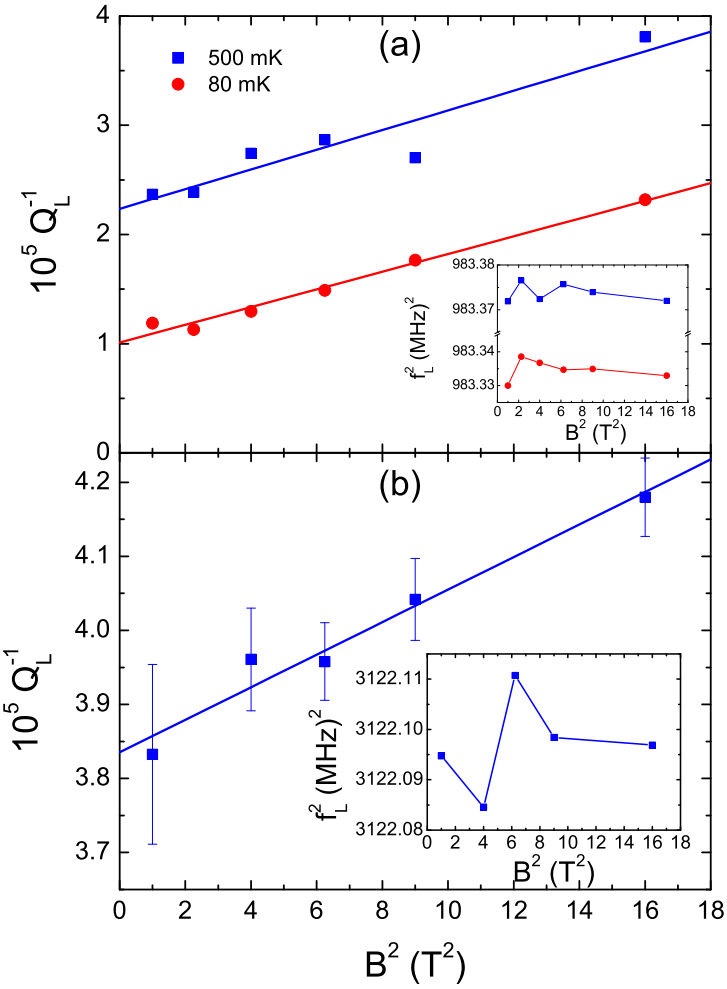

Figure 5.3: Dissipation, Q_L^{-1}, versus B^2 for the (a) 31.36 MHz and (b) 55.88 MHz resonator. The straight lines are linear fits to the data from which α was extracted. The insets show the change in resonant frequency of the beams with the magnetic field.

5.2.2 Dissipation as a function of temperature

Figures 5.4(a) and (b) show the temperature dependence of the intrinsic dissipation, Q_0^{-1}, for the devices measured. The data corresponding to the different resonators follow a common pattern and two different regions of interest can be identified. Above about 800 mK, the dissipation seems to increase very slowly for the 5.45, 16.84 and 55.88 MHz samples, but a complete saturation is not observed. On the other hand, the dissipation in the 31.36 MHz resonator increases faster above 800 mK, for reasons which are not clearly understood. Nevertheless, because the signals from the two short beams were very small and hard to detect, higher drives were used with increasing temperature and it is possible that the 31.36 MHz resonator might have been driven on the verge of nonlinearity, causing the observed behaviour.

From 800 mK down to base temperature ($\sim$ 40 mK), the dissipation in all devices falls linearly with temperature as denoted by the linear fits (smooth lines) to data according to the equation $Q_0^{-1} = bT + Q_0^{-1}(0)$. Here, b is a constant related to the coupling strength between the TLS and electrons/phonons in the system and $Q_0^{-1}(0)$ indicates the presence of a temperature independent dissipation mechanism. Table 5.2 summarizes the fit parameters.

Table 5.2: Values obtained from the linear fits to the dissipation data, the parameter b related to the coupling strength between TLS and electrons/phonons in the system and the temperature independent dissipation $Q_0^{-1}(0)$.

f_0 (MHz)	b ($\times 10^{-5}$)	$Q_0^{-1}(0)$ ($\times 10^{-6}$)
5.45	0.98	0.78
16.84	1.15	1.70
31.36	2.02	7.24
55.88	4.04	14.90

5.2.3 Resonant frequency as a function of temperature

The relative shift in the frequency of the resonators (measured at 2 T) as a function of temperature is shown in Figure 5.5. For all the samples, there is an increase in the resonant frequency with temperature. However, in

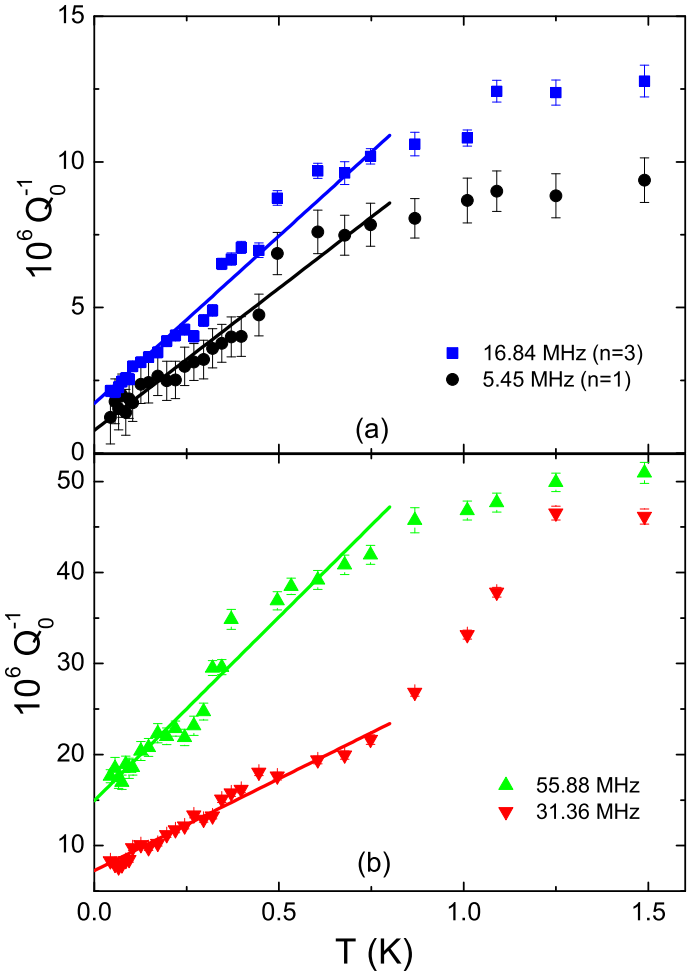

Figure 5.4: Q_0^{-1} as a function of temperature is shown for the (a) first (•) and third (■) mode of the 25.5 μm long beam and (b) 6.4 (▼) and 4.4 (▲) μm long beams. The straight lines are linear fits to the data up to $T = 800$ mK.

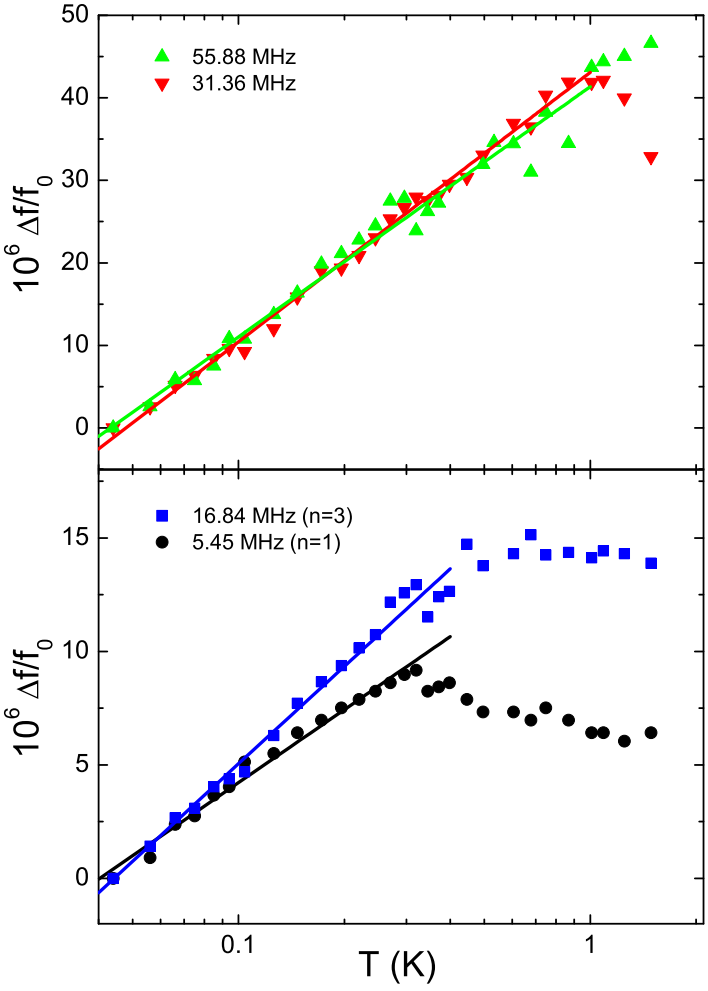

Figure 5.5: $\frac{\Delta f}{f_0}$ as a function of temperature for the four resonances measured. The smooth lines are logarithmic fits to the data up to $T \sim 400$ mK for the low frequency resonances, and up to $T \sim 1$ K for the high frequency resonators.

the case of the longer beam, the frequency of both its first and third mode increase up to about 400 mK whereas the frequencies of the two short beams increase over the whole temperature range measured. The frequency increase is a behaviour well described by the logarithmic expression $\frac{\Delta f}{f_0} = C\ln\frac{T}{T_0}$, a prediction of the STM, already introduced in Chapter 2. The values of C extracted from the fits to the data (denoted by the smooth lines in Figure 5.5) are given in Table 5.3.

Table 5.3: C values extracted from logarithmic fits to the frequency shift versus temperature data.

f_0 (MHz)	C ($\times 10^{-5}$)
5.45	0.46 ± 0.03
16.84	0.62 ± 0.03
31.36	1.42 ± 0.05
55.88	1.32 ± 0.08

At the higher temperatures, the frequency of the first mode of the longest beam starts to decrease slowly whereas the third mode frequency seems to saturate. The discrepancies in the frequency behaviour between the different devices and the lack of data above 1.5 K makes it difficult to draw any firm conclusions about the underlying behaviour at the higher temperatures. Furthermore, no frequency saturation is observed in the data at the lowest temperatures as was the case for the gold resonators (Chapter 4).

The signal for the 55.88 MHz resonator was very noisy and it was very challenging to measure its resonance characteristics. Small frequency jumps, of the order of a few Hertz, between the temperatures measured made it difficult to extract the true C value for this resonator. This unpredictable behaviour is illustrated by the scatter in the frequency shift data for this particular resonator.

5.3 Si_3N_4 beams with a thin gold electrode

The second batch of samples had the same number of resonators (with the same lengths) as the first batch, but with a thinner (40 nm) gold layer. For some unknown reason, we were only able to detect a signal from the the 25.5 μm long beam and not the others. Nonetheless, we were successful in

measuring the third and fifth mode of this resonator as well as the fundamental. Measurements were carried out in transmission mode, measuring a dip in the conductance of the beam.

5.3.1 Magnetic field dependence

In contrast to the thick gold resonators, the thin gold beam was only measured once at any given temperature, at a fixed field, instead of being measured at two different fields. A careful magnetic field dependence study was carried out at three temperatures: 45, 100 and 500 mK (only at 500 mK for mode 5). The average value of α extracted from the fits to the Q_L^{-1} vs B^2 data was then used to extrapolate to Q_0^{-1} at any arbitrary temperature. We assumed that the change in α with temperature is minimal, if not negligible, based on the behaviour measured at 45, 100 and 800 mK.

Figures 5.6(a), (b) and (c) show the plots of the loaded dissipation as a function of B^2 for modes 1, 2 and 3, respectively. As expected, the dissipation in all three modes varies linearly with B^2, with α being: $(1.226 \pm 0.021) \times 10^{-5}$ T^{-2} (7.5 MHz), $(5.312 \pm 0.241) \times 10^{-7}$ T^{-2} (22.85 MHz) and $(1.309 \pm 0.101) \times 10^{-7}$ T^{-2} (39.28 MHz). The effect of the magnetic field on the resonator decreases for higher modes. Similar to the thicker gold devices, a systematic decrease in the resonant frequency is seen with increasing magnetic field, once again confirming that the coaxial cables have a reactive component. However, this reactive component is estimated to be small compared to the resistive part and the shifts in resonant frequency with magnetic field are only of the order of a few Hertz.

5.3.2 Dissipation as a function of temperature

Figure 5.7 shows the intrinsic dissipation plotted against temperature for the three flexural modes measured. The dissipation in all modes exhibits a linear behaviour in the temperature range measured, no saturation is observed at high or low temperatures. The smooth lines are linear fits to the data from which we extract b and Q_0^{-1}, shown in Table 5.4.

The large error bars in Figure 5.7 are due to the fact that the Q-factor of the resonator is extremely high (exceeding $Q_0 \sim 10^6$ for mode 1). The magnetic fields at which the resonator was measured were above 1 T, leading to large errors in the extrapolation to Q_0^{-1}. There was a difference of about

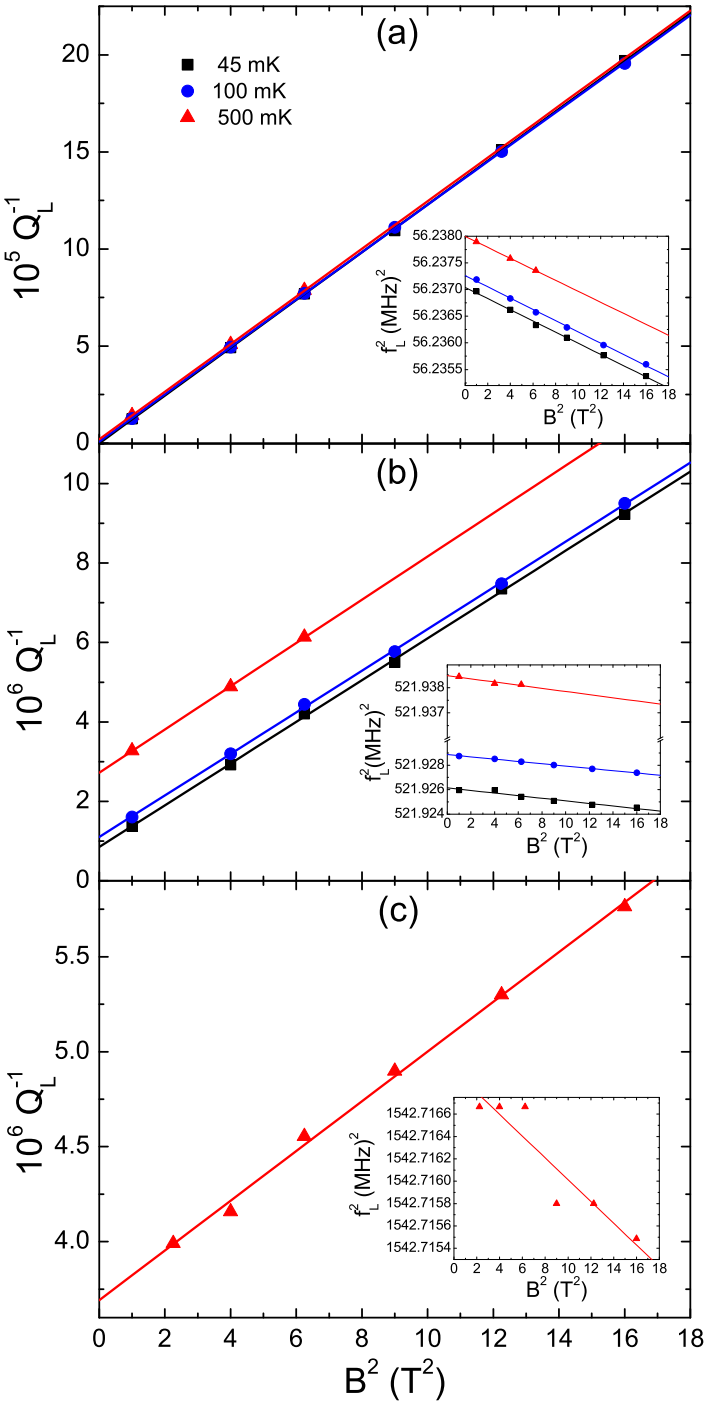

Figure 5.6: Dissipation, Q_L^{-1}, versus B^2 for the (a) first, (b) third and (c) fifth mode of the 25.5 μm long beam. Insets show the resonant frequency of the beams versus B^2.

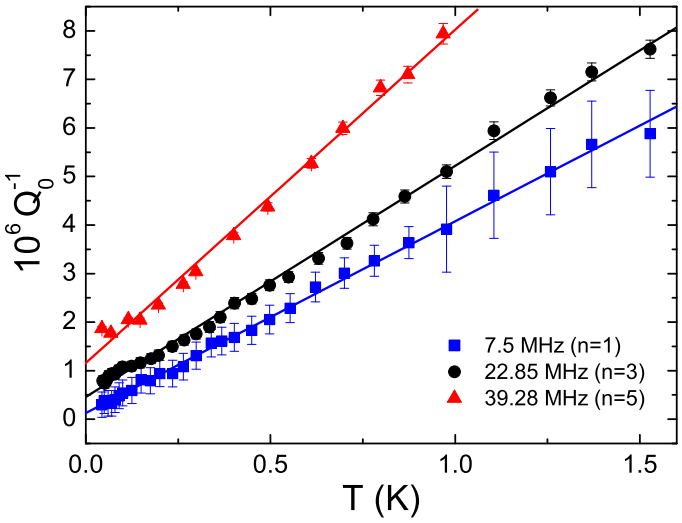

Figure 5.7: Q_0^{-1} as a function of temperature for the (a) first , third and fifth mode of the 25.5 μm long beam with a thin gold electrode. The straight lines are linear fits to the data.

2 orders of magnitude between the measured Q-factor and the intrinsic Q-factor ($Q_L \sim 10^4$ and $Q_0 > 10^6$ for the fundamental mode). For example, at 40 mK, the lower bound for the Q-factor of the fundamental mode is about 4×10^6, however it could be as high as $\sim 30 \times 10^6$. This problem could have been solved by measuring at lower magnetic fields, below 1 T. Note that the extrapolation error is only significant when the Q-factor of a resonator is very large, for smaller Q-factors, measuring at a field above 1 T is reasonable.

Table 5.4: Values obtained from the linear fits to the dissipation data shown in Figure 5.7.

f_0 (MHz)	b ($\times 10^{-6}$)	$Q_0^{-1}(0)$ ($\times 10^{-7}$)
7.50	3.95 $\pm$ 0.04	1.29 $\pm$ 0.25
22.85	4.76 $\pm$ 0.05	4.61 $\pm$ 0.32
39.28	6.87 $\pm$ 0.16	11.56 $\pm$ 0.86

5.3.3 Resonant frequency as a function of temperature

The temperature dependence of the frequency of the three flexural modes is shown in Figure 5.8. The resonant behaviour of the different modes were measured at 1, 2 and 3 T respectively. The signal measured scales inversely with mode number, hence higher magnetic fields were employed for the higher modes. As in the case for the thicker gold devices, an increase in the resonant frequency with temperature is observed, however there is one very important difference: the frequency increases all the way up to 1 K for all three modes in this case. Above 1 K, saturation is observed. The smooth lines are fits to the data from which we extracted the values of C, shown in Table 5.5. Saturation is observed at the lowest temperatures although the lack of data below 40 mK makes it difficult to establish its origin.

Table 5.5: C values extracted from logarithmic fits to the frequency shift versus temperature data for the three flexural modes measured.

f_0 (MHz)	C ($\times 10^{-5}$)
7.50	0.39 ± 0.01
22.85	0.55 ± 0.02
39.28	0.95 ± 0.07

5.4 Discussion

This section is split into three parts: the first provides a qualitative description of the data using the STM as a framework. In the second part we focus on the contributions of the metallic layer on the overall dissipation and the third part discusses some other recent experiments on high stress silicon nitride resonators at low temperatures.

5.4.1 Qualitative description of data

The strong variation seen in dissipation and the logarithmic increase in resonant frequency observed at very low temperatures suggest that tunnelling TLS, are the dominant source of dissipation. The experiments were carried out in the regime where $\hbar\omega \ll k_b T$, and the dominant contribution to the dissipation comes from the relaxation of the TLS rather than resonant in-

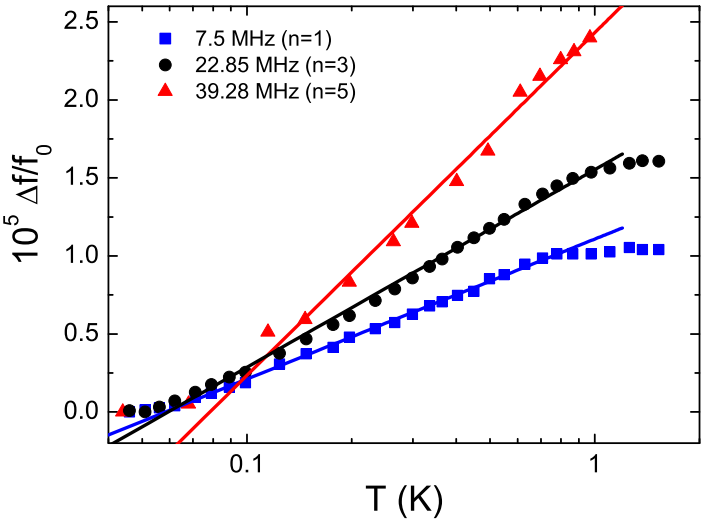

Figure 5.8: $\frac{\Delta f}{f_0}$ as a function of temperature for mode 1 measured at 1 T, mode 3 measured at 2 T and mode 5 measured at 3 T. The smooth lines are logarithmic fits to the data up to $T \sim 1$ K.

teraction. A plateau is not quite observed for any of the devices, but the dissipation in the thick gold electrode devices starts to saturate at the higher temperatures. However, the lack of data above 1.5 K makes it difficult to draw any firm conclusions.

Quantitatively, the linear temperature dependence of dissipation cannot be explained by the basic version of the STM [33, 36]. Although, at first instance, the linear behaviour can be attributed to TLS-electron interaction in the gold layer, measurements on bare gold nanomechanical resonators of similar frequencies (see Chapter 4) revealed a $T^{0.5}$ dependence, in disagreement with the results presented here. Furthermore, a temperature independent dissipation mechanism, indicated by $Q_0^{-1}(0)$, is also likely to play a key role. The value of $Q_0^{-1}(0)$ scales inversely with the length of the resonator (see Figure 5.9), therefore this dissipation mechanism is most likely to be clamping loss [26], however, the lack of a suitable theory on clamping losses in high-stress nanomechanical resonators makes it difficult to do any further analysis. $Q_0^{-1}(0)$ also becomes larger with mode number, which can be qualitatively explained in terms of the bending of the particular flexural mode. The bending points in the beam increase with mode number, hence

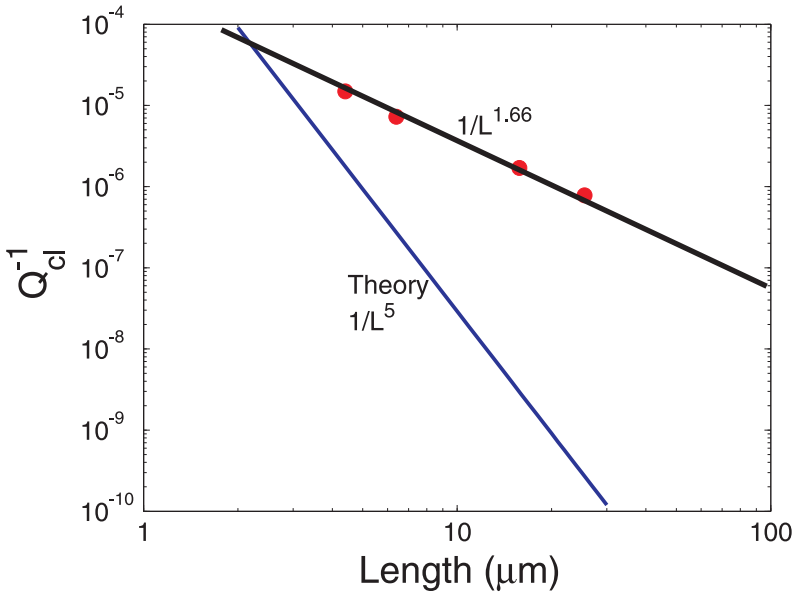

Figure 5.9: $Q_0^{-1}(0)$ (denoted by the filled circles) versus length for the thicker gold resonators, showing the difference between the clamping loss theory ($\frac{1}{L^5}$) described in reference [26] and the experimental behaviour ($\frac{1}{L^{1.66}}$).

a higher flexural mode is expected to lose more energy than a lower mode [81].

The STM also predicts a shift in frequency of the oscillator that increases logarithmically with temperature $T < T^*$ due to the resonant interaction between the TLS and the acoustic excitation, with a gradient given by C [33, 36]. For $T > T^*$, a logarithmic decrease in frequency is expected, with a gradient that depends on the dominant relaxation mechanism. We observe a logarithmic increase in frequency at the lowest temperatures for all the devices, with $C \sim 10^{-5} - 10^{-6}$, an order of magnitude below the range typical for amorphous solids [39], though similarly low values are seen in some disordered metals [37] as well as in stressed silicon nitride micromechanical resonators [71] and in polycrystalline gold resonators (Chapter 4). Furthermore, the frequency dependence of C is not well understood, and it cannot be explained in the framework of the STM.

5.4.2 Effect of metallic layer

The presence of a gold electrode on the silicon nitride resonators makes the interpretation of the results very challenging, specially as we have no data for a bare silicon nitride resonator (without any metal on top). Nevertheless, we measured two nanomechanical beams of very similar dimensions (25.5 μm long) but with two different gold thicknesses, which can be compared to understand the effect of the gold layer, at least to a qualitative level.

The first aspect to notice is that the gold electrode severely diminishes the resonant frequency and Q-factor of the resonators due to its heaviness; the thicker the gold, the lower the Q-factor and f_0. At base temperature (40 mK), the Q-factor of the 5.45 MHz beam is about 1×10^6 whereas for the 7.5 MHz beam it is about 4×10^6 (note that these are only lower bounds). However, the most important feature to notice is that the temperature dependence of both the dissipation and frequency differ for the two thicknesses of gold. For the 5.45 MHz resonator, the dissipation only increases linearly up to 800 mK, with the frequency saturating at 400 mK whereas for the 7.5 MHz resonator, the dissipation increases linearly over the whole temperature range measured and the peak in resonant frequency too shifts up to 800 mK. This is a remarkable result as it clearly indicates the TLS in the gold layer are contributing to the overall dissipation of the nanomechanical resonator. As mentioned previously, experiments on bare silicon nitride resonators would help to separate the contributions to the energy dissipation from the silicon nitride and gold layers, and then to determine the origin of TLS in these resonators.

5.4.3 Recent studies on Si_3N_4 resonators

The work described in this Chapter is the first systematic study of low temperature dissipation in high-stress silicon nitride doubly-clamped nanomechanical beams. Only a couple of other research groups have studied the energy loss in this material in the recent years.

In a recent publication [71], Southworth et al, reported low temperature dissipation measurements on LPCVD, high-stress Si_3N_4 membrane resonators with $f_0 = 1.5$ MHz. It is worth noting that our silicon nitride layers were grown in the same growth chamber as theirs [52], therefore a similar tensile stress for both is expected ($\sim$ 1000-1200 MPa). Southworth

et al, studied the energy dissipation in their high-stress membranes from room temperature down to 1 K, with the dissipation being in the range $10^{-7} \leq Q^{-1} \leq 10^{-6}$ as shown in Figure 5.10 [71], three orders of magnitude below the glassy range, but close to the values we obtain in our nanomechanical resonators. They also measured the energy loss in stress relieved LPCVD Si_3N_4 cantilevers with $f_0 = 3.5$ MHz, with a dissipation closer to the usual glass plateau ($10^{-4} - 10^{-3}$). This indicates that the tension in the structure can significantly enhance the Q-factor. Furthermore, the authors carried out X-ray diffraction measurements and TEM imaging to confirm that Si_3N_4 is indeed glassy, as is SiO_2, in contrast to the Si lattice.

Dissipation in Si_3N_4 nanomechanical resonators has also been briefly mentioned in references [9, 82]. J. B. Hertzberg measured the dissipation in a Al-Si_3N_4 sample: the nanomechanical resonator was 30 μm long, 170 nm wide and 140 nm thick, formed of 60 nm of stoichiometric, high-stress, LPCVD Si_3N_4 and 80 nm of aluminium, with a frequency $f_0 = 6.3$ MHz. A linear temperature dependence of dissipation in the resonator was observed from base temperature up to 600 mK with $Q \sim 10^6$ at 100 mK [82], similar to that for our 25.5 μm long resonator with a thin gold electrode.

5.5 Summary and Conclusions

The dissipation and resonant frequency in gold-coated high-stress silicon nitride nanomechanical resonators was measured at temperatures below 1.5 K. The data can be qualitatively explained in the framework of the STM, however quantitative agreement with theory is not obtained. Throughout most of the temperature range measured, the dissipation decreased linearly with temperature, with a non-zero value at $T = 0$ suggesting the presence of a temperature independent mechanism in our resonators, the most likely candidate being a tension dependent clamping loss. The resonant frequency increased logarithmically with temperature at the lowest temperatures, with saturation observed at the higher temperatures observed for the flexural modes of the 25.5 μm long beams. The values of C obtained from the fits to the frequency data are roughly two orders of magnitude smaller than those for bulk amorphous solids (glassy range). Nevertheless, the strong variation of the damping and the logarithmic dependence of the resonant frequency on temperature suggest that tunnelling TLS are indeed a source

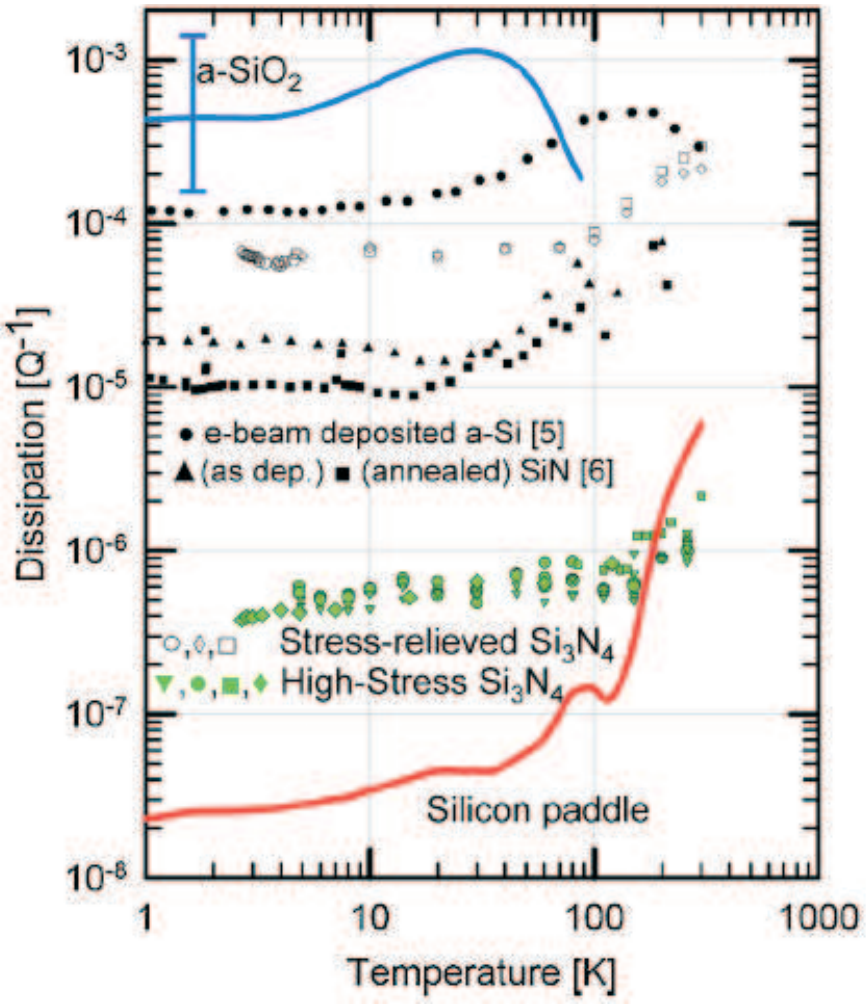

Figure 5.10: Temperature dependence of internal friction measured in high stress LPCVD Si_3N_4 membranes. Results from measurements in a-SiO_2, Si, e-beam deposited a-Si, stress relieved Si_3N_4 cantilevers are shown for comparison [71].

of dissipation in nanomechanical resonators, although their origins are not very well known.

Our results also confirm that a metallic layer on top of a dielectric resonator can have significant effects in the overall dissipation in the system, not just in the magnitude but also in the temperature dependent behaviour, as illustrated by the different results obtained from similar size beams with different thicknesses of gold. Discrepancies between our results and theories based on bulk amorphous solids are to be expected, not just because TLS relaxation rates should be rather different in nanomechanical resonators [70], but also because of the very small volume of the samples [75] together with the effects of tension [71] may lead to a distribution of TLS quite different to that usually assumed for bulk solids.

Further experiments on high-stress silicon nitride resonators are required to be able to draw more firm conclusions about the dissipation mechanisms in such structures. Measurements on beams with different metallic layers (for example alumnium) and thickness and on bare silicon nitride nanomechanical resonators would help to quantify the contributions from the dielectric and metallic layers to the overall dissipation in the system.

Chapter 6

Nonlinear dynamics of a silicon nitride nanomechanical beam at low temperatures

The theory and results described in Chapters 2-5 have been limited to the linear regime of operation. However, in real oscillating structures various types of nonlinearities exist. Sources of nonlinearities in small vibrating elastic beams include material, inertial, geometric and damping effects. In the case of a doubly-clamped beam, a common source of nonlinearity is the lengthening of the structure as it is displaced which causes a nonlinear restoration force to be introduced in the equation of motion of the system [83].

The nonlinear dynamics of nanomechanical resonators have been investigated in a range of recent studies [13, 84, 85]. Recently, experiments on the nonlinear modal interactions in a single doubly-clamped macroscopic silicon beam were carried out at room temperature. These experiments focused on the nonlinear coupling between the first and third mode of the beam [14]. Anharmonic modal coupling has also been studied in bulk micromechanical resonators, with both flexural and longitudinal modes coupling to each other [15]. In this chapter we present a low temperature study on the nonlinear dynamics of several vibrational modes of a single doubly-clamped pre-stressed silicon nitride nanomechanical beam. We demonstrate that the

different modes of the same resonator are coupled by the displacement induced tension in the beam.

A theoretical model describing the nonlinear coupling between the different modes is derived using the Euler-Bernoulli equation, extended with a displacement induced tension, as a starting point. A fairly good quantitative agreement is observed between the theoretical model and the experimental results in the low amplitude (weakly nonlinear) regime.

6.1 Theoretical model

We derive the general relations describing the nonlinear behaviour of a single mode of the beam and outline the main equations describing mode coupling, a full derivation for the latter is given in Appendix B. To simplify the derivation, dimensionless quantities have been used. We start by considering a doubly-clamped beam, similar to the one illustrated in Figure 2.2 (Chapter 2), but with the direction of flexure in the y-direction, along the width of the beam. The beam is under an intrinsic tension, T_0, and we assume that the motion of the beam entails a stretching which leads to an additional nonlinear tension term [11].

6.1.1 Geometry of mode functions

In this section we derive an expression for the mode function of a doubly-clamped beam under the influence of tension, which will be used later for the nonlinear analysis. The equation of motion of such a system is just the Euler-Bernoulli equation including the displacement induced tension [11]:

$$\rho A\frac{\partial^2 y}{\partial t^2}+\eta\frac{\partial y}{\partial t}+EI\frac{\partial^4 y}{\partial x^4}-\left[T_0+\frac{EA}{2L}\int_0^L\left(\frac{\partial y}{\partial x}\right)^2 dx\right]\frac{\partial^2 y}{\partial x^2}=F_L, \quad (6.1)$$

where F_L is the external drive force per unit length. The displacement $y(x,t)$ can be divided into a spatial and a time dependent part using separation of variables:

$$y(x,t)=u(t)g(x). \quad (6.2)$$

The beam profile $g(x)$ has the form

$$g(x)=c_1\sinh\left(\frac{k_1x}{L}\right)+c_2\cosh\left(\frac{k_1x}{L}\right)+c_3\sin\left(\frac{k_2x}{L}\right)+c_4\cos\left(\frac{k_2x}{L}\right),$$

or in terms of the dimensionless parameter $X = \frac{x}{L}$,

$$\tilde{g}(X) = c_1 \sinh(k_1 X) + c_2 \cosh(k_1 X) + c_3 \sin(k_2 X) + c_4 \cos(k_2 X), \quad (6.3)$$

where the roots

$$\begin{aligned} k_1 &= \sqrt{U + \sqrt{U^2 + \Omega^2}} \\ k_2 &= \sqrt{-U + \sqrt{U^2 + \Omega^2}} \end{aligned}$$

depend on the tension in the beam. The dimensionless tension parameter $U = \frac{T_0 L^2}{2EI}$ and dimensionless frequency parameter $\Omega = \omega_0 L^2 \sqrt{\frac{\rho A}{EI}}$ have already been defined in Chapter 2 but are included here for completeness. The boundary conditions (relations 2.14, Chapter 2) imply that $c_2 = -c_4$ and $c_1 = -\frac{k_2}{k_1} c_3$ which leads to the simultaneous equations:

$$\begin{aligned} c_1[k_2 \sinh(k_1) - k_1 \sin(k_2)] + c_2 k_2[\cosh(k_1) - \cos(k_2)] &= 0 \quad (6.4) \\ c_1 k_1[\cosh(k_1) - \cos(k_2)] + c_2[k_1 \sinh(k_1) - k_2 \sin(k_2)] &= 0. \quad (6.5) \end{aligned}$$

Assuming $c_1 = 1$, c_2 can be expressed as

$$c_2 = \frac{k_1 \sin(k_2) - k_2 \sinh(k_1)}{k_2[\cosh(k_1) - \cos(k_2)]} = \Gamma.$$

The normalized mode function can then be written as

$$\tilde{g}(X) = c_0[\sinh(k_1 X) + \Gamma \cosh(k_1 X) - \frac{k_1}{k_2} \sin(k_2 X) - \Gamma \cos(k_2 X)], \quad (6.6)$$

where c_0 is a normalization constant which is determined by the requirement $\int_0^1 \tilde{g}^2(X) dX = 1$.

6.1.2 Single modes

We now derive the equations which describe the nonlinear behaviour of the n-th flexural mode. We start with the equation of motion without any drive ($F_L = 0$) and substitute in for the displacement $y = W \tilde{u}_n \tilde{g}_n$, where W is the width of the beam and $\tilde{u}_n$, $\tilde{g}_n$ are both dimensionless. Equation 6.1 becomes

$$\rho A \ddot{\tilde{u}}_n \tilde{g}_n + \eta \dot{\tilde{u}}_n \tilde{g}_n + [EI \tilde{g}_n'''' - T_0 \tilde{g}_n''] \tilde{u}_n - \frac{EAW^2}{2L} \left[\int_0^L (\tilde{g}_n')^2 dx \right] \tilde{g}_n'' \tilde{u}_n^3 = 0, \quad (6.7)$$

and for an eigenmode we have the relation

$$[EI\tilde{g}_n'''' - T_0\tilde{g}_n''] = \omega_{0n}^2\rho A\tilde{g}_n. \tag{6.8}$$

The spatial derivative is denoted by the prime symbol (u') and the time derivative is denoted by the dot ($\dot{u}$). Substituting equation 6.8 into 6.7, multiplying through by $\tilde{g}_n$ and integrating over X gives the following expression:

$$\ddot{\tilde{u}}_n + \omega_{0n}^2\tilde{u}_n + \gamma\dot{\tilde{u}}_n + \lambda I_{nn}^2\tilde{u}_n^3 = 0, \tag{6.9}$$

with the following parameters defined as: $\gamma = \frac{\eta}{\rho A}$, $\lambda = \frac{EW^2}{2\rho L^4}$ and the integral

$$I_{nn} = \int_0^1 (\tilde{g}_n')^2 dX, \tag{6.10}$$

which determines the coupling strength between the modes and, at least to a good approximation, only depends on tension. In deriving equation 6.7, we have used the fact that $\int_0^1 \tilde{g}_n^2 dX = 1$.

Adopting dimensionless units for time, $t^* = \omega_{0n}t$, means that $\left(\frac{\partial^2\tilde{u}_n}{\partial t^2}\right) = \omega_{0n}^2\left(\frac{\partial^2\tilde{u}_n}{\partial t^{*2}}\right)$, and so using this transformation leads to

$$\ddot{\tilde{u}}_n + \frac{\dot{\tilde{u}}_n}{Q_n} + \tilde{u}_n + \lambda\frac{I_{nn}^2}{\omega_{0n}^2}\tilde{u}_n^3 = 0, \tag{6.11}$$

where $Q_n = \frac{\omega_{0n}}{\gamma}$.

Now we consider the driven case, $F_L = F_0\cos(\tilde{\omega}_n t^*)$, where $\tilde{\omega}_n = \frac{\omega_n}{\omega_{0n}}$ and ω_n is the frequency of the external drive. The driven motion is described by

$$\begin{aligned} \ddot{\tilde{u}}_n + \frac{\dot{\tilde{u}}_n}{Q_n} + \tilde{u}_n + \lambda\frac{I_{nn}^2}{\omega_{0n}^2}\tilde{u}_n^3 &= \frac{\xi_n F_0\cos(\tilde{\omega}_n t^*)}{W\rho A\omega_{0n}^2} \\ &= f\cos(\tilde{\omega}_n t^*), \end{aligned} \tag{6.12}$$

where $\xi_n = \int_0^1 \tilde{g}_n dX$ is known as the mode parameter which indicates the average displacement of the mode per unit deflection and f is the dimensionless force. To solve equation 6.12, the general solution

$$\tilde{u}_n = a_n\cos(\tilde{\omega}_n t^*) + b_n\sin(\tilde{\omega}_n t^*) \tag{6.13}$$

is used where a_n and b_n are the dimensionless amplitudes of the two quadrature responses of the resonator, with the total dimensionless response amplitude being $r_n^2 = a_n^2 + b_n^2$. Substituting equation 6.13 into 6.12, and using standard trigonometric identities leads to the following equation:

$$\begin{aligned}
&(1-\tilde{\omega}_n^2)(a_n\cos(\tilde{\omega}_n t^*) + b_n\sin(\tilde{\omega}_n t^*)) \\
&+\frac{\tilde{\omega}_n}{Q_n}(-a_n\sin(\tilde{\omega}_n t^*) + b_n\cos(\tilde{\omega}_n t^*)) \\
&+\lambda\frac{3I_{nn}}{4\omega_{0n}^2}[b_n^3\sin(\tilde{\omega}_n t^*) + a_n^3\cos(\tilde{\omega}_n t^*) \\
&\quad +a_n^2 b_n\sin(\tilde{\omega}t^*) + b_n^2 a_n\cos(\tilde{\omega}_n t^*)] \;=\; f\cos(\tilde{\omega}_n t^*), \qquad (6.14)
\end{aligned}$$

where we have dropped the terms that oscillate at higher multiples of $\tilde{\omega}_n$ as they are expected to have little effect.

The amplitudes a_n and b_n are obtained by equating the coefficients of $\cos(\omega t)$ and $\sin(\omega t)$, determined through Fourier analysis (multiplying both sides of equation 6.14 by $\cos(\omega t)$ ($\sin(\omega t)$) and integrating over the period) [86], which translates to

$$a_n^2 = \frac{f^2}{H^2\left(1+\left(\frac{\tilde{\omega}_n}{HQ_n}\right)^2\right)} \qquad (6.15)$$

$$b_n^2 = \frac{\tilde{\omega}_n^2}{H^2Q_n^2}a_n^2, \qquad (6.16)$$

where

$$H = (1-\tilde{\omega}_n^2) + \frac{3}{4}\frac{I_{nn}^2}{\omega_{0n}^2}\lambda r_n^2. \qquad (6.17)$$

The response amplitude r_n is given by

$$r_n^2 = \frac{f^2}{\left[(1-\tilde{\omega}_n^2) + \frac{3}{4}\frac{I_{nn}^2}{\omega_{0n}^2}\lambda r_n^2\right]^2 + \left(\frac{\tilde{\omega}_n}{Q_n}\right)^2}, \qquad (6.18)$$

which is the usual behaviour of a Duffing oscillator [86]. At small amplitudes, on resonance, the relationship between the amplitude and f is linear as long as the Q-factor does not change much. For a high Q-factor and a relatively small r_n, the effect of the nonlinearity is to produce a frequency shift. From

equation 6.18 we can extract the relation:

$$\omega_{1n}^2 = \omega_{0n}^2 \left(1 + \frac{3}{4}\frac{I_{nn}^2}{\omega_{0n}^2}\lambda r_n^2\right). \tag{6.19}$$

By taking the square root of 6.19 and carrying out a binomial expansion of the right hand side, the frequency is, to a first approximation, given by

$$f_{1n} = f_{0n} + \frac{3}{32\pi^2}\frac{I_{nn}^2}{f_{0n}}\lambda r_n^2, \tag{6.20}$$

where only the first two terms in the expansion have been kept as the rest are deemed to be negligible. Notice how the frequency of the resonator shifts as the amplitude increases, an effect known as 'frequency pulling', one of the signatures of nonlinear behaviour.

6.1.3 Coupled modes

We now consider the situation where two modes (m and n) are driven simultaneously close to the bare mode frequencies ω_{0m} and ω_{0n}. The case where one mode is driven weakly (linear) whilst the second mode is slowly driven into the strongly nonlinear regime, is of particular interest, as it allows us to quantify the mode coupling. In a similar expression to the single mode analytical model (equation 6.20), the frequency of a weakly driven mode n as a function of amplitude of the strongly driven mode m is

$$f_{2n} = f_{1n} + r_m^2 \frac{\lambda}{8\pi^2 f_{1n}}\left(\frac{I_{nn}I_{mm}}{2} + I_{nm}^2\right). \tag{6.21}$$

The above analysis provides a way of calculating the amplitude at the drive frequencies of both, n and m modes, with higher harmonics being neglected. It also assumes that the resonances are resolvable: $|\omega_{0m} - \omega_{0n}| \gg \frac{\omega_{0m}}{Q_m} + \frac{\omega_{0n}}{Q_n}$ for $m \neq n$. Within this approximation, the amplitudes are given by the relations:

$$r_n^2 = \frac{f_n^2}{\left[1 - \tilde{\omega}_n^2 + \frac{3}{4}\frac{I_{nn}^2}{\omega_{0n}^2}\lambda r_n^2 + r_m^2\frac{\lambda}{\omega_{0n}^2}\left(\frac{I_{nn}I_{mm}}{2} + I_{nm}^2\right)\right]^2 + \left(\frac{\tilde{\omega}_n}{Q_n}\right)^2} \tag{6.22}$$

$$r_m^2 = \frac{f_m^2}{\left[1 - \tilde{\omega}_m^2 + \frac{3}{4}\frac{I_{mm}^2}{\omega_{0m}^2}\lambda r_m^2 + r_n^2\frac{\lambda}{\omega_{0m}^2}\left(\frac{I_{nn}I_{mm}}{2} + I_{nm}^2\right)\right]^2 + \left(\frac{\tilde{\omega}_m}{Q_m}\right)^2}. \tag{6.23}$$

These equations give r_n and r_m as functions of the two drive frequencies ω_n and ω_m; the full derivation is shown in Appendix B.

6.2 Relationship between beam displacement and measured signal

In sections 6.1.2 and 6.1.3, we derived equations for the dimensionless amplitude r, which can be related to a physical amplitude (R) via the mode function $g(x)$ and the width of the beam: $R = Wrg(x)$. The signal measured is a voltage V_S, proportional to the V_{EMF} generated by the motion of the beam. Here, we establish the relationship between the dimensionless amplitude and the measured voltage, which will be used later when analyzing the experimental results.

The measured signal is related to the EMF generated by the device through the equation

$$V_S = GV_{emf} = GW\xi_n LB\omega \frac{\partial \tilde{u}}{\partial t^*}, \tag{6.24}$$

where G is just a constant of proportionality that quantifies the signal gain from the sample to the the network analyzer (output transmission line). The behaviour of $\tilde{u}$ is assumed to be purely harmonic at the drive frequency (see equation 6.13), and the measured signal is assumed to have the form $V_S = V_1 \cos(\tilde{\omega}t^*) + V_2 \sin(\tilde{\omega}t^*)$. Expanding equation 6.24 leads to

$$V_1 \cos(\tilde{\omega}t^*) + V_2 \sin(\tilde{\omega}t^*) = GW\xi_n LB\omega[b\cos(\tilde{\omega}t^*) + a\sin(\tilde{\omega}t^*)], \tag{6.25}$$

and a relationship between r and V_S is obtained by equating the coefficients for $\cos(\tilde{\omega}t^*)$ and $\sin(\tilde{\omega}t^*)$:

$$r^2 = \frac{1}{G^2}\left(\frac{1}{W\xi_n LB\omega}\right)^2 V_S^2 = DS^2, \tag{6.26}$$

where $D = \frac{1}{G^2}$ and S is the dimensionless measured signal.

It has to be noted that the gain in the transmission line will actually vary slightly with frequency and will therefore be slightly different for each mode. Once D is known, it is possible to convert the signal measured V_S into a physical displacement using equation 6.24, and hence determine the

amount by which the nanomechanical resonator is moving when driven.

6.3 Experimental techniques and results

Measurements were conducted on the first, third and fifth flexural mode of a beam with dimensions: $L \sim 25.5$ μm, $W \sim 170$ nm, $h \sim 170$ nm and a 40 nm thick layer of gold on top. Results for the nonlinear response of each individual mode and the nonlinear modal coupling are presented with comparisons to the theory.

6.3.1 Measurement set-up

The nonlinear studies were carried out after the dissipation experiments described in Chapter 5. Measurements were performed at a field of 3 T, at 115 mK, using the magnetomotive technique to measure the mechanical motion of the beam. A schematic diagram of the experimental arrangement is shown in Figure 6.1, which is very similar to that used for the dissipation studies (see Chapter 3)[1]. The different modes of the beam were driven with two separate signal generators, one mode with the Agilent 8712ET network analyzer and the other with the Agilent E4420B signal generator. The two signals were fed into a Mini-Circuits ZSC-2-1 power combiner and the sum of the signals was sent to the device. A voltage signal, proportional to the EMF generated by the beam, was detected at the input of the network analyzer after passing through two rf pre-amplifiers [60, 62].

6.3.2 Device Parameters

To compare the theory and experimental data, the parameters ξ_n and I_{nn} need to be determined as they are required for the analysis. The parameters ξ_n and I_{nn} were calculated using Matlab, with $\sigma \approx 1020$ MPa assumed for the beam at low temperatures. The values for the three modes measured are shown in Table 6.1 along with generic theoretical values for nanomechanical devices in the limit of zero and high tension [87]. Our values of I_{nn} and ξ_n lie close to the high tension limit as expected due to the large tensile stress experienced by the beam. Furthermore, neither quantity I_{nn} or ξ_n vary much between the two limits. The coupling strengths between the different modes

[1]Figure 6.1 is just a simpler version of Figure 3.12

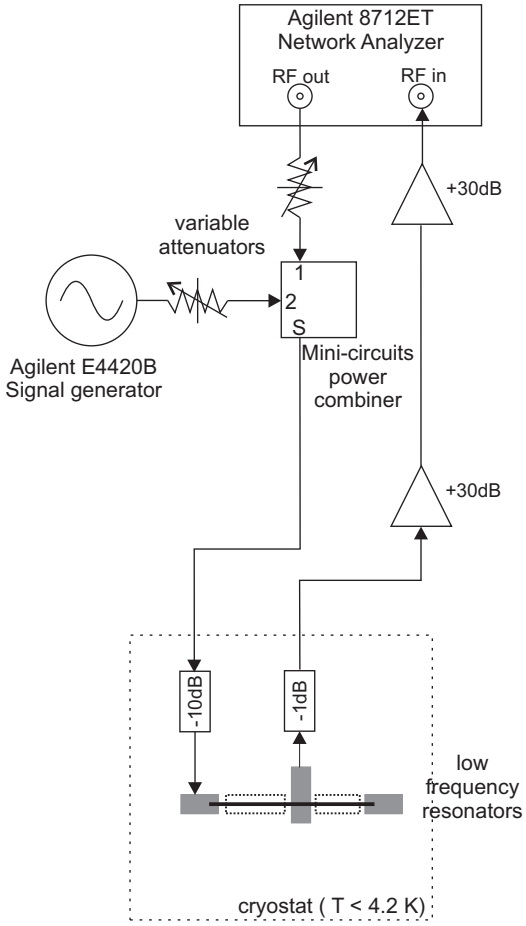

Figure 6.1: Schematic diagram of the measurement set-up used for the nonlinear studies.

Table 6.1: Eigenfrequencies and other device parameters for the three measured eigenmodes of the silicon nitride beam. Theoretical values for the integrals I_{nn} and mode parameters ξ_n for nanomechanical devices calculated in reference [87] in the limit of zero and high tension are also shown here for comparison with our data.

Mode	σ **= 1020 MPa**			**Bending limit**		**Tension limit**	
n	f_{0n} (MHz)	ξ_n	I_{nn}	ξ_n	I_{nn}	ξ_n	I_{nn}
1	7.50	0.88	10.4	0.83	12.3	0.90	9.9
3	22.85	0.30	93.3	0.36	98.9	0.30	88.8
5	39.28	0.19	257.9	0.23	264.0	0.18	246.7

are also determined: $I_{13} = I_{31} = -1.88$, $I_{15} = -2.98$ and $I_{35} = -8.81$. These will be used when analyzing the nonlinear modal coupling data.

6.3.3 Nonlinear behaviour of a single mode

Measurements on each individual mode were performed first, observing the response of the resonator as the driving frequency was swept through the mechanical resonance frequency. This was done for a range of driving amplitudes by systematically decreasing the attenuation in the input transmission line to the sample: 100 $\rightarrow$ 50 dB for mode 1 and 100 $\rightarrow$ 60 dB for modes 3 and 5 (in steps of 5 dB).

Figure 6.2 shows the amplitude response of each mode (with the offsets zeroed) for attenuations of 100 $\rightarrow$ 60 dB. Several features can be pointed out. Firstly the shape of the curves, which look Lorentzian for the smallest drives, become increasingly asymmetric as the beam is driven harder. At the largest drives, the device enters a regime of bistability depicted by the sharp drop seen in the measured signal, illustrated clearly by the curves at 65 and 60 dB, meaning that the resonator behaviour is completely nonlinear for these drives. The phenomenon of 'frequency pulling' is also clearly visible, with the peak frequency of the resonator shifting up as the drive is increased. Furthermore, notice how the third mode becomes nonlinear before the first, whereas the fifth mode response seems to be slightly nonlinear even at the lowest amplitudes. This behaviour is expected as the I_{nn} values increase with n ($I_{55} > I_{33} > I_{11}$).

All the parameters related to the device and which are relevant for the analysis have been determined, however, the quantity $D(= \frac{1}{G^2})$ is still an unknown. From the resonance curves in Figure 6.2 we extract the peak

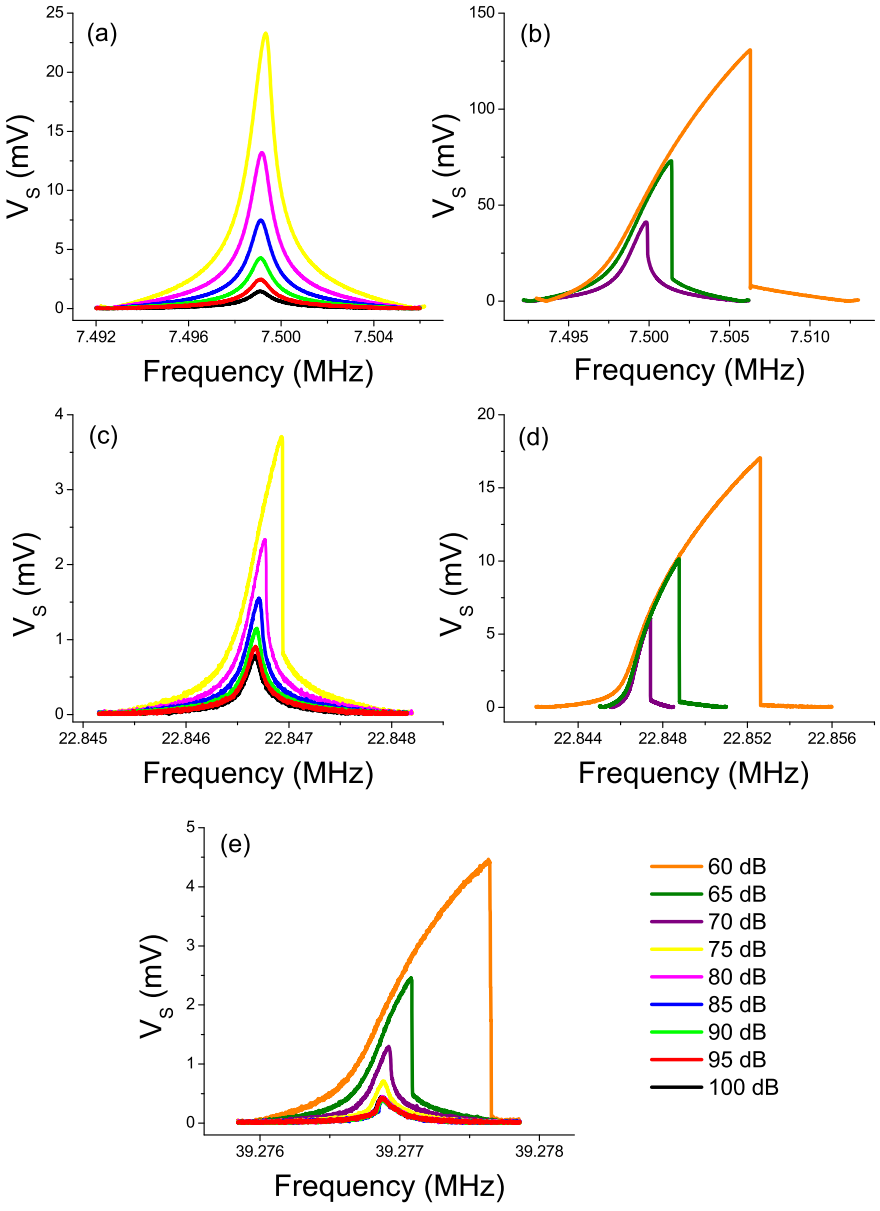

Figure 6.2: Resonant response of (a) & (b) mode 1 (7.5 MHz), (c) & (d) mode 3 (22.85 MHz), and (e) mode 5 (39.28 MHz) for a range of attenuations. Features to notice are the increase in response amplitude with increasing drive, the 'frequency pulling' and the asymmetry of the response shape at the largest drives.

amplitudes and frequencies (f_{1n}) which are then used, along with equations 6.20 and 6.26 to determine D. The relationship between f_{1n}^2 and $\beta_n = \frac{3}{16\pi^2} I_{nn}^2 \lambda S_n^2$ should be linear with a gradient D and an intercept f_{0n}^2. Figures 6.3(a), (c) and (e) show plots of f_{1n}^2 as a function of β_n and the corresponding linear fits over the whole data range, from which we extract f_{0n} and D_n. As can be seen, the fits to the full data range for modes 1 and 3 are not very good and therefore we decide to fit to a narrower range (weakly nonlinear regime) where the data and the model have a much better agreement, as shown in Figures 6.3(b) and (d). The fit parameters are displayed in Table 6.2 along with their respective errors.

In the transmission line from the sample to the network analyzer, there are two room temperature rf pre-amplifiers which provide a total gain of about +62 dB (+31 dB each). The total loss in the cables and other rf components inside the fridge was measured to be about -2 to -3 dB at room temperature, in the frequency range relevant here. However, the measurements were made at 115 mK, and the attenuation inside the cryostat changes with temperature; unfortunately we have no low temperature measurements for the losses in the cables so it is reasonable to assume that the amplification in the transmission line is known to an accuracy of ± 3 dB. Within this error, it is acceptable to say that the values of G obtained from the fits are consistent with each other. For the rest of the analysis, we use the values of D_1 and and D_3 obtained from fitting to the lower drive range of data.

Table 6.2: Parameters extracted from the linear fits to the data shown in Figure 6.3 where D_n is the gradient and f_{0n} the intercept along with their respective errors obtained from the fits. The gain $G = 1/D^2$.

Figure	**n**	$\mathbf{f_{0n}}$ **(MHz)**	$\mathbf{D_n}$	$\mathbf{G_n}$	$\mathbf{G_n}$ **(dB)**
6.3(a)	1	7.498280	$(1.11 \pm 0.04)\times10^{-6}$	948 ± 16	59.5 ± 0.4
6.3(b)	1	7.499099	$(7.15 \pm 0.06)\times10^{-7}$	1183 ± 5	61.5 ± 0.1
6.3(c)	3	22.846794	$(1.14 \pm 0.06)\times10^{-6}$	935 ± 23	59.4 ± 0.5
6.3(d)	3	22.846666	$(1.79 \pm 0.01)\times10^{-6}$	748 ± 2	57.5 ± 0.1
6.3(e)	5	39.276863	$(8.80 \pm 0.09)\times10^{-7}$	1066 ± 6	60.5 ± 0.1

The physical displacement of each mode (at a given drive) was obtained through expression 6.24 and the current passing through the device was determined by fitting the response curves (Figure 6.2) to equation 6.18 with the drive current I_0 and the Q-factor as the only fit parameters. On resonance, for small response amplitudes, the theory predicts a linear relationship be-

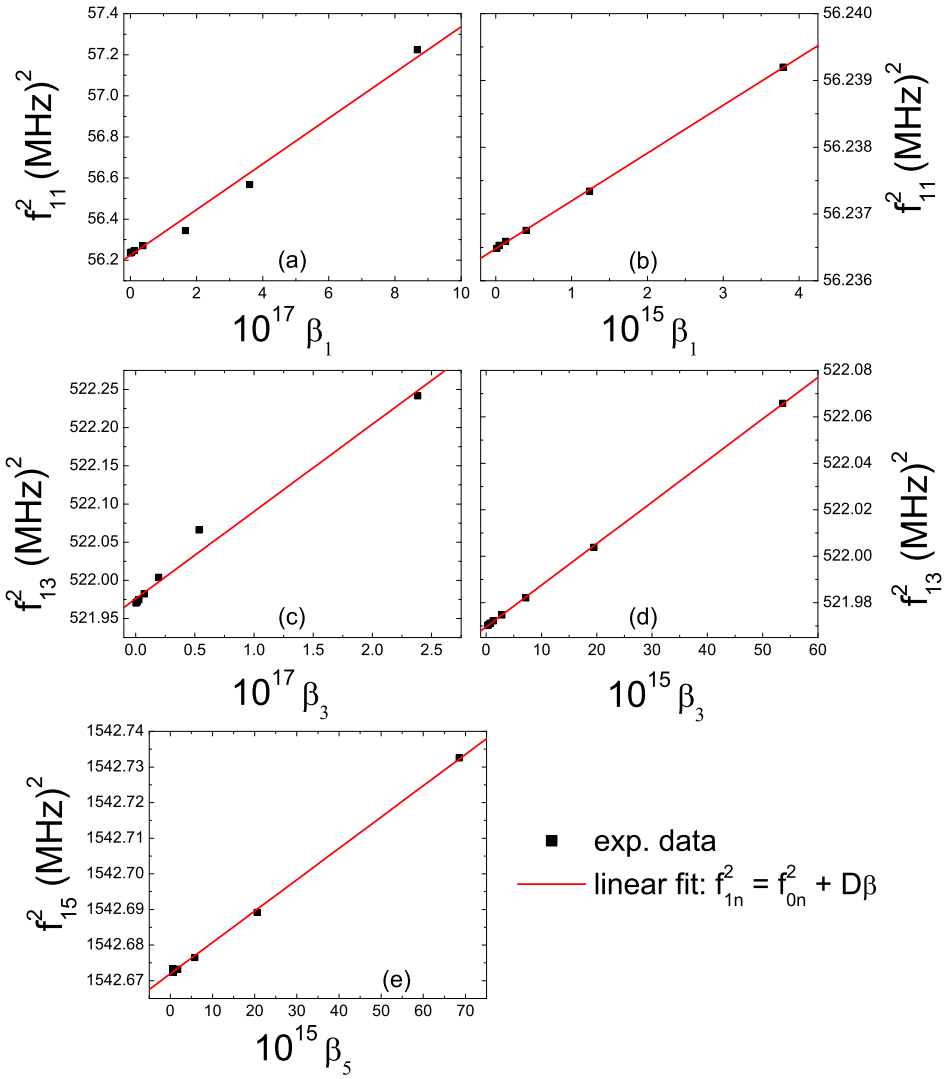

Figure 6.3: Plots of f_{1n}^2 versus β_n for the full range of data for (a) mode 1, (c) mode 3, (e) mode 5 and in the small amplitude region for (b) mode 1 and (d) mode 3. The smooth red lines are fits to the data from which f_{0n} and D_n are extracted.

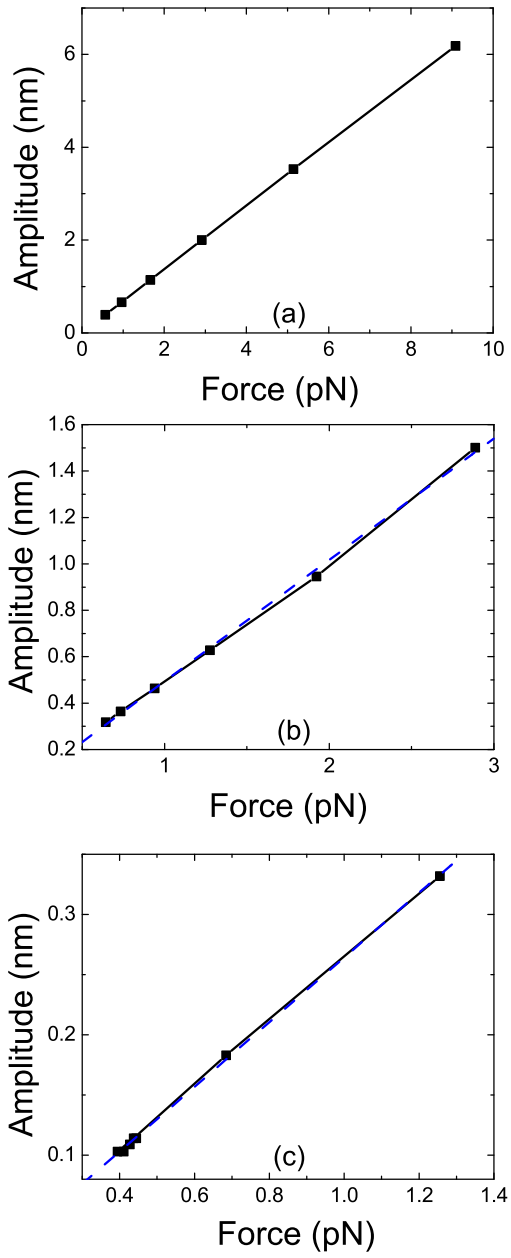

Figure 6.4: Amplitude versus force for all three modes showing the expected linear relationship in the low amplitude regime. The dashed blue lines represent linear behaviour and the slight deviations of the experimental data, for modes 3 and 5, from this behaviour are due changes in their Q-factor.

tween the force ($F_0 = BI_0L$) and the amplitude and our data confirms this as illustrated in Figure 6.4. At larger amplitudes, the Q-factor of the resonator starts to change and the linear relationship no longer holds. In Figures 6.4(b) and (c), the slight discrepancies between the measurements and linear behaviour (denoted by the dashed blue line) seen for modes 3 and 5 are due to minor changes in the Q-factor with drive.

The fits to the experimental data suggest a fairly good quantitative agreement between the nonlinear response of an individual mode and the theoretical model, as the fitted values of D are within the range expected.

6.3.4 Nonlinear modal coupling

The nonlinear interactions between the different modes of the beam were also probed. Measurements were performed where we looked at frequency shifts in a weakly driven mode whilst the amplitude of another mode was gradually increased. We looked at the effects of the amplitude of the first mode (driven at 7.499 MHz) on f_3 and f_5 and the amplitude of the third mode (driven at 22.84665 MHz) on f_1 and f_5. In Figure 6.5 the frequency response of the third mode is shown for three different response amplitudes of the first mode. The third mode is driven weakly and its drive amplitude is kept constant. Note that its resonant frequency increases when the amplitude of the first mode becomes larger, but no significant change is seen in the amplitude or the shape of the f_3 response curve.

The resonant frequencies of the third mode and fifth modes (f_3 and f_5) as a function of the amplitude of the first mode are shown in Figures 6.6(a) and (b). Similarly, Figures 6.7(a) and (b) show the effect of the amplitude of the third mode on the resonant frequency of the first and fifth modes. Jumps in the resonant frequencies f_{21} and f_{25} were observed when carrying out the latter measurements. The resonant frequencies f_{2n} for $S_m = 0$ were measured at a different time to the rest of the data, and in between measurements, frequency jumps of $\Delta f_{21} \sim 150$ Hz and $\Delta f_{25} \sim 45$ Hz occurred which have been accounted for in the plots. The blue dashed lines represent the theoretical model using the D_n value obtained from the single mode analysis (see Table 6.2). The red lines are quadratic fits to the data (using equations 6.21 and 6.26) with D_n as the only free parameter. The fitted values are displayed in Table 6.3. Within the error margins assumed for the gains, good agreement is found between the observed frequency shift

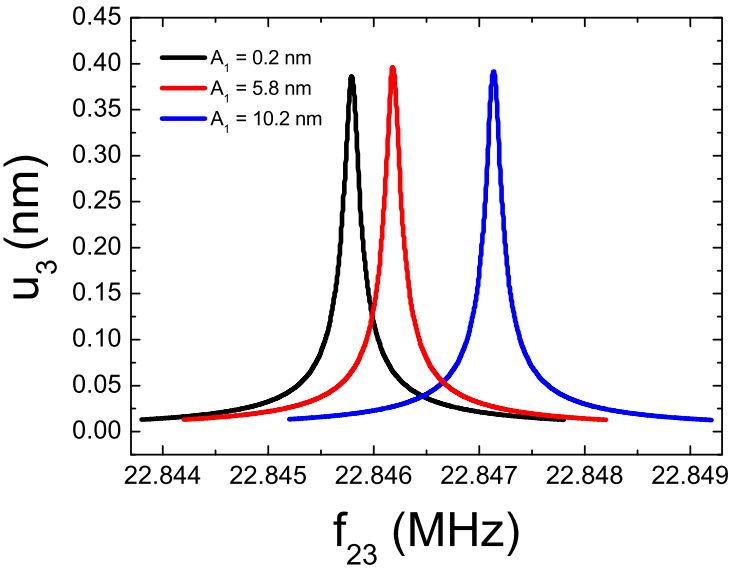

Figure 6.5: Frequency responses of the third mode for different response amplitudes of the first mode at a frequency of 7.499 MHz.

and the quadratic behaviour predicted by the theoretical model.

Table 6.3: Parameters extracted from the quadratic fits to the data shown in Figures 6.6 and 6.7 where D_n is the only free quantity.

Figure	**n**	$\mathbf{D_n}$	$\mathbf{G_n}$ **(dB)**
6.6(a)	1	$(1.01 \pm 0.01)\times10^{-6}$	60.0 ± 0.1
6.6(b)	1	$(8.26 \pm 0.30)\times10^{-7}$	60.8 ± 0.4
6.7(a)	3	$(1.96 \pm 0.10)\times10^{-6}$	57.1 ± 0.2
6.7(b)	3	$(1.53 \pm 0.10)\times10^{-6}$	58.2 ± 0.1

The nonlinear modal coupling between the first and third mode was further investigated by driving the first (third) mode at a fixed amplitude, with an attenuation of 63 dB (73 dB), varying its drive frequency f_1 (f_3) and sweeping through the third (first) mode (which is driven weakly) at each frequency step. This is illustrated in Figures 6.8(a) and (b), showing both forward and backward sweeps. From the plots we can confirm that the modes interact with each other as the nonlinear line shape of one mode is reflected in the response of the other mode. In both cases, the strongly driven modes are completely in the nonlinear regime as can be noticed from

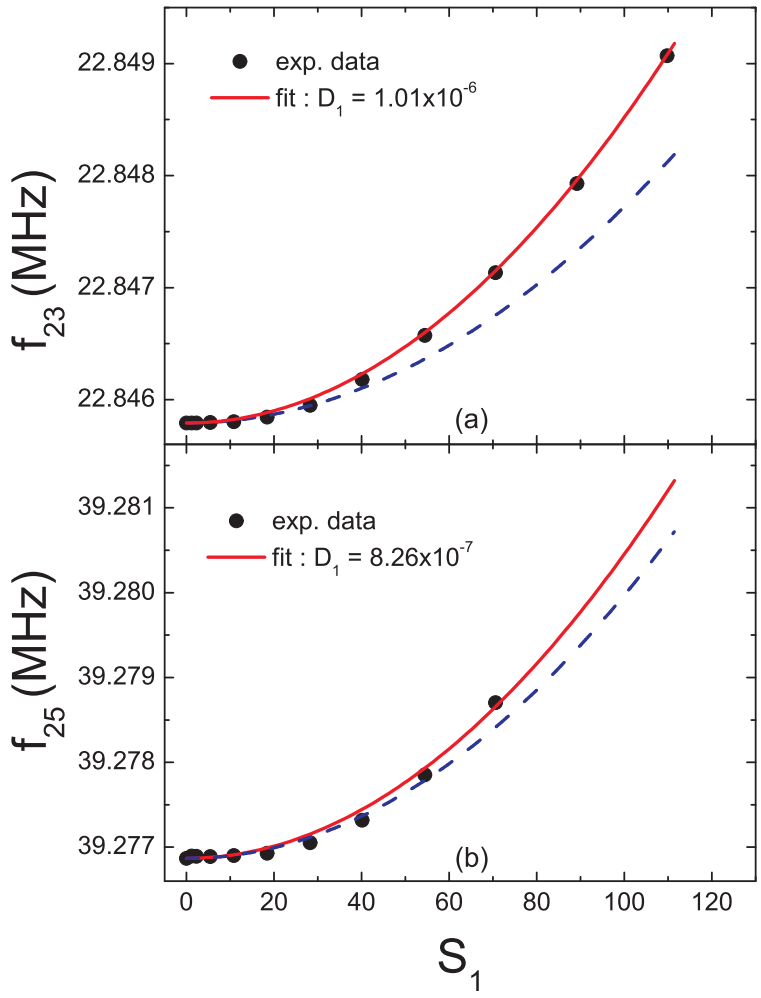

Figure 6.6: Resonant frequency of (a) mode 3 and (b) mode 5, as a function of S_1. Within the error margins assumed for G_1, a quadratic dependence over the whole data range is observed, in good agreement with theory. The blue dashed lines represent the model using the D_n value obtained from the single mode analysis (see Table 6.2).

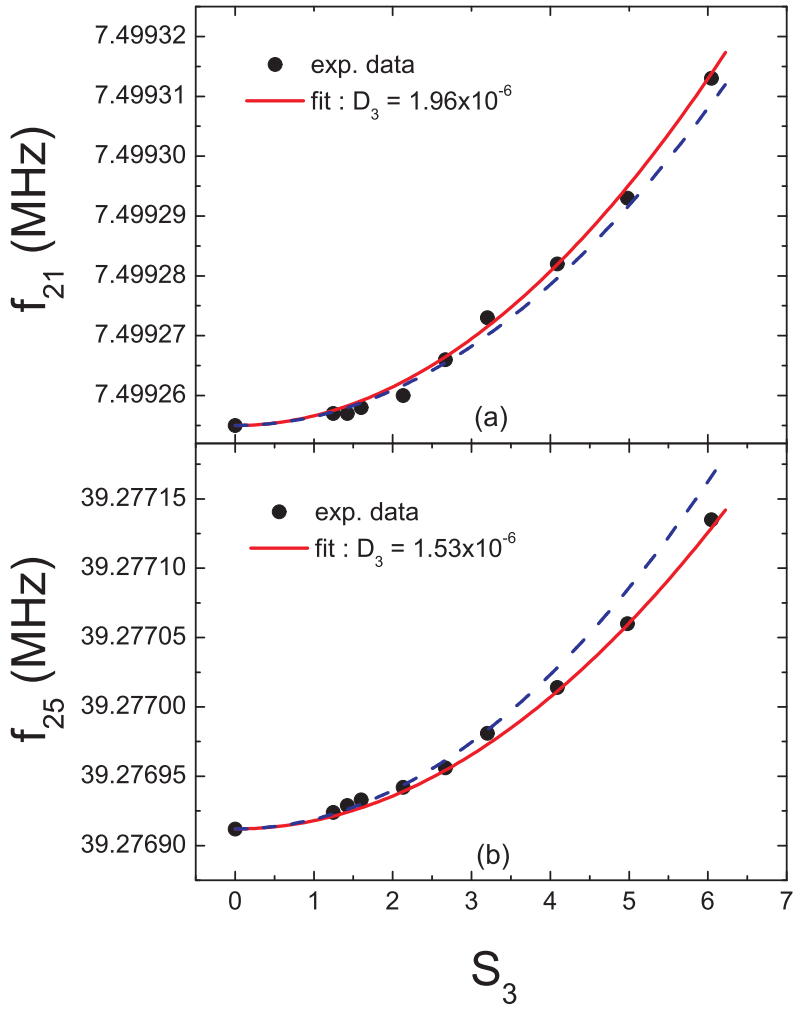

Figure 6.7: Resonant frequency of (a) mode 1 and (b) mode 5, as a function of S_3. Within the error margins assumed for G_3, a quadratic dependence over the whole data range is observed, in good agreement with theory. The blue dashed lines represent the model using the D_n value obtained from the single mode analysis (see Table 6.2).

the hysteretic behaviour and bistability.

The quadratic curve (red line) in Figure 6.6(a) was used to map the resonant frequencies f_{23} into amplitudes S_1. As the input attenuation for this measurement was 63 db, this curve should lie in between the first mode resonance sweeps (see Figure 6.2(b)) measured at attenuations of 60 and 65 dB. This is the case as shown in Figure 6.9 (forward sweep curves). The curve at 63 dB is slightly deceiving because of the lack of points, indicated by the sharp drop seen at the peak frequency, which is not quite as vertical as for the other two curves.

6.4 Heating effects

The temperature of a nanomechanical resonator can change depending on the amount of current that passes through it. For the experiments described in this chapter, the larger drives can cause substancial heating of the device and lead to a change in resonant frequency of the beam. It is important to therefore determine whether the frequency shifts we observe are due to heating effects or purely from the stretching of the sample. Figure 5.8 in Chapter 5 clearly shows that the frequencies of the flexural modes measured do not vary much with temperature as the frequency shifts observed are of the order of tens of Hertz and saturation is observed above about 1 K. Nonetheless, we carry out a very simple calculation to estimate how much the fundamental mode of the device (7.5 MHz) heats up with increasing driving power.

The heat transfer is dominated by the conduction along the beam. The temperature of the beam can raise through electrical heating as well as through stretching. We first estimate the electrical heating contribution. Assuming the temperature at the clamping points is fixed at T_p, and that maximum heating occurs at the centre of the beam, the heat conduction from the centre of the beam to a clamping point is given by [88]

$$P = 2kA\frac{\Delta T}{L}, \tag{6.27}$$

where $P = I^2R$ is the power generated, k is the thermal conductivity of the beam, A its cross-sectional area and ΔT is the temperature difference between the centre of the beam and the clamping point. At this point we

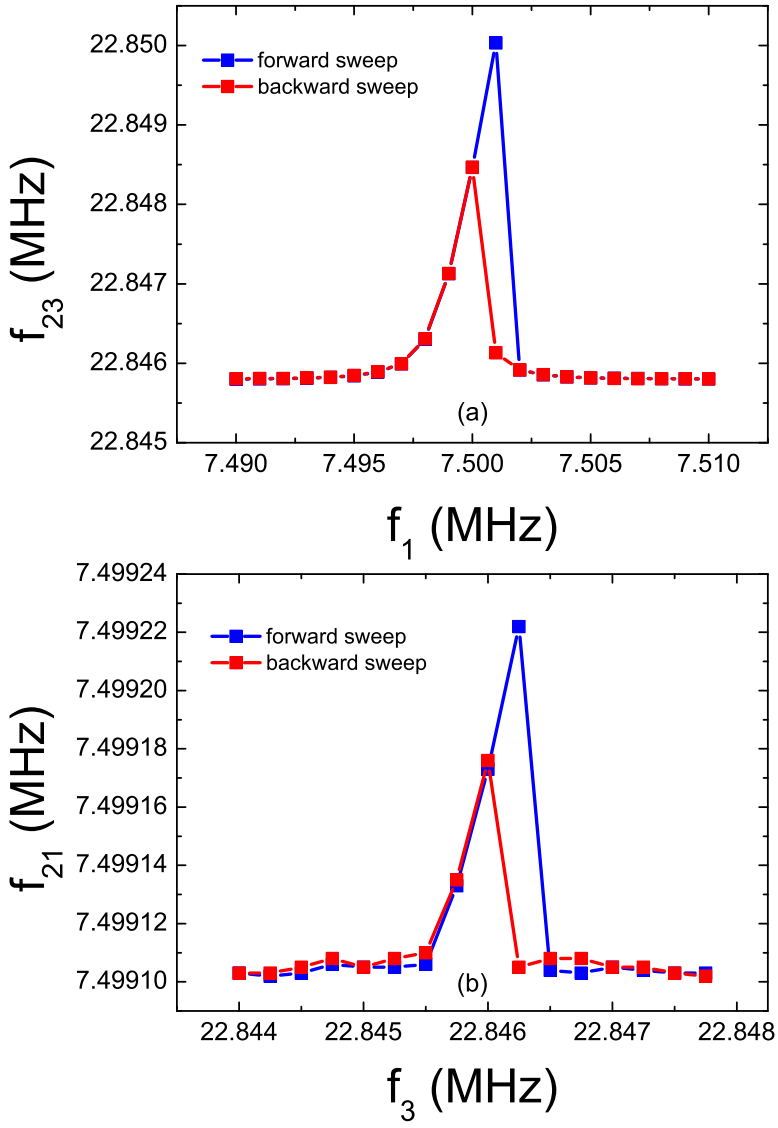

Figure 6.8: (a) Resonant frequency of the mode 3 as a function of mode 1 drive frequency. Mode 3 is driven weakly with an attenuation of 100 dB whereas as mode 1 is driven strongly with an attenuation of 63 dB. (b) Resonant frequency of mode 1 as a function of mode 3 drive frequency. Mode 1 driven weakly (attenuation: 100 dB) and mode 3 driven strongly (attenuation: 73 dB).

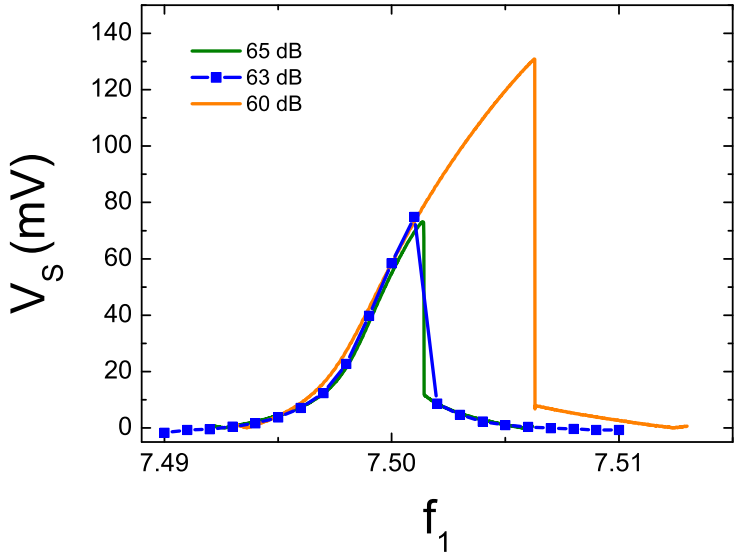

Figure 6.9: Frequency response is plotted for the amplitude of mode 1 (forward sweep). The amplitude at 63 dB of attenuation obtained through the conversion of f_{23} into S_1.

make another assumption which is that all the heating takes place in the gold layer, and therefore we completely neglect the effect of the nitride layer.

The Wiedemann-Franz law relates the thermal conductivity (k) and electrical resistivity (ρ_e), at temperature T, according to $k\rho_e = L_0 T$, where $L_0 = 2.44 \times 10^{-8}$ WΩ/K^2 is a universal constant known as the Lorenz number [88]. Substituting this into equation 6.27 and rearranging for ΔT leads to:

$$\Delta T = \frac{V^2}{2L_0 T}, \tag{6.28}$$

where V is the voltage across the resonator. Using equation 6.28 we estimate that the temperature of the sample heats up by less than 1 mK at the lowest drives, but can heat up by more than 1 K for the highest drive. Nevertheless, these values are only very rough estimates as the calculations are not very rigorous. This type of heating can cause frequency shifts but cannot lead to the bistable behaviour we observe at the highest drives.

The heating from the elongation of the resonator depends on energy lost per cycle in the system, $\Delta E \approx \frac{E}{Q_0}$, where $E = \frac{1}{2}mv^2$ is the energy stored in the resonator. The velocity v can be estimated from relation 6.24 and

$Q_0 \approx 10^6$ at 100 mK (temperature at which measurements were performed). Using these values we found that the temperature of the sample increased by a few microkelvin, even for the largest drives.

It has to be noted that the calculations described here are only approximations, as there are so many unknowns which make it difficult to obtain more accurate estimates of the heating. As mentioned previously, however, it is unlikely that the observed nonlinear behaviour is due to heating effects as the results match fairly well with our theoretical model.

6.5 Summary and Conclusions

In this chapter we have derived equations describing the nonlinear response of pre-stressed nanomechanical resonators, taking the Euler-Bernoulli equation with an added displacement induced tension term, as a starting point. A time dependent equation of motion with a cubic term in displacement (Duffing nonlinearity) is obtained which is solved for the situations when only one mode is driven and when two modes are driven simultaneously. The theory predicts a quadratic dependence of the resonant frequency on the amplitude in both cases.

Our measurements prove that all three resonances belong to the same nanomechanical beam and not to another slightly shorter resonator which was in series with the one being measured (see bridge arrangement in Figure 6.1). We have observed the nonlinear behaviour of the three individual modes and also measured the coupling between them by driving the beam at multiple frequencies. This interaction is very important in nanomechanical resonators and has to be included when describing the mechanical motion of the higher flexural modes of such devices. The model is in good agreement with the measurements and quantitatively captures the observed nonlinear behaviour, with D as the only free parameter. The fitted values of D translate to gains of about +60 dB which is close to what is expected. As the attenuation in the output line of the dilution fridge is not known at low temperatures, we assume that at best the gain G will have an error of about 2-3 dB.

The nonlinear coupling can be used to detect the effect of different resonance modes on each other. The amplitude of one mode can be determined by looking at the frequency shift in another. The fact that the silicon ni-

tride beam investigated here has a stress of about 1020 MPa (which leads to a high Q) makes it easier to probe the nonlinear coupling which would otherwise be difficult to measure in un-stressed nanomechanical resonators.

Chapter 7

Summary and future work

In this thesis, the dissipation and nonlinear dynamics in nanomechanical resonators at low temperatures have been studied. The nanomechanical resonators were fabricated as doubly-clamped beams using a combination of optical and electron-beam lithography followed by dry/wet etching techniques. Their motion was actuated and detected using the magnetomotive transduction scheme. The samples were placed in dilution refrigerators and all measurements were carried out at temperatures below 2 K. The resonance characteristics of the doubly-clamped beams were measured as a function of magnetic field and temperature. By fitting the raw data to a Lorentzian function, we extracted the resonant frequency and Q-factor of the devices. The field dependence study allowed us to extrapolate to the $B = 0$ limit and infer the intrinsic quality factor of the resonators at any temperature.

We investigated the energy loss mechanisms in two polycrystalline gold doubly-clamped beams. The dissipation in gold nanomechanical resonators varies with temperature as $Q_0^{-1} \propto T^{0.5}$ between 30 and 500 mK, saturating above 600 mK. The resonant frequency of the beams increase logarithmically with temperature below 400 mK, but at higher temperatures, each resonator behaves differently which makes it difficult to draw any firm conclusions for that regime. The observation of features such as the plateau, and the variation of Q_0^{-1} and f_0 with temperature suggest that tunnelling TLS are a source of dissipation in metallic nanomechanical resonators at low temperatures.

In order to obtain more information about the origin of TLS in metallic structures as well as their location (surface or bulk), it would be necessary

to study more resonators with a wider range of resonant frequencies. The effects of the fabrication processes can be investigated simply by measuring devices made using different techniques, for example, compare wet etched and dry etched devices. Furthermore, thermal annealing or coating the surface of the resonator with a polymer layer will help determine the importance of surface effects and the nature of the TLS there.

We also carried out measurements on gold-coated high-stress silicon nitride resonators. The dissipation (frequency) in these devices increases linearly (logarithmically) with temperature. Experiments on two beams of similar dimensions but different gold thickness reveal that tunnelling TLS in the gold layer have an important role to play in the overall dissipation of the system.

To allow us to separate the contributions to the damping from the metallic and dielectric layers, it is necessary to carry out further studies on resonators with thinner layers of gold, although a beam without a metal layer on top would be even better. Furthermore, measurements on high-stress membrane oscillators and stress-relieved cantilevers [71] clearly indicate that tension can substantially increase the Q-factor of a resonator. A more established theory on the effects of tension in nanomechanical structures is therefore required to analyze the data more quantitatively.

We also investigated the nonlinear dynamics of a single silicon nitride beam, both theoretically and experimentally. It is demonstrated theoretically that the different flexural modes of a beam are coupled to each other through the amplitude dependent tension in the beam. We performed measurements on the first, third and fifth mode, observing shifts in the frequency of one mode when the drive of another mode was varied, in good agreement with theory.

In conclusion, the experiments described in this thesis provide a good base for a phenomenological understanding of the behaviour of nanomechanical resonators at low temperatures. However, additional measurements are needed to get a full picture of the dissipation mechanisms along with a more established theory to describe some of the observed features quantitatively. Also, a good understanding of the nonlinear dynamics of nanomechanical resonators is vital when describing their motion as well as being able to exploit or avoid these nonlinearities when necessary.

Appendix A

Device fabrication details

In this Appendix, the technical details of the fabrication process for both the gold and silicon nitride nanomechanical beams are described.

A.1 Gold beams on gallium arsenide

The fabrication of the gold nanomechanical resonators can be separated into two parts:

1. Lithography for contact pads and nano-wires.
2. Defining a suitable etch window to release the beams

A.1.1 Lithography for contact pads and nano-wires

Trilayer resist coating After being cleaned in solvents ethyl lactate, acetone, methanol and isopropanol (IPA) in ultrasound for five minutes each, the GaAs chip was first coated with a 400 nm layer of lift-off resist LOR5B, which was spun at a speed of 4000 rpm for 45 s followed by a 5 minute bake on a hot plate at 180°C. The chip was then covered with a 35 nm thick layer of Ge, thermally evaporated with a deposition rate of 0.5 nms^{-1} keeping the evaporator chamber pressure below 10^{-6} mbar. Finally, the sample was spun coated with two layers of 950K PMMA A2 (2% solution of PMMA in anisole) at 4000 rpm for 45 s; each layer was baked on a hot plate for 30 s at 180°C and had a thickness of about 40 nm.

Electron beam lithography The nano-wires and contact pads were patterned via e-beam lithography using a JEOL JSM-7000F field emission scanning electron microscope, with a Xenos XPG-2 pattern generator. An acceleration voltage of 30 kV along with a beam current of 500 pA was used, with a working distance of 9 mm. The patterns were written in a 250 μm field size using doses of 120 μC/cm^2 for the pads, and 280 μC/cm^2 for the nano-wires. After the lithography process, the sample was developed in MIBK:IPA (Methyl Iso-butylketone:Isopropanol) solution in the volume ratio 1:3 for 2 minutes at room temperature, rinsed in IPA and blown dry. The Ge was isotropically etched in reactive ion etching (RIE) mode using an SF_6 plasma (flow rate: 20 sccm and RF power: 60 W) for 20 s. The LOR was isotropically etched in RIE mode using an oxygen plasma (flow rate: 25 sccm and RF power: 60 W) for 5 minutes to provide a Ge/LOR stencil. An inductively coupled plasma system (CORIAL 200IL) was employed for the dry etching.

Metallization The sample was then loaded into a thermal evaporator and metallized with 3 nm of titanium followed by 60 - 80 nm of gold. The evaporator chamber pressure was kept below 10^{-6} mbar and the deposition rates were between 0.3 - 0.5 nms^{-1}.

Lift-off The sample was then soaked in a photo-resist stripper (1165 Microposit Remover) for 30 minutes at 60°C to remove the Ge/LOR stencil leaving the metallized pattern on the GaAs substrate.

A.1.2 Releasing the beams

Bilayer resist coating The sample was coated with a PMMA/LOR bilayer resist. The spin speeds and times along with the baking times were the same as before.

Defining an etch window A window was patterned in the area of interest via e-beam lithography using an acceleration voltage of 30 kV, a 165 pA beam current, a 25 μm field size and a dose of 220 μC/cm^2. The sample was then developed in MIBK:IPA (1:3) for 110 s to remove the exposed PMMA. The LOR was developed in AZ 400K:DI water (1:4) solution for 15 s. The underlying GaAs was then wet etched to release the beams, rinsed

in methanol and blown dry. A standard wet etch recipe H_2SO_4:H_2O_2:H_20 in the ratio 1:8:100 by volume was used. Any remaining resist was removed in an oxygen plasma asher.

A.2 Gold-coated high-stress silicon nitride beams

The fabrication of the silicon nitride nanomechanical resonators was slightly more complicated than the bare gold beams as the whole design was defined using a combination of optical and e-beam lithography which increases the number of fabrication steps. However, some of the steps were common in both, such as the dry etching of Ge and LOR. This section is again divided into two parts, the first explaining the lithography steps and the second one describing the method to release the doubly-clamped beams.

A.2.1 Lithography for contact pads and nano-wires

Contact pads: optical lithography The sample was coated with a 400 nm layer of LOR5B, 35 nm of thermally evaporated Ge followed by 1.2 μm of photo-resist AZ6612 which was spun at 4000 rpm for 30 s and baked on a hot plate for 45 s at 110°C. A custom made optical mask was used to expose the contact pads using optical lithography with an exposure time of 7.8 s at 12 mW/cm^2. The photo-resist was developed in AZ 400K:DI water (1:4) solution for about 30 s. The Ge in the exposed areas was plasma etched using SF_6 as described previously. Only about 50 - 100 nm of LOR was etched away in an oxygen plasma. The sample was then soaked in acetone to remove any remaining photo-resist.

Nano-wires: e-beam lithography The sample was then coated with two layers of 950K PMMA A2 and the wires were patterned using e-beam lithography. Optical alignment marks were used to make sure that the contact pads and the wires overlapped each other to guarantee good electrical contact. An acceleration voltage of 30 kV and a beam current of 225 pA was chosen. The wires were written in a field size of 100 μm using a dose of 400 μC/cm^2. The PMMA was developed in MIBK:IPA (1:3) for 110 s and the remaining Ge/LOR in the exposed areas was plasma etched as previously explained. Before metallization, the sample was dipped in N-methyl-2-pyrrolidone [89] for 1 s in order to remove any remaining LOR in

the exposed areas. In the course of producing a number of devices, it was found that the 5 minute etch in an oxygen plasma did not remove the LOR entirely as traces of the resist could still be observed under an optical microscope after the etch process. N-methyl-2-pyrrolidone is a concentrated solvent and can be used as a photo-resist stripper.

Metallization Next, the sample was loaded into a thermal evaporator and metallized with 3 nm of titanium followed by 90 - 130 nm of gold. The evaporator chamber pressure was kept below 10^{-6} mbar and the deposition rates were between 0.3 - 0.5 nms^{-1}.

Lift-off The sample was then soaked in a photo-resist stripper (1165 Microposit Remover) between 30 - 40 minutes at 60°C to remove the Ge/LOR stencil, rinsed in IPA and blown dry.

A.2.2 Releasing the beams

Instead of using a bilayer resist to define the etch windows, the trilayer PMMA/Ge/LOR was chosen as it provided a better control over the width of the window. The etch windows were written using a voltage of 30 kV, a current of 180 pA in a 100μm field size with a dose of 240 $\mu\text{C/cm}^2$. The PMMA was developed and the Ge/LOR layer etched in the usual manner.

Etching The silicon nitride beams were released via dry etching. This involved an anisotropic etch in RIE mode of Si_3N_4 in a CHF_3 plasma for 240 s (flow rate: 100 sccm, RF power: 150 W). The underlying Si was then isotropically etched, using an inductively coupled plasma (ICP), with SF_6 for 45 s (flow rate: 24 sccm, RF power: 50 W, LF power: 250 W). The RF power was kept low in order to minimize gold sputtering. After releasing the beams, any remaining resist was removed in an oxygen plasma asher.

A.3 Sample bonding

All the samples were attached onto standard 12-pin headers using GE varnish. As the gold nanomechanical resonators are very sensitive to static charges, connections from the contact pads to the header pins was made using indium coated 0.1 mm diameter gold wires. The ends of the wires were

pressed onto the pads/pins using a wooden cocktail stick. Whilst bonding the samples, it was absolutely essential to be connected to ground (earth) to avoid breaking the beams. On the other hand, the silicon nitride devices were connected to the pins using a 17 μm diameter aluminium wire and a commercial wedge bonder.

Appendix B

Theory for modal coupling

In this Appendix, we derive the equations which describe the nonlinear coupling between two different flexural modes of the same doubly-clamped beam. The two modes, labelled m and n are driven at frequencies close to the bare mode frequencies, ω_{0n} and ω_{0m}. All parameters used in the derivation are dimensionless.

The external driving force per unit length is given by

$$F_L = F_{0m}\cos(\omega_m t) + F_{0n}\cos(\omega_n t), \tag{B.1}$$

and the displacement is

$$y = W(\tilde{u}_m\tilde{g}_m + \tilde{u}_n\tilde{g}_n). \tag{B.2}$$

Substituting the expressions above into equation 6.1 leads to

$$\begin{aligned}\rho A[\ddot{\tilde{u}}_m\tilde{g}_m + \ddot{\tilde{u}}_n\tilde{g}_n] + \eta[\dot{\tilde{u}}_m\tilde{g}_m + \dot{\tilde{u}}_n\tilde{g}_n] + [\omega_{0m}^2\rho A\tilde{g}_m]\tilde{u}_m + [\omega_{0n}^2\rho A\tilde{g}_n]\tilde{u}_n \\ -\frac{EAW^2}{2L}\left[\int_0^L(\tilde{g}'_m\tilde{u}_m + \tilde{g}'_n\tilde{u}_n)^2dx\right](\tilde{g}''_m\tilde{u}_m + \tilde{g}''_n\tilde{u}_n) \quad = 0,\end{aligned} \tag{B.3}$$

where

$$\omega_{0n}^2\rho A\tilde{g}_n = EI\tilde{g}_n'''' - T_0\tilde{g}_n''$$

for any given eigenmode. We now focus on one mode by multiplying both sides of B.3 by $\tilde{g}_n$ and integrate over X (recall that orthonormality requires

$\int_0^1 \tilde{g}_m \tilde{g}_n dX = \delta_{mn}$) which translates to the following relation

$$\begin{aligned} &\ddot{\tilde{u}}_n + \omega_{0n}^2 \tilde{u}_n + \gamma \dot{\tilde{u}}_n \\ &+\lambda[\tilde{u}_n^3 I_{nn}^2 + \tilde{u}_m^3 I_{nm} I_{mm} + 3\tilde{u}_n^2 \tilde{u}_m I_{nn} I_{nm} + \tilde{u}_m^2 \tilde{u}_n (I_{nn} I_{mm} + 2I_{nm}^2)] \\ &= [F_{0n} \cos(\omega_n t) + F_{0m} \cos(\omega_m t)] \frac{\xi_n}{\rho A W}, \end{aligned} \tag{B.4}$$

where $I_{mn} = \int_0^1 \tilde{g}'_m \tilde{g}'_n dX$. Adopting dimensionless units for time, $t^* = \omega_{0n} t$, and dividing through by ω_{0n}^2, equation B.4 transforms into

$$\begin{aligned} &\ddot{\tilde{u}}_n + \tilde{u}_n + \frac{\dot{\tilde{u}}_n}{Q_n} \\ &+\frac{\lambda}{\omega_{0n}^2}[\tilde{u}_n^3 I_{nn}^2 + \tilde{u}_m^3 I_{nm} I_{mm} + 3\tilde{u}_n^2 \tilde{u}_m I_{nn} I_{nm} + \tilde{u}_m^2 \tilde{u}_n (I_{nn} I_{mm} + 2I_{nm}^2)] \\ &= f_n \cos(\tilde{\omega}_n t^*) + f_m \cos(\tilde{\omega}_m t^*). \end{aligned} \tag{B.5}$$

The general solution

$$\tilde{u}_{n(m)} = a_{n(m)} \cos(\tilde{\omega}_{n(m)} t^*) + b_{n(m)} \sin(\tilde{\omega}_{n(m)} t^*) \tag{B.6}$$

is substituted into equation B.5 and terms oscillating at ω_n are collected, neglecting the higher harmonics and assuming that $\omega_m \neq 3\omega_n$. This leads to the characteristic equation

$$\begin{aligned} &(1 - \tilde{\omega}_n^2)(a_n \cos(\tilde{\omega}_n t^*) + b_n \sin(\tilde{\omega}_n t^*)) \\ &+\frac{\tilde{\omega}_n}{Q_n}(-a_n \sin(\tilde{\omega}_n t^*) + b_n \cos(\tilde{\omega}_n t^*)) \\ &+\frac{\lambda}{\omega_{0n}^2}[\frac{3}{4} r_n^2 I_{nn}^2 (a_n \cos(\tilde{\omega}_n t^*) + b_n \sin(\tilde{\omega}_n t^*)) \\ &+\frac{r_m^2}{2}(I_{nn} I_{mm} + 2I_{nm}^2)(a_n \cos(\tilde{\omega}_n t^*) + b_n \sin(\tilde{\omega}_n t^*))] \quad = f_n \cos(\tilde{\omega}_n t^*), \end{aligned} \tag{B.7}$$

which is used to define

$$H = (1 - \tilde{\omega}_n^2) + \frac{\lambda}{\omega_{0n}^2} \frac{3}{4} r_n^2 I_{nn}^2 + \frac{\lambda}{\omega_{0n}^2} \frac{r_m^2}{2} (I_{nn} I_{mm} + 2I_{nm}^2). \tag{B.8}$$

The coefficients a_n and b_n are extracted by carrying out a Fourier analysis

which gives the response amplitude as:

$$r_n^2 = \frac{f_n^2}{H^2 + \frac{\tilde{\omega}_n^2}{Q_n^2}} \tag{B.9}$$

and the angular frequency renormalization:

$$\omega_{2n}^2 = \omega_{0n}^2 \left[1 + \frac{3}{4} \frac{I_{nn}^2}{\omega_{0n}^2} \lambda r_n^2 + r_m^2 \frac{\lambda}{\omega_{0n}^2} \left(\frac{I_{nn} I_{mm}}{2} + I_{nm}^2 \right) \right], \tag{B.10}$$

which translates into

$$f_{2n} = f_{1n} + r_m^2 \frac{\lambda}{8\pi^2 f_{1n}} \left(\frac{I_{nn} I_{mm}}{2} + I_{nm}^2 \right). \tag{B.11}$$

The amplitudes r_m and r_n are dimensionless, but can be related to a physical displacement ($A_{m(n)}$) via a mode function:

$$A_{m(n)}(x) = W r_{m(n)} g_{m(n)}(x) \tag{B.12}$$

which is most sensibly defined at the antinode at $x = \frac{L}{2}$ for $n(m) = 1, 3, 5, ...$ (odd modes are symmetric about the centre of the beam).

Bibliography

[1] A. N. Cleland. *Foundations of Nanomechanics*. Springer, 2003.

[2] K. L. Ekinci and M. L. Roukes. Nanoelectromechanical systems. *Rev. Sci. Instrum.*, 76:061101, 2005.

[3] M. L. Roukes. Nanoelectromechanical systems face the future. *Physics World*, 14(2):25, 2001.

[4] M. P. Blencowe. Quantum electromechanical systems. *Phys. Rep.*, 395:159, 2004.

[5] D. Rugar, R. Budakian, H. J. Mamin, and B. W. Chui. Single spin detection by magnetic resonance force microscopy. *Nature*, 430:329, 2004.

[6] Y. T. Yang, C. Callegari, X. L. Feng, K. L. Ekinci, and M. L. Roukes. Zeptogram-scale nanomechanical mass sensing. *Nano Letters*, 6(4):583, 2006.

[7] C. A. Regal, J. D. Teufel, and K. W. Lehnert. Measuring nanomechanical motion with a microwave cavity interferometer. *Nature Physics*, 4:555, 2008.

[8] M. D. LaHaye, J. Suh, P. M. Echternach, K. C. Schwab, and M. L. Roukes. Nanomechanical measurements of a superconducting qubit. *Nature*, 459:960, 2009.

[9] T. Rocheleau, T. Ndukum, C. Macklin, J. B. Hertzberg, A. A. Clerk, and K. C. Schwab. Preparation and detection of a mechanical resonator near the ground state of motion. *Nature*, 463:72, July 2010.

[10] R. H. Blick, A. Erbe, L. Pescini, A. Kraus, D. V. Scheible, F. W. Beil, E. Hoehberger, A. Hoerner, J. Kirschbaum, H. Lorenz, and J. P. Kotthaus. Nanostructured silicon for studying fundamental aspects of nanomechanics. *J. Phys. Condens. Matter*, 14:905, 2002.

[11] R. Lifshitz and M. C. Cross. Nonlinear dynamics of nanomechanical and micromechanical resonators. Preprint of contribution to: Review of Nonlinear

Dynamics and Complexity, Edited by H. G. Schuster (Wiley, 2008), March 2008.

[12] H. W. Ch. Postma, I. Kozinsky, A. Husain, and M. L. Roukes. Dynamic range of nanotube- and nanowire-based electromechanical systems. *Appl. Phys. Lett.*, 86:223105, 2005.

[13] R. B. Karabalin, M. C. Cross, and M. L. Roukes. Nonlinear dynamics and chaos in two coupled nanomechanical resonators. *Phys. Rev. B*, 79(16):165309, 2009.

[14] H. J. R. Westra, M. Poot, H. S. J. van der Zant, and W. J. Venstra. Nonlinear modal interactions in clamped-clamped mechanical resonators. *Phys. Rev. Lett.*, 105(11):117205, 2010.

[15] T. Dunn, J-S. Wenzler, and P. Mohanty. Anharmonic modal coupling in a bulk micromechanical resonator. *App*, 97(12):123109, 2010.

[16] D. H. Santamore, A. C. Doherty, and M. C. Cross. Quantum nondemolition measurement of fock states of mesoscopic mechanical oscillators. *Phys. Rev. B*, 70(14):144301, 2004.

[17] A. Venkatesan, K. J. Lulla, M. J. Patton, A. D. Armour, C. J. Mellor, and J. R. Owers-Bradley. Dissipation in a gold nanomechanical resonator at low temperatures. *J. Low Temp. Phys.*, 158:685, 2009.

[18] A. Venkatesan, K. J. Lulla, M. J. Patton, A. D. Armour, C. J. Mellor, and J. R. Owers-Bradley. Dissipation due to tunneling two-level systems in gold nanomechanical resonators. *Phys. Rev. B*, 81(7):073410, 2010.

[19] B. Witkamp. *High-frequency nanotube resonators*. PhD thesis, Technische Universiteit Delft, 2009.

[20] T. v.Karman and M. A. Biot. *Mathematical methods in engineering*. McGraw-Hill Book Company, 1940.

[21] P. Hagedorn and A. DasGupta. *Vibrations and waves in continuous mechanical systems*. Wiley, 2007.

[22] A. Bokaian. Natural frequencies of beams under tensile axial loads. *J. Sound and Vibration*, 142(3):481, 1990.

[23] I. Kozinsky. *Nonlinear Nanoelectromechanical Systems*. PhD thesis, California Institute of Technology, 2007.

[24] R. B. Bhiladvala and Z. J. Wang. Effect of fluids on the Q factor and resonance frequency of oscillating micrometer and nanometer scale beams. *Phys. Rev. E*, 69:036307, 2004.

[25] V. A. Sazonova. *A tunable carbon nanotube resonator.* PhD thesis, Cornell University, 2006.

[26] I. Wilson-Rae. Intrinsic dissipation in nanomechanical resonators due to phonon tunneling. *Phys. Rev. B*, 77(24):245418, 2008.

[27] A. N. Cleland and M. L. Roukes. External control of dissipation in a nanometer-scale radiofrequency mechanical resonator. *Sensors and Actuators*, 72:256, 1999.

[28] C. Zener. Internal friction in solids. *Physical Review*, 53:90, 1938.

[29] R. Lifshitz and M. L. Roukes. Thermoelastic damping in micro- and nanomechanical systems. *Phys. Rev. B*, 61(8):5600, 2000.

[30] K. Y. Yasumura, T. D. Stowe, E. M. Chow, T. Pfafman, T. W. Kenny, B. C. Stipe, and D. Rugar. Quality factors in micron- and submicron-thick cantilevers. *Journal of microelectromechanical systems*, 9(1):117, 2000.

[31] J. A. Henry, Y. Wang, and M. A. Hinesa. Controlling energy dissipation and stability of micromechanical silicon resonators with self-assembled monolayers. *Appl. Phys. Lett.*, 84(10):1765, 2004.

[32] R. C. Zeller and R. O. Pohl. Thermal conductivity and specific heat of noncrystalline solids. *Phys. Rev. B*, 4(6):2029, 1971.

[33] S. Hunklinger and A. K. Raychaudhuri. *Progress in low temperature physics*, volume IX. North-Holland, 1986.

[34] W. A. Phillips. Tunneling states in amorphous solids. *J. Low Temp. Phys.*, 7, 1972.

[35] P. W. Anderson, B. I. Halperin, and C. M. Varma. Anomalous low-temperature thermal properties of glasses and spin glasses. *Philos. Mag.*, 25 (1), 1972.

[36] W. A. Phillips. Two-level states in glasses. *Rep. Prog. Phys.*, 50:1657, 1987.

[37] P. Esquinazi and R. König. *Tunneling Systems in Amorphous and Crystalline Solids.* Springer-Verlag, 1998.

[38] A. D. Fefferman, R. O. Pohl, A. T. Zehnder, and J. M. Parpia. Acoustic properties of amorphous silica between 1 and 500 mk. *Phys. Rev. Lett.*, 100 (19):195501, 2008.

[39] R. O. Pohl, X. Liu, and E. Thompson. Low-temperature thermal conductivity and acoustic attenuation in amorphous solids. *Rev. Mod. Phys.*, 74(4):991, 2002.

[40] J. Classen, T. Burkert, C. Enss, and S. Hunklinger. Anomalous frequency dependence of the internal friction of vitreous silica. *Phys. Rev. Lett.*, 84(10): 2176, 2000.

[41] P. Esquinazi, R. König, and F. Pobell. Acoustic properties of amorphous SiO2 and PdSiCu, and of crystalline Ag, NbTi and Ta at very low temperatures. *Z. Phys. B Cond. Matt.*, 87, 1992.

[42] R. König, P. Esquinazi, and B. Neppert. Tunneling systems in polycrystalline metals: Absence of electron-assisted relaxation. *Phys. Rev. B*, 51(17):424, 1995.

[43] J. Haust, M. Burst, R. Haueisen, and G. Weiss. Low temperature acoustic properties of poly-crystalline aluminium. *J. Low Temp. Phys.*, 137(3/4):523, 2004.

[44] X. Liu, E. Thompson, B. E. White Jr, and R. O. Pohl. Low-temperature internal friction in metal films and in plastically deformed bulk aluminum. *Phys. Rev. B*, 59(18):767, 1999.

[45] G. Zolfagharkhani, A. Gaidarzhy, S. Shim, R. L. Badzey, and P. Mohanty. Quantum friction in nanomechanical oscillators at millikelvin temperatures. *Phys. Rev. B*, 72:224101, 2005.

[46] P. Mohanty, S. B. Shim, J. S. Chun, S. W. Kang, S. W. Cho, S. W. Cho, Y. D. Park, N. Kim, and J. Kim. Micromechanical resonators fabricated from lattice-matched and etch-selective GaAs/InGaP/GaAs heterostructures. *Appl. Phys. Lett.*, 91(13):133505, 2007.

[47] M. Imboden and P. Mohanty. Evidence of universality in the dynamical response of micromechanical diamond resonators at millikelvin temperatures. *Phys. Rev. B*, 79(12):125424, 2009.

[48] Resist supplied by *MicroChem Corp.,* Newton, MA, USA.

[49] L. D. Jackel, R. E. Howard, E. L. Hu, D. M. Tennant, and P. Grabbe. 50-nm silicon structures fabricated with trilevel electron beam resist and reactive-ion etching. *Appl. Phys. Lett.*, 39(3):268, 1981.

[50] Solvent supplied by *Rohm and Haas Electronic Materials,* Marlborough, MA, USA.

[51] The silicon wafers were supplied by *Wafer World Inc.,* West Palm Beach, Florida, USA.

[52] The silicon nitride layers were deposited on the silicon substrates using a low pressure chemical vapour deposition (LPCVD) process at the Cornell Nanoscale Science and Technology Facility (CNF), 250 Duffield Hall, Cornell University, Ithaca, New York, USA.

[53] K. L. Ekinci, Y. T. Yang, X. M. H. Huang, and M. L. Roukes. Balanced electronic detection of displacement in nanoelectromechanical systems. *Appl. Phys. Lett.*, 81(12):2253, 2002.

[54] A. N. Cleland and M. L. Roukes. Fabrication of high frequency nanometer scale mechanical resonators from bulk Si crystals. *Appl. Phys. Lett.*, 69(18): 2653, 1996.

[55] R. G. Knobel and A. N. Cleland. Nanometre-scale displacement sensing using a single electron transistor. *Nature*, 424:291, 2003.

[56] N. E. Flowers-Jacobs, D. R. Schmidt, and K. W. Lehnert. Intrinsic noise properties of atomic point contact displacement detectors. *Phys. Rev. Lett.*, 98(9):096804, 2007.

[57] S. S. Verbridge, J. M. Parpia, R. B. Reichenbach, L. M. Bellan, and H. G. Craighead. High quality factor resonance at room temperature with nanostrings under high tensile stress. *J. Appl. Phys.*, 99(12):124304, 2006.

[58] X. M. H. Huang, C. A. Zorman, M. Mehregany, and M. L. Roukes. Nanodevice motion at microwave frequencies. *Nature*, 421:496, 2003.

[59] A. B. Hutchinson, P. A. Truitt, K. C. Schwab, L. Sekaric, J. M. Parpia, H. G. Craighead, and J. E. Butler. Dissipation in nanocrystalline-diamond nanomechanical resonators. *Appl. Phys. Lett.*, 84(6):972, 2004.

[60] MITEQ AU-1114-BNC room temperature rf pre-amplifier.

[61] X. M. H. Huang, X. L. Feng C. A. Zorman, M. Mehregany, and M. L. Roukes. VHF, UHF and microwave frequency nanomechanical resonators. *New Journal of Physics*, 7(247), 2005.

[62] Advanced Control Components (ACC) W500E rf amplifier.

[63] T. F. Li, Yu. A. Pashkin, O. Astafiev, Y. Nakamura, and J. S. Tsai. High-frequency metallic nanomechanical resonators. *Appl. Phys. Lett.*, 92(4): 043112, 2008.

[64] P. J. Koppinen and I. J. Maasilta. Phonon cooling of nanomechanical beams with tunnel junctions. *Phys. Rev. Lett.*, 102(16):165502, 2009.

[65] M. A. Sillanpää, J. Sarkar, J. Sulkko, J. Muhonen, and P. J. Hakonen. Accessing nanomechanical resonators via a fast microwave circuit. *Appl. Phys. Lett.*, 95(1):011909, 2009.

[66] D. S. Greywall, B. Yurke, P. A. Busch, and S. C. Arney. Low-temperature anomalies in the dissipation of small mechanical resonators. *Europhys. Lett.*, 34(1):37, 1996.

[67] F. C. Nix and D. MacNair. The thermal expansion of pure metals: Copper, gold, aluminium, nickel, and iron. *Physical Review*, 60:597, 1941.

[68] J. S. Blakemore. Semiconducting and other major properties of gallium arsenide. *J. Appl. Phys.*, 53(10):123, 1982.

[69] K. Chun and N. O. Birge. Dissipative quantum tunneling of a single defect in a disordered solid. *Phys. Rev. B*, 54(7):4629, 1996.

[70] C. Seoánez, F. Guinea, and A. H. Castro Neto. Surface dissipation in nanoelectromechanical systems: Unified description with the standard tunneling model and effects of metallic electrodes. *Phys. Rev. B*, 77(12):125107, 2008.

[71] D. R. Southworth, R. A. Barton, S. S. Verbridge, B. Ilic, A. D. Fefferman, H. G. Craighead, and J. M. Parpia. Stress and silicon nitride: A crack in the universal dissipation of glasses. *Phys. Rev. Lett.*, 102(22):225503, 2009.

[72] F. Hoehne, Yu. A. Pashkin, O. Astafiev, L. Faoro, L. B. Ioffe, Y. Nakamura, and J. S. Tsai. Damping in high-frequency metallic nanomechanical resonators. *Phys. Rev. B*, 81(18):184112, 2010.

[73] J. Sulkko, M. A. Sillanpää, P. Häkkinen, L. Lechner, M. Helle, A. Fefferman, J. Parpia, and P. J. Hakonen. Strong gate coupling of high-Q nanomechanical resonators. *Nano Letters*, 10:4884, 2010.

[74] A. D. Fefferman, R. O. Pohl, and J. M. Parpia. Elastic properties of polycrystalline Al and Ag films down to 6 mk. *Phys. Rev. B*, 82(6):064302, 2010.

[75] L. G. Remus, M. P. Blencowe, and Y. Tanaka. Damping and decoherence of a nanomechanical resonator due to a few two-level systems. *Phys. Rev. B*, 80 (17):174103, 2009.

[76] A. Trionfi, S. Lee, and D. Natelson. Time-dependent universal conductance fluctuations in mesoscopic au wires: Implications. *Phys. Rev. B*, 75(10): 104202, 2007.

[77] Q. P. Unterreithmeier, E. M. Weig, and J. P. Kotthaus. Universal transduction scheme for nanomechanical systems based on dielectric forces. *Nature*, 458: 1001, 2009.

[78] R. A. Barton, B. Ilic, S. S. Verbridge, B. R. Cipriany, J. M. Parpia, and H. G. Craighead. Fabrication of a nanomechanical mass sensor containing a nanofluidic channel. *Nano Letters*, 10:2058, 2010.

[79] S. S. Verbridge, H. G. Craighead, and J. M. Parpia. A megahertz nanomechanical resonator with room temperature quality factor over a million. *Appl. Phys. Lett.*, 92(1):013112, 2008.

[80] W-H. Chuang. Mechanical property characterization of LPCVD silicon nitride thin films at cryogenic temperatures. *Journal of microelectromechanical systems*, 13(5):870, 2004.

[81] Q. P. Unterreithmeier, T. Faust, and J. P. Kotthaus. Damping of nanomechanical resonators. *Phys. Rev. Lett.*, 105(2):027205, 2010.

[82] J. B. Hertzberg. *Back-action evading measurements of nanomechanical motion approaching quantum limits*. PhD thesis, University of Maryland, 2009.

[83] A. H. Nayfeh and D. T. Mook. *Nonlinear Oscillations*. Wiley Interscience, 1979.

[84] H. Cho, M. Yu, A. F. Vakakis, L. A. Bergman, and D. M. McFarland. Tunable, broadband nonlinear nanomechanical resonator. *Nano Letters*, 10:1793, 2010.

[85] Q. P. Unterreithmeier, T. Faust, and J. P. Kotthaus. Nonlinear switching dynamics in a nanomechanical resonator. *Phys. Rev. B*, 81(24):241405, 2010.

[86] L. N. Hand and J. D. Finch. *Analytical Mechanics*. Cambridge University Press, 1998.

[87] M. Poot. *Mechanical systems at the nanoscale*. PhD thesis, Technische Universiteit Delft, 2009.

[88] F. Pobell. *Matter and Methods at Low Temperatures*. Springer-Verlag, 1996.

[89] Supplied by *Dupont Electronics,* Rue General Patton, L-2984, Luxembourg.